Experimental Study of Quantum Dot and Dash Lasers

Susannah C. Heck

Thesis Submitted for the Degree of Doctor of Philosophy

Department of Physics
University College Cork
National University of Ireland
Cork

Supervisors: Prof. Eoin P. O'Reilly and Dr. Simon Osborne
Head of Department: Prof. John G. McInerney

July 2009

Contents

I declare that this thesis contains my own work and has not been submitted for another degree, either at University College Cork or elsewhere.
Susannah C. Heck

Abstract

Quantum dashes are elongated quantum dots. Polarized edge-photovoltage and spontaneous emission spectroscopy are used to study the anisotropy of optical properties in 1.5μm InGaAsP and AlGaInAs-based quantum dash lasers. Strain, which causes TM-polarized transitions to be suppressed at the band edge, coupled with carrier confinement and dash shape leads to an enhancement of the optical properties for light polarized along the dash long axis, in excellent agreement with theoretical results. An analysis of the integrated facet and spontaneous emission rate with total current and temperature reveals that, in both undoped and p-doped InGaAsP-based quantum dash lasers at room temperature, the threshold current and its temperature dependence remain dominated by Auger recombination. We also identify two processes which can limit the output power and propose that the effects of the dopant in p-doped InGaAsP-based lasers dominate at low temperature but decrease with increasing temperature. A high threshold current density in undoped AlGaInAs-based quantum dash laser samples studied, which degrade rapidly at low temperature, is not due to intrinsic carrier recombination processes. 1.3μm GaAs-based quantum dots lasers have been widely studied, but there remains issues as to the nature of the electronic structure. Polarized edge-photovoltage spectroscopy is used to investigate the energy distribution and nature of the energy states in InAs/GaAs quantum dot material. A non-negligible TM-polarized transition, which is often neglected in calculations and analyses, is measured close to the main TE-polarized ground state transition. Theory is in very good agreement with the experimental results and indicates that the measured low-energy TM-polarized transition is due to the strong spatial overlap between the ground state electron and the light-hole component of a low-lying excited hole state. Further calculations suggest that the TM-polarized transition reduces at the band edge as the quantum dot aspect ratio decreases.

Acknowledgements

I would like to begin by thanking Prof. Eoin O'Reilly for the opportunity to carry out a Ph.D. in an interesting and challenging area as well as the opportunity of being involved in a European research project. At this point I would like to acknowledge financial support of the ZODIAC (Zero Order Dimension based Industrial components Applied to teleCommunications) IST European project as well as Science Foundation Ireland. Thank you also to my second supervisor, Dr. Simon Osborne, for his time, feedback and friendship. I would also like to thank my collegues, Dr. Sorcha Healy and Mark Crowley, with whom it was pleasure to collaborate.

Thank you to Dr. François Lelarge at Alcatel-Thales III-V Lab, joint lab: Bell Labs and Thales Research and Technology, Dr. Marc Fischer at nanoplus GmbH, Sebastian Hein at the University of Würzburg as well as Dr. Bob Manning and Dr. Rod Webb for providing most of the samples used in this research.

I would also like to thank a number of collegues and former collegues from the Tyndall National Institute: Robert Allison, Nicola Brandonisio, Vladimir Djara, Peter Engelstaedter, Dr. Robin Fehse, Dr. Fatima Gunning, John Justice, Pio Jesudoss, Krimo Khalfi, Carmel Kelleher, Vince Lodge, Dr. Bob Manning, Dr. James O'Callaghan, Dan O'Connell, Shane O'Donoghue, John Ray, Monika Rutowska, Paudie Scanlon, Pawel Sajewicz, Dr. Giuseppe Talli and Dr. Robert Young.

To Dr. Stephen Sweeney and Prof. John McInerney, thank you for your time in reading my thesis and for the stimulating discussions during my viva voce.

Last but not least, I like to thank my friends and family, especially my parents, Emer and Bernard Heck, my siblings, Monica, Patrick, Kevin, Brendan and Kathleen, and my boyfriend, Bryan Feeney, for their encouragement, love and support.

Publications

Polarization Resolved Ground State Absorption of 1.3 μm InAs/GaAs Quantum Dots,
M. T. Crowley, S. C. Heck, S. Osborne, S. B. Healy, and E. P. O'Reilly, submitted to *Applied Physics Letters* (2009).

Experimental and Theoretical Study of InAs/InP Quantum Dash Lasers,
S. C. Heck, S. Osborne, S. B. Healy, E. P. O'Reilly, F. Lelarge, F. Poingt, A. Accard, F. Pommereau, and O. Le Gouezigou, to be published in *IEEE Journal Of Quantum Electronics* (2009).

An Analysis of 1.55 μm InAs/InP Quantum Dash Lasers,
S. C. Heck, S. B. Healy, S. Osborne, E. P. O'Reilly, F. Lelarge, F. Poingt, A. Accard, F. Pommereau, O. Le Gouezigou, and B. Dagens, *Applied Physics Letters* 92, 251105 (2008).

Theoretical and Experimental Analysis of InAs/InGaAsP/InP Quantum Dash Lasers,
S. C. Heck, S. B. Healy, S. Osborne, D. P. Williams, R. Fehse, E. P. O'Reilly, F. Lelarge, F. Poingt, A. Accard, F. Pommereau, O. Le Gouezigou, and B. Dagens, 20th International Conference on Indium Phosphide and Related Materials, *IPRM 2008*, 1–4 (2008).
DOI:10.1109/ICIPRM.2008.4702976

Consider the postage stamp: its usefulness consists in the ability to stick to one thing till it gets there.

Josh Billings

Chapter 1

Introduction

Semiconductor lasers play a central role in fibre-based optical telecommunication systems, as well as being widely used in many other applications, including printing, medicine and data storage. This thesis contains an analysis of semiconductor quantum dot materials and lasers operating in the infrared at 1.3 μm and 1.5 μm. The former, where silica-based optical fibres exhibit zero dispersion, is used in short-haul optical links. The window at the longer wavelength, where optical losses are minimal in silica-based optical fibres, is used in long-haul optical networks.

The choice of semiconductor materials depends on the wavelength required. Since the 1970s InP-based semiconductor lasers have been used to achieve lasing at 1.3 μm and 1.5 μm. Bulk InGaAsP/InP lasers emitting at 1.5 μm have been commercially used since the middle of the 1980s and most recent InP-based lasers have InGaAsP/InP quantum well active regions [1]. However there is usually a need for expensive temperature controlling components in these laser modules due to the strong temperature sensitivity of the laser characteristics. 1.3 μm lasers are slightly less temperature sensitive than 1.5 μm lasers, due to the wider bandgap. GaAs-based vertical-cavity surface-emitting lasers, which emit at 1.3 μm, have been attracting much research interest, because suitable Bragg mirrors can be grown using an alternating sequence of GaAs and AlAs layers. Although there is an interest in growing GaAs-based lasers which emit at 1.5 μm [2, 3], there remains difficulty in extending these devices to wavelengths longer than 1.3 μm. Therefore InP remains the most suitable substrate choice for this spectral region.

It has been predicted that semiconductor laser characteristics change when the dimensions of the material are reduced to the order of the de Broglie wavelength [4]. This has been confirmed in moving from bulk to quantum well lasers on both GaAs and InP, with for example a reduction in the threshold current density and its temperature dependence. Quantum dots are obtained when all three dimen-

sions of the semiconductor material have been reduced, leading to a quantisation of the electron momentum in all three dimensions [5].
There is an interest in growing quantum dots on InP. Although it has been more challenging than growing on GaAs, advances have recently been made in growing quantum dots on the commercially favoured (001)-InP substrate orientation. The dots are elongated along (1-10) and are known as *quantum dashes* [6, 7].
GaAs-based quantum dot lasers have been widely studied with promising results, but there remain issues as to the nature of the electronic structure, and hence the polarization of transitions, in InAs/GaAs quantum dot materials.

1.1 Thesis Structure

This thesis begins with a summary of the basic theoretical concepts relevant to this work in chapter 2, while an overview of the experimental methods are presented in chapter 3. Chapter 4 contains an analysis of undoped 1.5 μm InAs/InGaAsP/InP quantum dash materials and lasers. A polarization anisotropy of the optical properties is measured in these lasers, in excellent agreement with theoretical predictions. We also investigate the dominant carrier recombination process in these undoped InP-based devices as a function of current and temperature. Having established the characteristics of this material system we consider the influence of p-doping on InAs/InGaAsP/InP quantum dash lasers in chapter 5. We consider the effect of the high density of acceptors and its temperature dependence in order to analyse of the recombination mechanisms at room temperature. We then study undoped InAs/AlGaInAs/InP quantum dash lasers in Chapter 6 in order to compare them to the devices studied in chapter 4. We investigate the polarization dependence of the optical properties and the carrier recombination process present in these lasers. In chapter 7 we consider the polarization characteristics of 1.3 μm InAs/GaAs quantum dots in order to identify the energy distribution and nature of the energy states close to the band edge to confirm whether or not the ground state in these dots is purely TE-polarized. Finally a summary of the work presented in this thesis can be found in chapter 8.

Chapter 2

Background Theory

2.1 Introduction

The aim of this chapter is to provide an overview of the background theory of semiconductor lasers relevant to this thesis. The chapter begins by providing a brief history of the laser diode. The following sections then provide an overview of the concepts which will be used in this work. The requirements to achieve lasing and an overview of three basic types of edge-emitting laser structures are included in section 2.3. In section 2.4 we consider laser light-current characteristics. The change in density of states between bulk, quantum well, quantum wire and quantum dot material is described in section 2.5. Lastly we consider recombination processes in diode lasers. We consider first the spontaneous emission rate and its polarization dependence. Next we review the main non-radiative recombination processes and optical losses, which can occur in real diode lasers. This chapter is summarised in section 2.8.

2.2 Brief History of the Diode Laser

A number of books and papers give a good overview of the history of semiconductor diode lasers [1, 8–10]. The first electrically pumped semiconductor lasers were based on recombination at a pn homojunction, and operated pulsed at 77 K [11–14]. These homojunction lasers, shown schematically in the top panel of Fig. 2.1 had large threshold current densities (10 – 100 kA cm^{-2}) due in large part to the absence of both optical and carrier confinement. Carrier and optical confinement are improved in the growth direction by growing a double heterostructure (DHS), shown schematically in the middle panel of Fig. 2.1. In this design, proposed by Kroemer in 1963 [15], the active region is sandwiched between two doped cladding layers with larger energy gap and smaller refractive index. The DHS acts as a

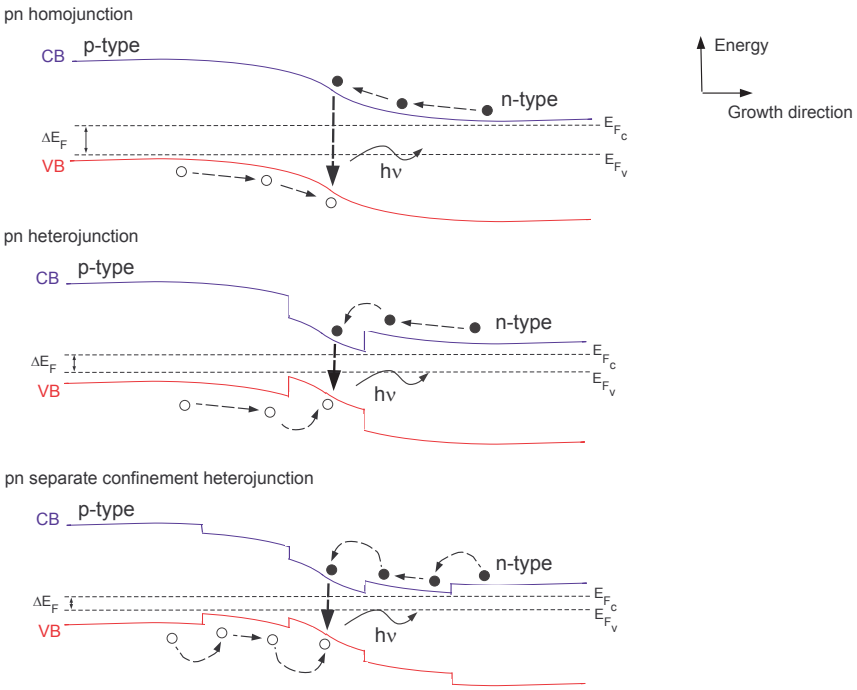

Figure 2.1: Schema of the conduction and valence band energy profiles of a forward biased pn homojunction laser (top), for a double heterostructure pn junction (middle) and for a double heterostructure pn junction with separate confinement heterostructure layers (bottom), where E_{F_c} and E_{F_v} are the conduction and valence band quasi-Fermi levels, with a energy separation ΔE_F.

waveguide for photons and to prevent electron and hole leakage from the active region. The first material system used to make DHS lasers was bulk AlGaAs grown on bulk GaAs, because this pair of alloys are similar lattice constants, often referred to as being lattice-matched. Both pulsed and continuous-wave lasing were demonstrated at room temperature in 1970 [16–18].

Improvements in diode laser characteristics were seen in the 1970s as the growth of the semiconductor material moved from liquid phase epitaxy (LPE) to molecular beam epitaxy (MBE) and metal organic vapour phase epitaxy (MOVPE), which allowed precise monitoring of the thickness, planarity and composition of each layer. Laser characteristics also improved by using separate confinement heterostructure (SCH) layers, illustrated in the bottom panel of Fig. 2.1. As the name suggests, these structures provide separate confinement of charge carriers in the central narrow-gap region, and of the photon mode by the lower refractive index cladding layers.

Once room temperature operation in semiconductor laser diodes was demon-

strated, diode lasers found applications in many areas, including printing, medicine, data storage and as sources for optical fibre-based telecommunication. The rapid growth in the Internet would not have been possible without the roll out of fibre-based optical telecommunication systems where InP-based lasers have played a central role. Optical fibre communication was proposed in the mid-1960s and by the mid-1970s two windows in the infrared had been identified for telecom applications [1]. The first, at 1.3 μm, shows no material dispersion in silica fibres and is now used for short haul applications. The second window, at 1.5 μm, has minimal optical loss and is used in long haul optical systems. In the mid to late 1970s, bulk InP-based diode lasers were demonstrated at both 1.3 μm and 1.5 μm [19, 20]. Bulk InGaAsP/InP lasers have been commercially used since the middle of the 1980s, while most recent InP-based lasers have InGaAsP strained quantum well active regions [1]. However AlGaInAs/InP has been a competing material system since it was demonstrated in the mid 1990s with promising results [21]. The difference between these two material systems will be described in detail in chapter 6. Although quantum wells were proposed and first demonstrated in the mid-1970s [22], growing the thin layers required to make a quantum well was initially challenging even by MBE and MOVPE. In 1982 the first quantum well laser to outperform bulk lasers was reported [23]. That same year Arakawa and Sakaki [4] predicted that quantum wire and quantum dot lasers should have reduced threshold current with improved temperature stability compared to quantum well lasers. As with quantum wells, it remained challenging throughout the 1980s and 1990s to grow quantum wires and dots. The first quantum dot laser based on GaAs was demonstrated in 1994 [24] and six years later the first 1.3 μm GaAs-based quantum dot laser with a very low threshold current was reported [25].

Quantum dots grown on GaAs, which operate at 1.3 μm, are now commercially available. However there have been issues extending GaAs-based quantum well and quantum dot materials to the second telecom window at 1.5 μm, due to the large lattice mismatch between GaAs and InAs. There are currently two approaches being investigated to extend GaAs-based lasers to longer wavelengths. The first involves adding a small amount of N and/or Sb to GaInAs to further reduce the bandgap [26]. Quantum well lasers have been demonstrated based on this material system [27, 28], but there remain issues related to defects in the active region, and concerns about device reliability. The second approach involves reducing the lattice mismatch between GaAs and InAs by growing a metamorphic buffer layer [29, 30]. Lasing at 1.5 μm has been measured in quantum well and quantum dot lasers with a metamorphic layer [2, 3], but the temperature performance is quite poor. There are also issues of defects in the active region

and device reliability in lasers which contain a metamorphic layer. The growth of quantum dots on an InP-substrate is more challenging than on GaAs due to the larger lattice mismatch. Two approaches currently being investigated. The first approach involves using highly misoriented substrates, such as (311)B [6, 31], where device processing is challenging. Recently advances have also been made in growing quantum dots on the commercially favoured (001)-InP substrate orientation. Using this substrate orientation enables the use of the same fabrication processes as for bulk and quantum well lasers [6, 7].

2.3 Basic Principles of Diode Lasers

The objective of a laser is emit coherent radiation, where the energy and phase of all the photons is the same. The requirements for lasing are positive gain and optical feedback and the laser reaches threshold when the modal gain equals the total losses. In this section we focus on the requirements to achieve lasing. We begin by reviewing radiative recombination, considering both emission and absorption. We then present the condition for positive gain and the threshold condition in a Fabry-Pérot laser.

2.3.1 Electronic Transitions

In this section we consider single mode band-to-band transitions, which can be seen schematically in Fig. 2.2, between a single conduction and valence band. Transitions must conserve energy and momentum,

$$E_{21} = E_2 - E_1 = h\nu \tag{2.1}$$

$$k_2 = k_1 \tag{2.2}$$

and must occur between a filled initial state and an empty final state. The left panel of Fig. 2.2 shows stimulated absorption, R_{12}, which is responsible for the generation of carriers and the loss of photons. This is the recombination process used in photovoltage measurements for example. The middle panel of Fig. 2.2 shows stimulated emission, R_{21}, where an incoming photon causes an electron and hole to recombine, producing a photon with the same energy and phase as the incoming photon. R_{12} and R_{21} are competing processes and results in a net stimulated emission rate, $R_{st} = R_{21}$ - R_{12}. The right panel of Fig. 2.2 shows the single mode spontaneous emission for a photon, R^*_{sp}. This downward transition, induced by a vacuum field photon, is similar to R_{21}, but has a random phase and generally a different emission direction compared to the stimulated photons.

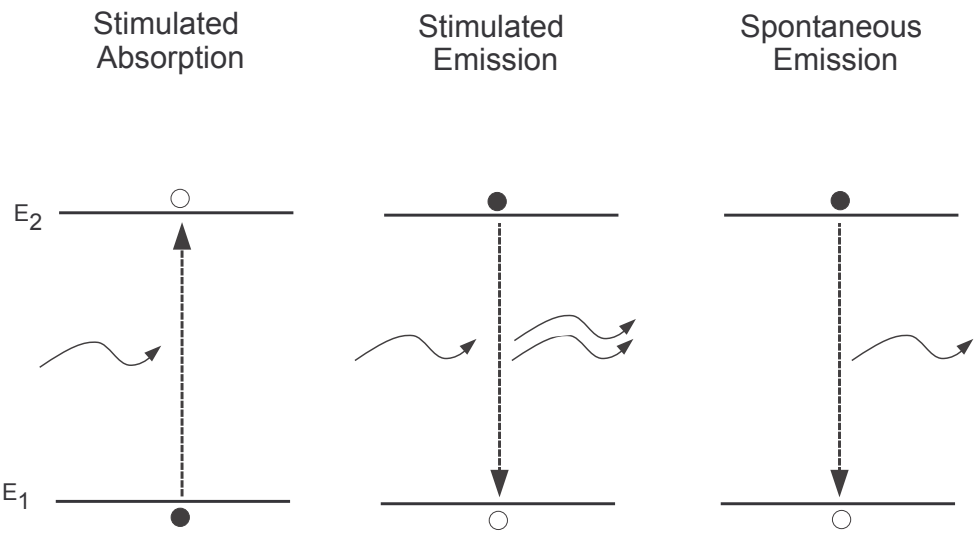

Figure 2.2: Schema of three single mode band-to-band transition types, where the left panel is stimulated absorption, middle panel is stimulated emission and right panel is spontaneous emission.

Taking the occupation probabilities of states 1 and 2, f_1 and f_2, we can write the transition rates for R_{12}, R_{21}, R^*_{sp} and R_{st} as

$$R_{12} = R_r f_1(1 - f_2)P \tag{2.3}$$

$$R_{21} = R_r f_2(1 - f_1)P \tag{2.4}$$

$$R^*_{sp} = R^*_r f_2(1 - f_1) \tag{2.5}$$

$$R_{st} = R_r(f_2 - f_1)P \tag{2.6}$$

where R^*_r and R_r are the single mode spontaneous and radiative recombination rates, where P is the photon density. f_1 and f_2 are usually described by Fermi-Dirac statistics. Under quasi-equilibrium conditions each state has its own occupation probability:

$$f_1 = \frac{1}{1 + \exp\left(\frac{E_1 - E_{F_v}}{k_B T}\right)} \tag{2.7}$$

$$f_2 = \frac{1}{1 + \exp\left(\frac{E_2 - E_{F_c}}{k_B T}\right)} \tag{2.8}$$

where E_1 and E_2 is the energy of states 1 and 2, E_{F_c} and E_{F_v} are the conduction and valence band quasi-Fermi levels and k_B is the Boltzmann constant [32].

We see from equation (2.6) that in order to have net stimulated emission we require $f_2 - f_1 > 0$. We can show by subtracting equation (2.7) from equation (2.8)

that this requires

$$\Delta E_F > E_{21} \tag{2.9}$$

where ΔE_F is the difference between the quasi-Fermi levels E_{F_c} and E_{F_v} and where the bandgap energy is written using equation (2.1). This is the Bernard-Duraffourg condition for population inversion [33]: the stimulated emission rate is larger than the absorption rate when the quasi-Fermi levels are separated by more than the bandgap energy.

2.3.2 The Threshold Condition

As outlined above, a laser requires gain and optical feedback. In a diode laser a forward biased pn-junction is used to inject electrons and holes to generate a population inversion and optical gain in the material. The Fabry-Pérot cavity provides feedback by allowing a photon density to build up in the cavity. In a Fabry-Pérot diode laser photons are amplified as they travel back and forth many times before leaving the cavity. When the amplitude and phase of the electric field are unchanged after a round trip as the gain has compensated for the losses, oscillations occurs and the laser starts to emit coherent radiation as the threshold is reached.

The threshold condition for a Fabry-Pérot laser can be derived using the scattering matrix formalism [32]. We consider the etalon of length L with mirror reflectivities r_1 and r_2 in Fig. 2.3, with a complex propagation constant β and inputs a_1 and a_2, and outputs b_1 and b_2 and write

$$\begin{pmatrix} b_1 \\ b_2 \end{pmatrix} = \begin{pmatrix} S_{11} & S_{12} \\ S_{21} & S_{22} \end{pmatrix} \begin{pmatrix} a_1 \\ a_2 \end{pmatrix} \tag{2.10}$$

We can rewrite equation (2.10) as

$$\begin{aligned} b_1 &= S_{11}a_1 + S_{12}a_2 \\ b_2 &= S_{21}a_1 + S_{22}a_2 \end{aligned} \tag{2.11}$$

Assuming the etalon is not injected from the right ($a_2 = 0$), the element $S_{21} = \frac{b_2}{a_1}$, where

$$S_{21} = \frac{t_1 t_2 exp(-i\beta L)}{1 - r_1 r_2 exp(-2i\beta L)} \tag{2.12}$$

with $r_1 r_2 = R$. When the denominator of equation (2.12) tends to zero, the condition for a finite transmitted amplitude for zero incident field is obtained and can be written as

$$Rexp(-2i\beta L) = 1 \tag{2.13}$$

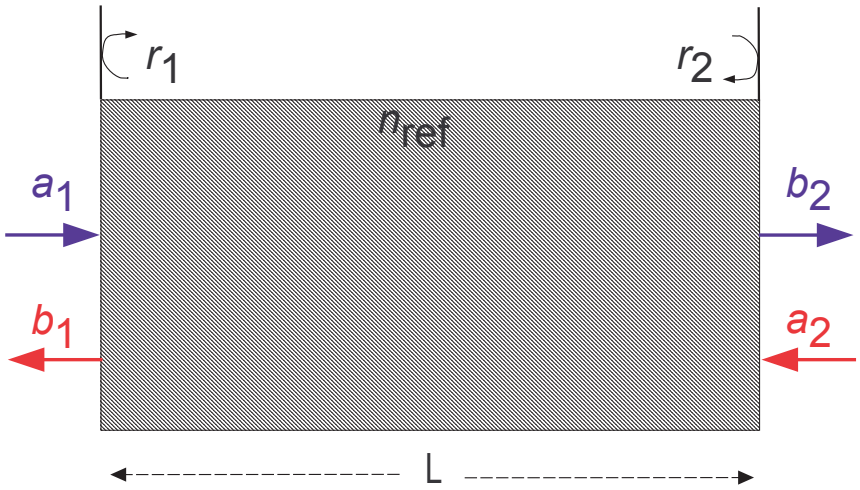

Figure 2.3: Fabry-Pérot etalon of length L and refractive index, n_{ref} with inputs a_i and outputs b_i are for $i = 1,2$.

In this condition oscillation occurs and the threshold is reached. At threshold the amplitude and phase of the electric field are unchanged after a round trip as the modal gain has compensated for the losses.
Assuming L is greater than or equal to the wavelength, λ, β can be written as a real part, β_r, and imaginary part, β_i, as

$$\beta = \beta_r + i\beta_i = \frac{2\pi n_{ref}}{\lambda} + \frac{i}{2}(\Gamma g - \alpha_i) \tag{2.14}$$

where n_{ref} is the refractive index of the mode and Γg and α_i are the transverse modal gain and internal loss respectively.
Substituting equation (2.14) into equation (2.13) and separating the real and imaginary parts we obtain

$$R \exp\left[-2i\left(\frac{2\pi n_{ref}}{\lambda}L\right)\right] \exp((\Gamma g - \alpha_i)L) = 1 \tag{2.15}$$

where the first exponential term describes the phase, where $(-\beta_r L)$ is the phase shift after a single pass, and the second term describes the magnitude of the electric field. Considering the magnitude of the electric field term, we obtain the threshold

condition by solving for Γg_{th}

$$\Gamma g_{th} = \alpha_i + \frac{1}{L} \ln\left(\frac{1}{R}\right) = \alpha_i + \alpha_m \tag{2.16}$$

where α_m are the mirror losses.

2.3.3 Basic Edge-Emitting Diode Laser Designs

The most basic design for an edge-emitting diode laser is an oxide stripe (OS) laser, shown schematically in the top panel of Fig. 2.4. This gain-guided design has only weak carrier and optical confinement in the plane perpendicular to the growth direction, due to a small current-induced refractive index change in the electrically pumped region [34].

Index-guided lasers have improved in-plane optical and carrier confinement. In an index-guided laser, such as a ridge waveguide (RW) laser shown schematically in the middle panel of Fig. 2.4, the optical and carrier confinement is due to a lateral index step at the interface between the semiconductor cladding and dielectric around the waveguide [32]. A buried heterostructure (BH) laser is a strongly

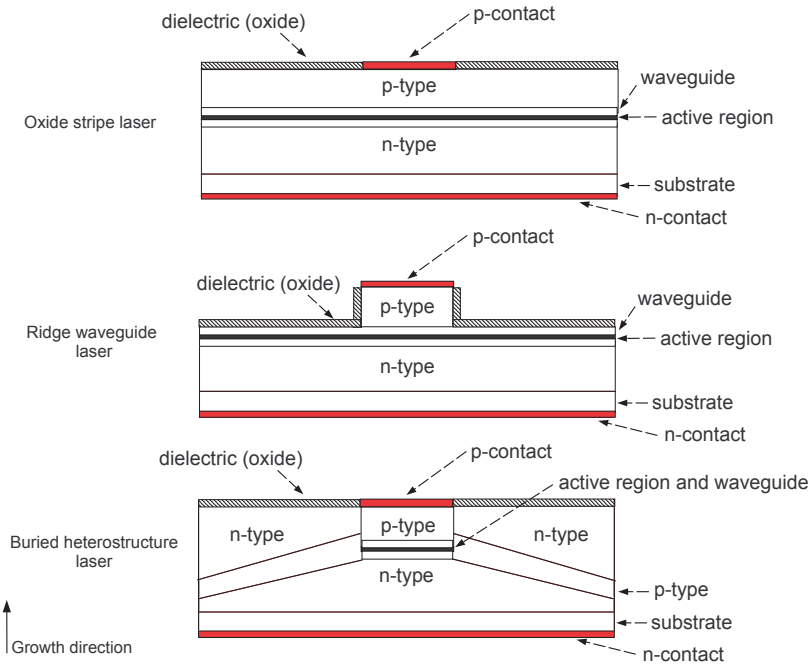

Figure 2.4: Schema of the cross section of an oxide stripe (OS) laser (top), for a ridge waveguide (RW) laser (middle) and for a buried heterostructure (BH) (bottom).

index-guided laser. In BH lasers the active region is bounded both parallel and perpendicular to the junction by layers with a lower refractive index. The layers, which are perpendicular to the growth direction, are doped with doping opposite to that in the active region, as seen schematically in the bottom panel of Fig. 2.4. Processing a BH device is more complex than either OS or RW devices, as it involves regrowth on etched surfaces. However, although BH lasers are more difficult to fabricate, they are widely used because they have improved performance over both RW and OS lasers. One of the ways in which RW and OS lasers differ from BH lasers is the presence of current spreading, which will be explained below.

2.4 Laser Light-Current Characteristics

In this section we consider the light current (LI) characteristics of a laser measured at the facet. From the LI characteristics we extract two figures of merit in lasers, the threshold current and the external differential quantum efficiency.

2.4.1 The Threshold Current

The threshold current is the current which must be injected into a laser diode for the modal gain to equal the total losses. Diode lasers with temperature insensitive threshold currents are desirable for telecom applications. Currently thermoelectric coolers have to be used as the threshold current, I_{th}, of most diode lasers is very temperature sensitive between 20 °C and 100 °C. The overall temperature dependence of I_{th} in most diode lasers can be well described over a limited temperature range by an empirical formula [9]

$$I_{th} = I_0 \exp\left(\frac{T}{T_0}\right) \tag{2.17}$$

where T and T_0 are in Kelvin. If we rewrite equation (2.17) we can evaluate the characteristic temperature, T_0, from the slope of a $ln(I_{th})$ versus temperature plot. T_0 is used as a figure of merit for lasers, with a high value of T_0 describing a weak temperature dependence of I_{th}.

2.4.2 Types of Efficiencies

We begin by considering the internal efficiency, η_i, which is the ratio of the radiative current to the total current. It is used when working with lasers below threshold. We now define η_d^{int}, the internal differential quantum efficiency, which is the ratio of the number of photons generated per second in the lasing mode to the total

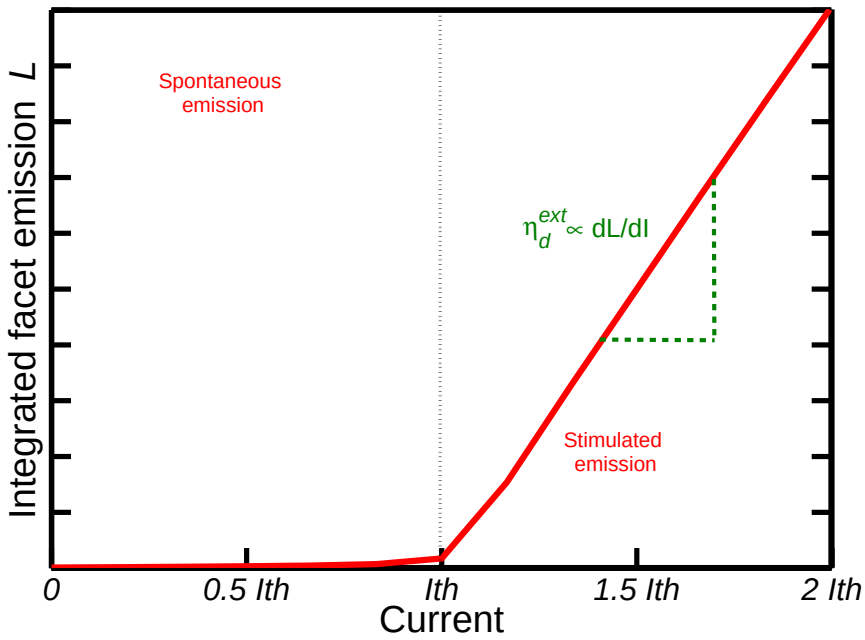

Figure 2.5: Plot of the integrated total emitted optical power, L, of a laser as a function of current. η_d^{ext} is proportional to the slope above threshold.

number of additional carriers injected per second above threshold. This is an above threshold definition of η_i. In an ideal laser, the carrier density clamps at threshold and all the extra carriers are injected into the active region above threshold and will contribute to the stimulated emission, that is, $\eta_d^{int} = 1$.
The external differential quantum efficiency, η_d^{ext}, is the number of photons in the lasing mode collected at the facets to the total number of injected carriers above threshold, and can be related to η_d^{int} and the total emitted optical power, L, through equation (2.18).

$$\eta_d^{ext} = \eta_d^{int} \frac{\alpha_m}{(\alpha_i + \alpha_m)} = \frac{q}{h\nu} \frac{dL}{dI} \tag{2.18}$$

So we can measure η_d^{ext} from the slope of an L versus current above threshold plot as illustrated in Fig. 2.5.

2.5 Density of States

When studying the electronic and optical properties of semiconductor lasers it can be useful to know both the number of states and their energy distribution [32, 34–36], i.e. the density of states per unit energy. It is required for example to calculate

the material gain or the spontaneous emission rate. Changing the quantum confinement can change the form of the density of states near a band edge as illustrated in Fig. 2.6. Since quantum wells were proposed in the early 1970s there has been a lot interest, both theoretically and experimentally, in understanding how the changes in the density of states affect the overall laser characteristics.
This section includes a derivation of the density of states per unit energy, per unit volume, $\rho_{3D}(E)$, in a bulk material, followed by an overview of how the density of states is modified as the carriers become increasingly confined in a quantum well, quantum wire and quantum dot.

2.5.1 Density of States in Bulk

If the dimensions L_x, L_y and L_z are large ($\geq$0.1 μm), the states are uniformly distributed in k-space and the spacing between allowed k values, $(\frac{2\pi l}{L_x}, \frac{2\pi m}{L_y}, \frac{2\pi n}{L_z})$, where l, m and n are integers, is very small. The number of states, N, in the range $k \rightarrow k + dk$ is

$$N = D(k)dk = D(E)dE \tag{2.19}$$

where $D(E)$ is the density of states per unit energy. We assume a parabolic dispersion relation

$$E = \frac{\hbar^2 k^2}{2m^*}, \tag{2.20}$$

a bulk volume V, and write N as the volume of shell of radius k with thickness dk, $4\pi k^2 dk$, divided by the volume of a single state, $\frac{8\pi^3}{V}$. We include a factor of 2 to account for the spin.

$$N = D(k)dk = 2(\frac{Vk^2 dk}{2\pi^2}) \tag{2.21}$$

Writing $D(E)$ using equation (2.19) and substituting N from equation (2.21), we obtain

$$D(E) = \frac{2V}{4\pi^2}(\frac{2m^*}{\hbar^2})^{3/2}\sqrt{E} \tag{2.22}$$

which has units of inverse energy. Dividing $D(E)$ by the volume V we obtain $\rho_{3D}(E)$, the density of states per unit energy per unit volume, shown schematically in the bottom left panel of Fig. 2.6.

$$\rho_{3D}(E) = \frac{1}{2\pi^2}(\frac{2m^*}{\hbar^2})^{3/2}\sqrt{E} \tag{2.23}$$

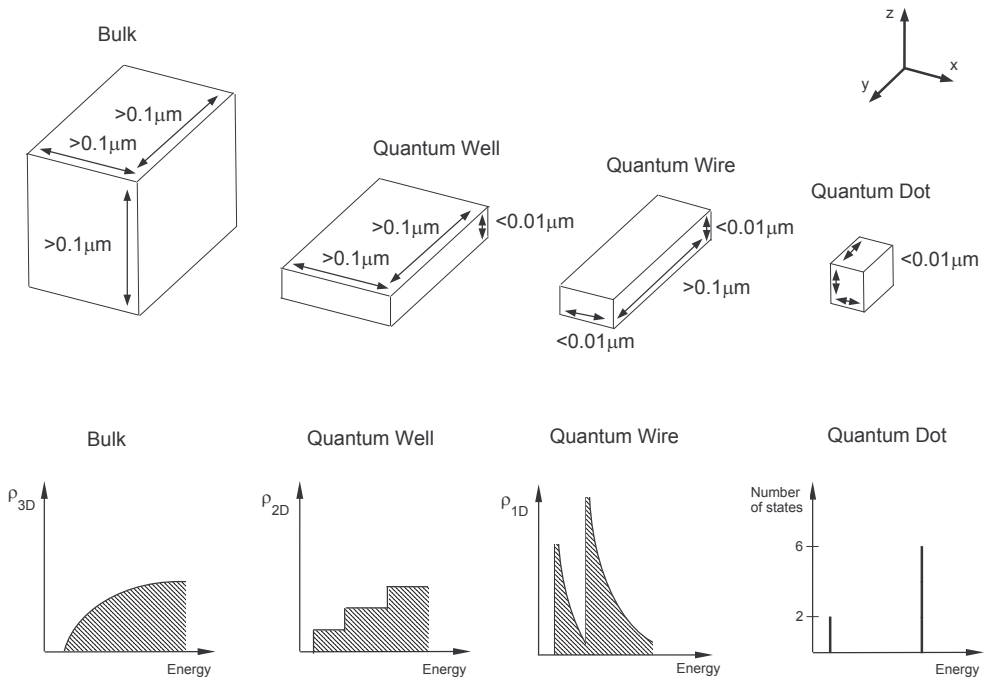

Figure 2.6: Schema of the change in size as well as in the density of states from left to right in going from for bulk to quantum well to quantum wire to quantum dot.

2.5.2 Density of States in Quantum Well, Wire and Dot

Reducing one of the dimensions, say L_z, to a size of the order of the de Broglie wavelength, we obtain a quantum well, shown schematically in the second top panel of Fig. 2.6. The carriers are free to move in the $x-y$ plane, as in bulk, but are quantised along k_z and form subbands. Taking the density of states as a function of k, $D(k)$, as in equation (2.19) for an area, $A = L_x L_y$, we now have that the number of states, N, between k and $k+dk$ is proportional to $2\pi k dk$, compared to $4\pi k^2 dk$ in the bulk case. Following a similar process as outlined in section 2.5.1 for bulk, we then obtain the density of states per unit energy per unit area for one sub band as

$$\rho_{2D}^{1sub}(E) = \frac{m^*}{\pi\hbar^2} \tag{2.24}$$

To obtain $\rho_{2D}(E)$, shown schematically in the second bottom panel from the left in Fig. 2.6 for $N = 3$ sub bands, we use the Heaviside step function $H(x - x_0)$

where

$$H(x - x_0) = \begin{cases} 0 & \text{if } x < x_0 \\ 1 & \text{if } x \geq x_0 \end{cases} \tag{2.25}$$

to write

$$\rho_{2D}(E) = \frac{m^*}{\pi\hbar^2} \sum_{n=1}^{N} H(E - E_n) \tag{2.26}$$

for $E \geq E_n$, where E_n is the energy of the n^{th} confined state.
We now restrict the carrier momentum to a single dimension, say along y, by reducing x and z to the order of the electron wavelength and obtain a quantum wire, shown schematically in the third top panel of Fig. 2.6. In this case electron momentum is quantised along x and z and the density of states is derived per unit length. Following a similar analysis as for bulk we obtain the density of states per unit energy per unit length for one sub band as [34]

$$\rho_{1D}^{1sub}(E) = 2\frac{\hbar^2}{m^*}\sqrt{\frac{2m^*}{\hbar^2}}\frac{1}{\sqrt{(E - E_{n_x} - E_{n_z})}} \tag{2.27}$$

for $E > E_{n_x} + E_{n_z}$. As with the density of states in a quantum well, the Heaviside step function is used for a number of sub bands and $\rho_{1D}(E)$ is illustrated in the third bottom panel from the left in Fig. 2.6 for two sub bands along z, the shortest wire dimension.

$$\rho_{1D}(E) = 2\frac{\hbar^2}{m^*}\sqrt{\frac{2m^*}{\hbar^2}} \sum_{n_x,n_y=1}^{M,N} \frac{H(E - E_{n_x} - E_{n_z})}{\sqrt{(E - E_{n_x} - E_{n_z})}} \tag{2.28}$$

for $E > E_{n_x} + E_{n_z}$.
Reducing all three dimensions, L_x, L_y and L_z, to sizes of the order of the de Broglie wavelength we obtain a quantum dot, where electron momentum is quantised in all three dimensions, and hence to a discrete, atom-like, density of states. Illustrated in the bottom right most bottom panel of Fig. 2.6 are the ground and first excited states of a cube shaped quantum dot, where the excited state is made as the sum of three states, which each have 2 spins. Overall, reducing the dimensions of the material changes both the form of the density of states and also the total number of states per unit energy in the active region of the laser. There has been significant interest in how these changes affect the overall laser characteristics: a major theme of this thesis is to investigate the influence of elongated quantum dots - referred to as *quantum dashes* - on the characteristics of actual 1.5 μm InP-based lasers.

2.6 Recombination Processes in Diode Lasers

In this section we first focus on the spontaneous emission rate and its polarization dependence. Next we consider the non-radiative recombination processes and optical losses present in real diode lasers which operate at 1.5 μm.

2.6.1 The Spontaneous Emission Rate

The total spontaneous emission rate per unit energy, per unit active volume, R_{sp}, is obtained by summing R^*_{sp} over all optical modes. Assuming we have a quantum dot with n_c conduction band states and n_v valence band states, we can write R_{sp} as

$$R_{sp}(p, h\nu) \propto h\nu \sum_{i}^{n_c} \sum_{j}^{n_v} |M^p_{i,j}|^2 G(E_{c,i} - E_{v,j} - h\nu) f_c(E_{c,i})(1 - f_v(E_{v,j})) \quad (2.29)$$

where p indicates the polarization direction and $h\nu$ is the photon energy [5]. $M^p_{i,j}$ is the momentum matrix element with polarization p for the ij^{th} transition with energy separation $E_{c,i} - E_{v,j}$. $G(x) = \frac{1}{\sigma\sqrt{2\Pi}} exp(\frac{-(x-\mu)^2}{2\sigma^2})$, where where μ is the mean, σ is the standard deviation, is a Gaussian broadening function which quantifies the amount of inhomogeneous broadening present in an ensemble of real quantum dots. This broadening is due to the presence of dash size dispersion and composition fluctuations in the ensemble.

The Polarization Dependence of R_{sp}

The transition rate of an electron in a state 2 to a continuum of final states 1 in the presence of a harmonic perturbation, such as an electromagnetic field, which is given by Fermi's Golden Rule [32], is proportional to

$$\frac{2\pi}{\hbar} |H'_{21}|^2 \quad (2.30)$$

where $|H'_{21}|^2$ is the square of the matrix element evaluated at E_{21}, which determines the strength of the interaction between the initial and final states and the optical field. The matrix element H'_{21}, is given by

$$H'_{21} = \int_V \psi^*_2 H'_r \psi_1 d^3r \quad (2.31)$$

where ψ_1 and ψ_2 are the wavefuntions of the isolated electron in states 1 and 2, while H'_r is the Hamiltonian characterising the electronic state and its interaction

with the electromagnetic field.

In a low dimensional structure such as a quantum well, ψ_1 and ψ_2 can be decoupled into a slowly varying envelope function, $F(\mathbf{r})$, which satisfies Schrödinger's equation at a macroscopic level, and a complex Bloch function, $u(\mathbf{r})$, which repeats itself over each unit cell and satisfies Schrödinger's equation at an atomic level. The difference between $F(\mathbf{r})$ and $u(\mathbf{r})$ can be seen schematically in Fig. 2.7. We can therefore write

$$\psi_1 = F_v(\mathbf{r})u_v(\mathbf{r}) \tag{2.32}$$

$$\psi_2 = F_c(\mathbf{r})u_c(\mathbf{r}) \tag{2.33}$$

$H_r^{'}$ is related to the vector potential $A(\mathbf{r})$ and can be written as [32]

$$H_r^{'} = \frac{qA(\mathbf{r})}{2m_0}(\mathbf{e}\cdot\mathbf{p}) \tag{2.34}$$

where the unit vector $\mathbf{e}$ gives the polarization direction and $\mathbf{p}$ is the momentum operator. If we substitute equations (2.32), (2.33) and (2.34) into equation (2.31) and assuming that the vector potential is a plane wave with magnitude A_0 and no

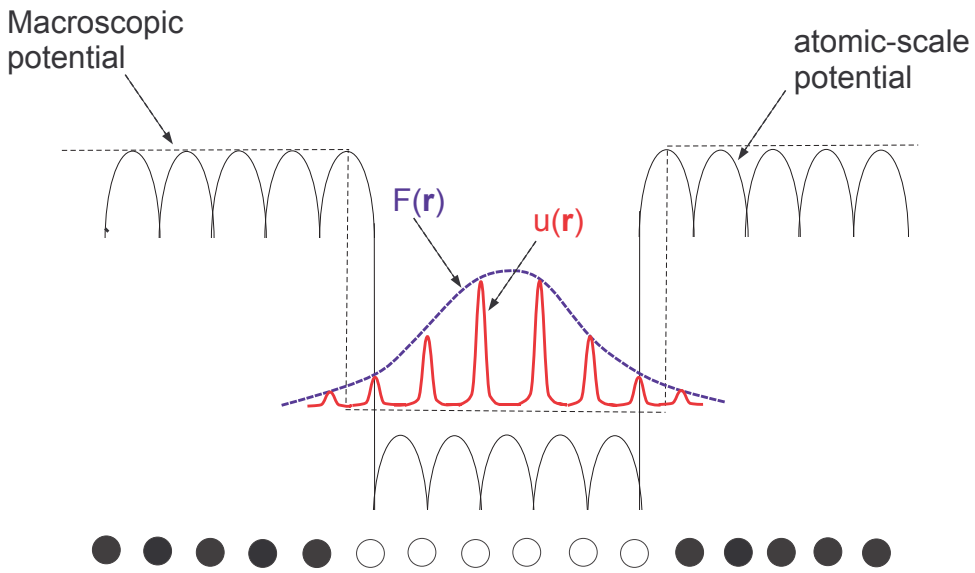

Figure 2.7: Schema of a quantum well potential and the corresponding lowest energy wavefunction.

spatial dependence, we obtain

$$H'_{21} = \frac{qA_0}{2m_0}|M_T| \tag{2.35}$$

where $|M_T|$ is the transition matrix element and is equal to the product of the overlap integral, $< F_v(\mathbf{r})|F_c(\mathbf{r}) >$, and the momentum matrix element, $|M| = < u_c(\mathbf{r})|\mathbf{e}\cdot\mathbf{p}|u_v(\mathbf{r}) >$, which gives the polarization dependence of the interaction. We substitute equation (2.35) into equation (2.30) and can write $|M|^2 = S_x|M^x|^2 + S_y|M^y|^2 + S_z|M^z|^2$, where S_i is the relative transition strength at the band edge along the i^{th} direction. The polarization dependence of $|M|^2$ does not reveal itself in bulk due to a uniform distribution of electron momentum as seen schematically in the left panel of Fig. 2.8. However when we form a quantum well, the degeneracy of the heavy-hole (HH) and light-hole (LH) levels is lifted, with the HH states lying above the LH states in unstrained and compressively strained quantum wells. When light is emitted (absorbed) by recombination into (from) a pure HH state in a quantum well, the emitted (absorbed) photon is polarized in the $x-y$ plane with $S_x = S_y = \frac{1}{2}$ and $S_z = 0$, giving what is referred to as TE-polarized emission (absorption). By contrast, $S_z = \frac{2}{3}$ and $S_x = S_y = \frac{1}{6}$ for a pure LH state, so that transitions involving LH states are predominantly TM-polarized, with the electric field pointing along the z-direction.

In a symmetric quantum wire, the band edge transition matrix element is enhanced along the wire axis, and suppressed equally along the two other directions. In an asymmetric quantum wire the electron momentum is anisotropic in all three directions. The quantum dashes, which we will be investigating in this thesis, can be approximated as asymmetric quantum wires [37]. For an asymmetric quantum wire with $L_x > L_z$ (see Fig. 2.8), we find $S_x > S_z$ and for sufficient asymmetry, $S_z \to 0$, suppressing TM-polarized emission (absorption) at the band edge.

If we have a quantum dash with the long axis along y and define transitions along that direction as p_1-polarized and transitions along the shorter in-plane axis x as p_2-polarized, we can simplify and use equation (2.29) to write the spontaneous emission rates with polarization p_1 and p_2 as

$$R_{sp}(p_1, h\nu) \propto \sum_{i,j}^{n_c,n_v} |M_{i,j}^{p_1}|^2 f_c(E_{c,i})(1 - f_v(E_{v,j})) \tag{2.36}$$

$$R_{sp}(p_2, h\nu) \propto \sum_{i,j}^{n_c,n_v} |M_{i,j}^{p_2}|^2 f_c(E_{c,i})(1 - f_v(E_{v,j})) \tag{2.37}$$

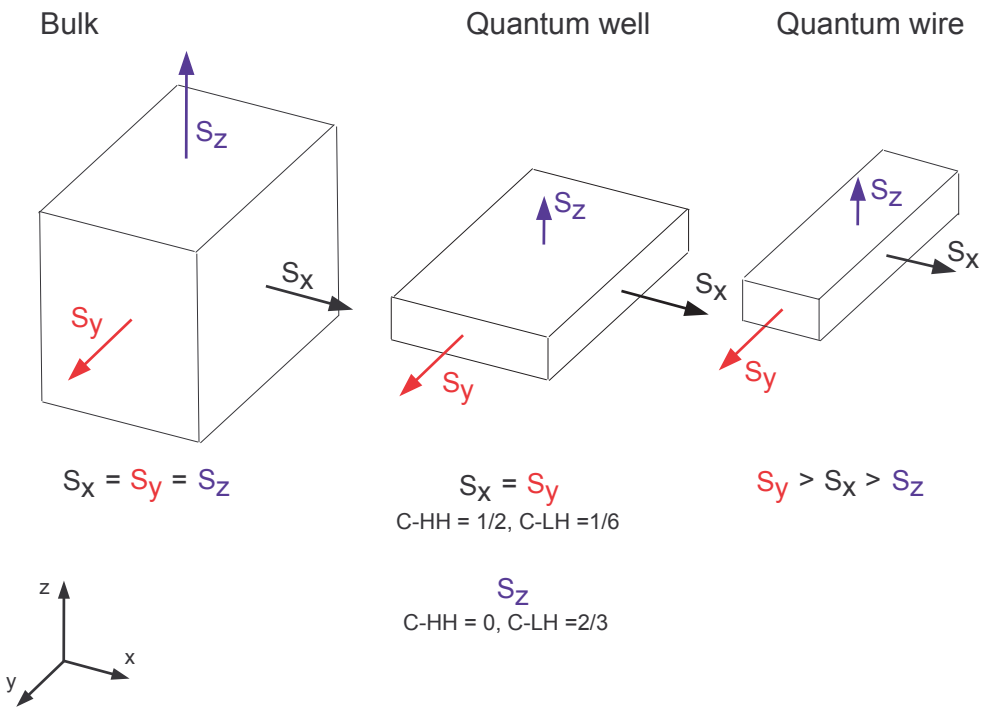

Figure 2.8: Illustration showing S, the relative transition strengths for bulk (left panel), quantum well (middle panel) and quantum wire (right panel) at the band edge.

The quasi-Fermi factors, $f_c(E_{c,i})(1 - f_v(E_{v,j}))$, have no polarization dependence, so we can write the ratio, r, of the spontaneous emission rates along y and x as

$$r = \frac{R_{sp}^{p_1}(h\nu)}{R_{sp}^{p_2}(h\nu)} = \frac{\sum_{i,j}^{n_c,n_v} |M_{i,j}^{p_1}|^2}{\sum_{i,j}^{n_c,n_v} |M_{i,j}^{p_2}|^2} \tag{2.38}$$

Using equation (2.38) we can quantify the anisotropy of the square of the momentum matrix element experimentally.

2.6.2 Carrier Recombination Processes in Diode Lasers

Although a lot of work has been carried out on semiconductor lasers operating at telecoms wavelengths, recombination processes still make them temperature sensitive. In this section we describe four carrier recombination processes, shown schematically in Fig. 2.9, which can occur in diode lasers.

Monomolecular defect-related recombination, shown schematically in the left most panel of Fig. 2.9, can play a dominant role at low carrier densities. Defects are not intrinsic and can be due to vacancies, impurities or dislocations in the semiconductor crystal, which leads to the creation of the defect states in the bandgap through which carriers can recombine non-radiatively. The overall recombina-

tion rate is assumed to be proportional to the carrier density, n. In high quality undoped material defect-related recombination is negligible. Radiative recombination is an intrinsic process involving two carriers. The integrated spontaneous emission, L_{SE}, is obtained by integrating $R_{sp}(h\nu)$ as a function of energy and is a measure of the radiative current, with $I_{rad} = qV(Bn^2)$ in an undoped material. Unlike defect-related recombination, band-to-band Auger recombination is an intrinsic non-radiative process [9, 32, 35, 36]. There are a number of possible Auger processes, all of which involve three carriers. Considering the CHCC Auger recombination process, shown schematically in the third panel of Fig. 2.9, the energy created by the annihilation of a **C**onduction band electron – valence band heavy **H**ole pair, (1) and (2), is transferred to a second **C**onduction band electron, (3), which is promoted to a higher **C**onduction band energy state. The third carrier then looses the energy by the non-radiative emission of phonons to return to its original state. Auger recombination is dependent on the quasi-Fermi level separation as this affects whether carrier (1) is available. Auger recombination is also influenced by the valence band structure as this governs the availability of carrier (2). Lastly Auger recombination is dependent on the bandgap of the material, as this governs the energy given to the third carrier and can be negligible in shorter wavelength lasers. I_{Auger} has a stronger dependence on the carrier density ($\propto n^3$) than either defect-related or radiative recombination and can become dominant for larger carrier densities.

In an ideal laser the carriers should be confined to the active region. However carriers can thermally escape from the active region and recombine radiatively or non-radiatively in the barrier or cladding regions, as illustrated in the right most panel of Fig. 2.9. Leakage currents, $I_{leakage}$, which may not clamp at threshold, lead to a decrease in η_d^{int}, the internal differential quantum efficiency of the laser [32, 38]. The internal differential quantum efficiency in RW and OS lasers are also reduced by current spreading, where electron - hole pairs recombine in

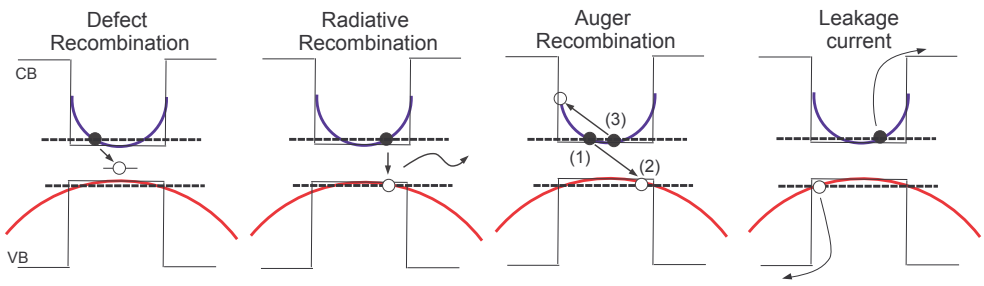

Figure 2.9: Schema of the carrier recombination processes which can occur in a forward biased semiconductor laser

the region beyond the contacts. Current spreading also leads to an increase in the threshold current density but is expected to be negligible in BH lasers.

The z analysis

The method, which we refer to as the z analysis [39], assumes that the carrier distributions are described by Boltzmann statistics and can be used to evaluate the dominant carrier recombination process in a diode laser at threshold. This involves measuring the variation of the radiative current, I_{rad}, with total current, I_{tot}, as a function of temperature. The analysis assumes that I_{tot} varies with carrier density, n, as [9, 39–41]

$$I_{tot} = qV(An + Bn^2 + Cn^3) + I_{leakage} \tag{2.39}$$

where $qVAn$ describes monomolecular defect-related recombination, $qVBn^2$ is the radiative current, $qVCn^3$ is due to intrinsic Auger recombination, and $I_{leakage}$ is due to leakage current paths.
Assuming negligible leakage currents, the total current can be written as $I_{tot} \propto n^z$. If the device is dominated by defect-related non-radiative recombination, $z \sim 1$, while $z \sim 2$ in a radiatively dominated device, and $z \sim 3$ if non-radiative Auger recombination is dominant. Within this model, $n^2 \propto I_{rad}$, so $I_{tot} \propto (I_{rad}^{1/2})^z$. Therefore the dominant recombination process can be identified by finding the slope, z, of a plot of $ln(I_{tot})$ versus $ln(I_{rad}^{1/2})$.

2.7 Optical Losses in Diode Lasers

Lasers operating at 1.5 μm also suffer from a major optical loss mechanism called intervalence band absorption (IVBA), which is undesirable as it leads to a loss of carriers and photons. In IVBA a photon traveling in the laser gets reabsorbed and the energy is transferred to an electron in the spin-split-off (SO) band, which gets promoted to an injected hole state in the HH band, as seen schematically in Fig. 2.10. In 1.5 μm lasers the photon is reabsorbed a distance from the Γ point, as the energy gap is larger than the SO splitting. IVBA may also involve phonons and is influenced by the temperature and the valence band structure. IVBA increases with temperature as the population of hole states away from the Γ point and phonons increases.

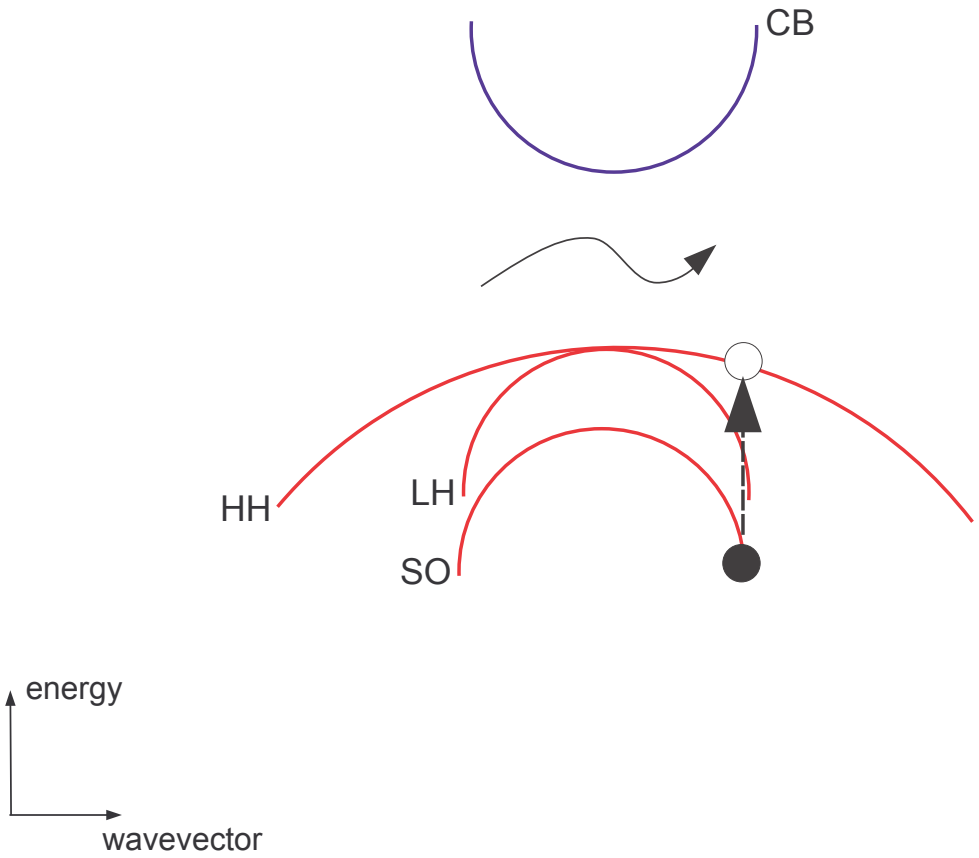

Figure 2.10: Illustration of intervalence band absorption (IVBA), where a photon is reabsorbed leading to the promotion of an electron from the spin-split-off band to an injected hole state in the heavy hole band.

2.8 Summary

This chapter contains an overview of the relevant background theory of semiconductor lasers and begins with a history of the diode laser. The requirements to achieve lasing, an overview of three basic edge emitting laser designs and the laser light-current characteristics are reviewed in section 2.3 and 2.4. Section 2.5 introduces the concept of density of states for bulk, and highlights how the density of states is modified by changing the dimensions of the material and hence the carrier confinement. The final part of this chapter included in section 2.6 involves the presentation of the recombination processes and loss mechanisms present in diode lasers. We consider the spontaneous emission rate and its polarization dependence. We then review the effects of intrinsic and non-intrinsic processes on the laser light-current characteristics and show how to evaluate the dominant recombination process at threshold from the integrated spontaneous emission. Lastly we review an optical loss which can be important in diode lasers emitting at 1.5 μm.

Chapter 3

Experimental methods

3.1 Introduction

As outlined in chapter 1 the main theme of this thesis is the analysis of the optical characteristics and identification of the recombination processes present in quantum dash and quantum dot semiconductor lasers. Much of this work involves measuring polarized and unpolarized unamplified spontaneous emission (SE) spectra as well as carrying out polarized edge-photovoltage (E-PV) spectroscopy measurements in order to analyse the electronic structure of the semiconductor material and its consequence on the optical properties and recombination processes present in lasers. This chapter describes the main experimental techniques used in this thesis.

In order to collect unamplified SE, the measurement must be made in a direction perpendicular to the laser waveguide [42]. This usually requires the etching of windows in either the substrate of the laser or in the top contact. First, in section 3.2, we will describe the technique used to create the windows through which unamplified spontaneous emission is collected. Next we describe the polarized E-PV spectroscopy method as well as the method used to collect polarized and unpolarized unamplified SE spectra. Polarized E-PV and SE spectral measurements are linearly polarized along the three main axis, with $TE_{(1-10)}$, $TE_{(110)}$ and TM-polarized along the (1-10), (110) and (001) crystal planes respectively. In section 3.3 we describe polarized E-PV spectroscopy in detail and show that by coupling light into the facet in the samples being analysed, we can only have access to the $TE_{(1-10)}$ and TM components of the polarized E-PV spectrum. Having reviewed SE and possible measurement methods in section 3.4, we show in section 3.5, that in order to have access to both TE components we must measure polarized unamplified SE spectra through a window milled in the top contact of the laser. In this work we also collect SE in order to compare the radiative and

non-radiative processes as a function of temperature. This requires using a cryostat set up to measure how facet and integrated spontaneous emission vary as a function of current between 40 – 330 K. The current range used covers below and above threshold enabling us to identify how the threshold current and its radiative component change with temperature. The technique, as well as the set up used for this measurement, are described in detail in section 3.6.
In summary this chapter reviews of the main experimental methods used in this thesis. Section 3.2 provides information about the milling carried out using a focused ion beam microscope (FIB) to etch transparent windows into the laser contacts. Section 3.3 describes room temperature polarized E-PV spectroscopy and the set up used to measure polarized E-PV spectra. A brief overview of the methods used to measure SE are included in section 3.4. Next the set up and method used to measure room temperature polarized SE spectra are described in section 3.5. An outline is then given in section 3.6 of the experimental set up and method used to collect facet and spontaneous emission as a function of current and temperature. Section 3.7 provides a summary of the work presented in this chapter.

3.2 Window Milling

In this section, a review of the window milling process is presented. Windows are milled in the p and n-contacts of devices using a FEI Vectra 200 DE Focused Ion Beam (FIB) system. A FIB [43] works in a very similar way to a scanning electron microscope, except that it uses a finely focused beam of of energetic (30 keV) gallium (Ga+) ions instead of electrons. The spot diameter is 10 nm. During operation, Ga flows from a reservoir to the tip of a tungsten needle. A large negative potential between the tungsten needle and the extraction electrode generates a large electric field at the needle tip leading to the emission of the gallium ions. The ion beam is then collimated and focused onto the sample. Unlike an electron microscope, the FIB is a destructive process [44, 45], as material at the surface of the sample can be sputtered by high-energy gallium ions as they strike the sample. However at low intensities the FIB can be used as a high magnification microscope for short periods to align the sample and focus the beam before any milling is carried out.

3.2.1 Windows in P-Contact

Devices to be windowed on the p-side are mounted on carriers and wire bonded before milling. In the FIB, contact is made with the metal holder through the

n-contact of the carrier, using a double-sided sticky carbon planchet or using a specially designed mount. The advantage of using the mount is that no acetone is required to break down the glue on the planchet in order to remove the carrier from the holder. The in-plane dimensions of the rectangular window are set at 6μm by 10μm on the FIB user interface. However, window depth cannot be accurately set in the FIB, because the depth is dependent on the ion beam intensity, the type of material used and the length of time for which the material is exposed to the ion beam. The settings of the FIB used in this work are calibrated for the milling of Si, but it has been suggested that InP and the metals that make up the contact, usually titanium, platinum and gold, are milled faster than Si [45–47]. Included below is an investigation carried out to obtain the optimal depth for windows milled on the p-contact of InP-based devices.

Depth of Windows in P-Contact

When milling windows in the p-contact of a device, we aim to achieve a uniform current distribution underneath the windows caused by uniform current spreading. This ensures that the waveguide and optical recombination are not perturbed by the presence of the window.
In order to reliably achieve the correct window depth, a series of large windows of

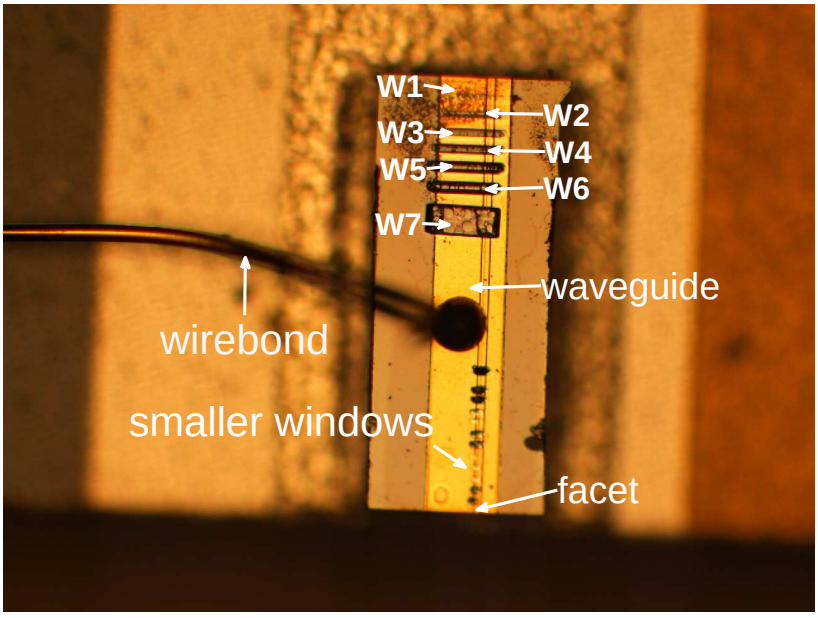

Figure 3.1: Photo of a test device used to measure the depth of the windows in the p-contact milled with the FIB.

different depths were first milled in the p-contact of four test devices. Fig. 3.1 shows a photo of one of the test lasers, where the gold p-contact of the laser is yellow and the oxide is orange. The black disk at the centre of the laser contact is the point at which the wirebond is attached. The vertical lines mark the waveguide of the laser. The small windows below the wirebond were too small to achieve an accurate depth measurement. A larger set of windows, labeled W1-W7 with increasing depth, were milled above the wirebond and their depth was measured using a surface profilometer.

Plotted in Fig. 3.2 is the measured depth versus the depth set in the FIB for the four test devices. Although there is some scatter on the data, the trend is linear and suggests the actual depth measured is ∼10 times larger than the value set in the FIB. This is consistent with the contact metals and InP being milled faster than Si [45–47].

Both sets of windows in Fig. 3.1 have been milled along the waveguide in order to measure SE from them. The left panel of Fig 3.3 shows the same test laser as in Fig. 3.1 under a X32 microscope giving a close up view of windows W2-W7. The test laser is biased using a 2400 Keithley DC source. The window emission measured using an Electrophysics Corp MicronViewer 7290 infrared (IR) camera is shown in the right panel of Fig. 3.3.

Considering first window W2, which has a measured depth of less than ∼1μm,

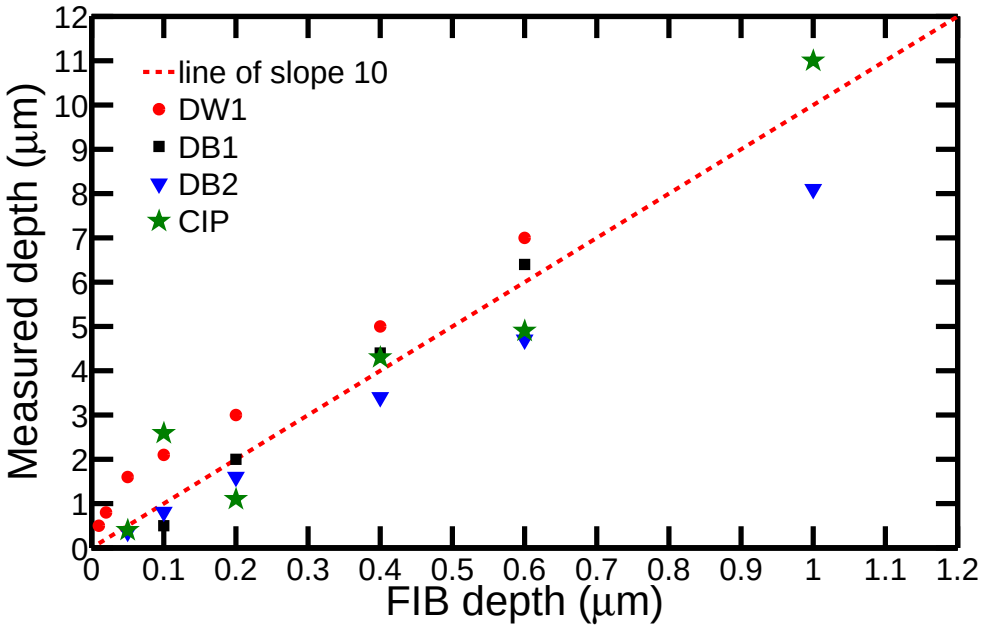

Figure 3.2: Plot of measured surface profilometer depth as a function of the depth set in the FIB for four test samples. The red line has a slope of 10.

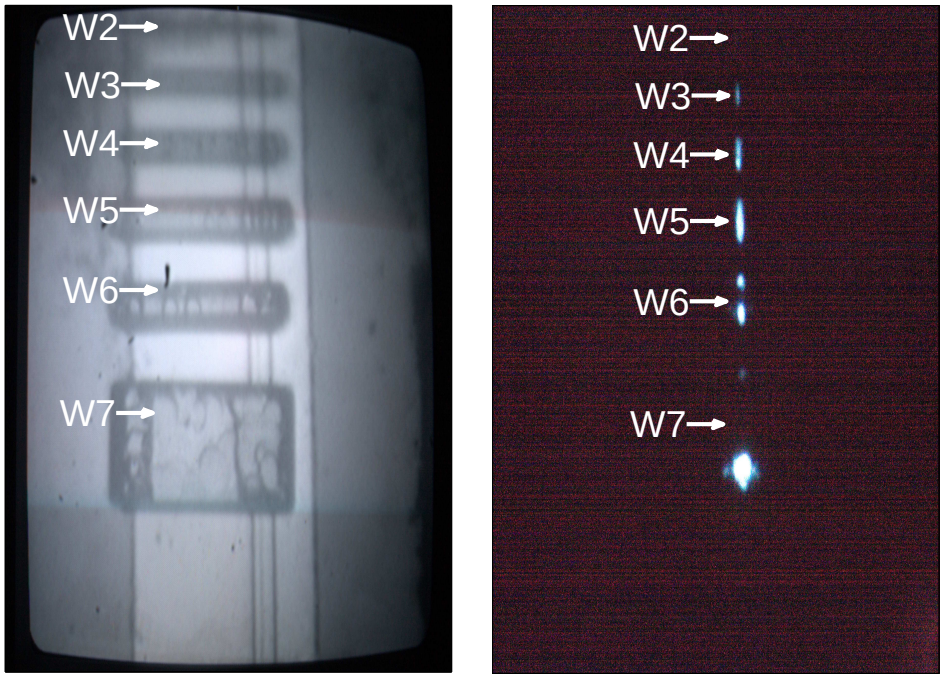

Figure 3.3: Photo of a test device (left panel) and window emission (right panel) from the test device under X32 magnification.

no spontaneous emission is observed, suggesting that W2 is not deep enough to expose any InP. The next three windows (W3-W5) have depths between 1μm and 3μm and have uniform window emission. This indicates a uniform current density underneath these windows. Window W6 is $\sim$5μm deep and in this case the window emission is non-uniform, with no spontaneous emission emitted at the centre of the window. This suggests the absence of current or the presence of a non-radiative recombination site underneath the centre of the window. W7 is the largest and deepest window and the current density is not uniform underneath this window either. The difference in emission strength between both edges of W7 suggests the laser waveguide has been perturbed by W7. When the very bright window emission, closest to the wirebond was spectrally resolved, it was measured to be amplified spontaneous emission, as normally measured through the facet of a laser.

To conclude, a window milled in the p-side of a device must be small and not too deep, to ensure the waveguide is not perturbed and that the current density underneath the window is uniform. The window is milled as close as possible to the centre of the laser, but is dependent on the position of the wire bond(s). The dimensions set in the FIB are 6 μm x 10 μm and 0.1 μm deep, leading to an expected window depth of $\sim$ 1 μm. Emission can be observed from such a window using the X32 microscope and IR camera. However it is hard to make out the

uniformity of the emission due to the small size of the window. The spectrum of the emission from this window confirms the presence of pure unamplified SE only. A photo of one of the lasers with a 6 μm x 10 μm x $\sim$ 1 μm window milled in the p-contact, which is investigated in chapter 4, is included in Fig. 3.4.

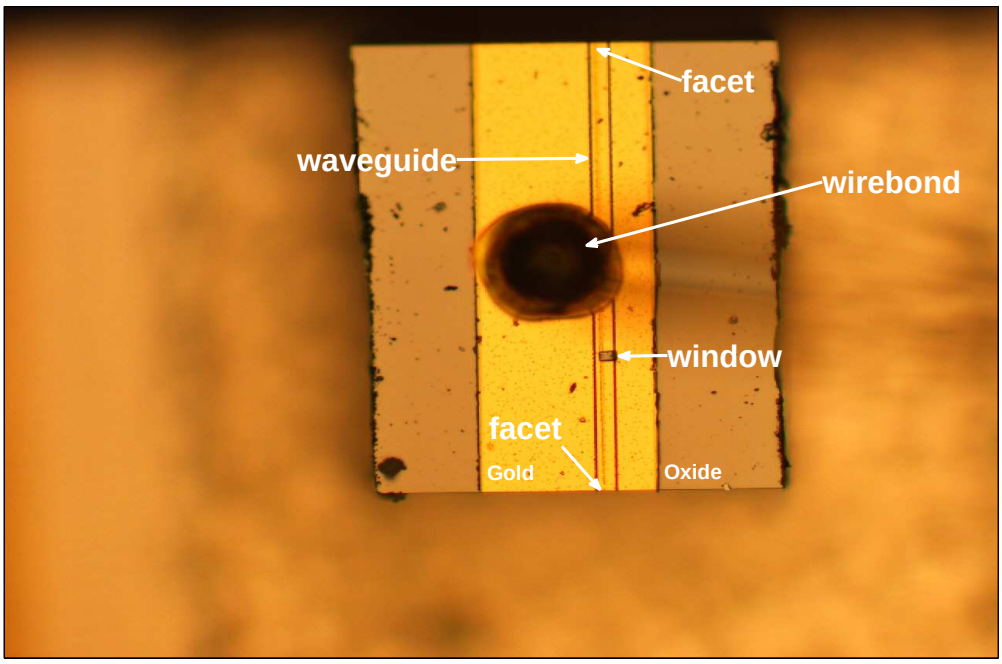

Figure 3.4: Photo of a laser with a window (6μm by 10μm) milled in the p-contact which is investigated in chapter 4. The laser stripe width in 1.5 μm. The large black disk at the centre is the gold ball by which the wire bond is attached to the laser. Some of the wire bond can be seen as an out of focus horizontal line on the right of the photo. The gold p-contact of the laser is yellow and the oxide is orange. The vertical lines mark the waveguide of the laser and the window has been milled along the waveguide close to the centre of the laser.

3.2.2 Windows in N-Contact

Bare laser bars with six lasers per chip are used when milling windows on the n-substrate. The chip is mounted p-side down on a metal holder using a double-sided sticky carbon planchet, before the holder is mounted in the FIB. One large window with long axis aligned perpendicular to the laser cavity is milled on the n-side at the centre of the chip, exposing some active region from all the lasers on the chip. The width of the window is set to 10 μm, as on the p-contact, and the FIB depth is set to 1 μm. Results measured for depth on the p-contact indicate the actual depth of the windows on the n-substrate is $\sim$10 μm. A deep window is not expected to affect the current density in the laser due to the thickness of the substrate. In order to remove the chip from the holder, acetone is used to

break down the glue on the double-sided sticky carbon planchet. Unamplified SE is measured at different points along the window when the lasers on the chip are biased in turn.
In summary, this section provides an overview of the main considerations when milling windows in the p and n-contacts of semiconductor lasers. Windows milled must be small enough in order to ensure uniform current distribution underneath the window. The depth of the window is carefully set when milling on the p-contact, but is less critical when milling on the n-substrate. Care must also be taken when windowing lasers as the FIB mills contact metals and InP $\sim$ 10 times faster than Si.

3.3 Polarized Edge-Photovoltage Spectroscopy

This section includes information about photovoltage (PV) spectroscopy and the set up used to measure polarized E-PV spectra. In this experiment the diode laser is used as a pn photodiode, as described in Ref [48].
When light with energy greater than the bandgap incident on a pn junction, such as the active region of a diode laser, it gets absorbed and electron – hole pairs are generated inside the depletion region. The generated electron and hole are separated by the electric field in the depletion region of the laser active region. When the laser is connected to an external circuit the extra electrons travel through the external circuit to the p-type semiconductor. This photocurrent, and associated photovoltage, can be measured across the laser.
In PV spectroscopy light is incident from the side (S-PV) or the edge (E-PV) of the laser and a step in magnitude of the measured PV spectrum, and the onset of a peak represents the onset of a set of transitions at that energy. PV spectra are used to identify energy states in quantum confined materials, such as quantum well and quantum dots.
By polarizing the light incident on the laser facet E-PV spectroscopy can be used to differentiate between transitions involving heavy hole (HH) and light hole (LH) valence band states [49–53]. As outlined in chapter 2 transitions involving HH states are TE-polarized, while transitions involving LH states are predominantly TM-polarized.

3.3.1 Set Up

The set up used to measure polarized E-PV spectra can be seen schematically in Fig 3.5. The spectrometer used is a SP2150 made by Princeton Instruments, which has a focal length of 150 mm. The entrance and exit slits are vertical and

are operated manually. The grating used has 600 line/mm, is blazed at 1μm and has a 9 nm/mm dispersion.

In this experiment light from a tungsten bulb passes through a pin hole and is collimated by a lens. An iris is placed in the light path to control the amount of light that passes through. A second lens, which has the same f number as the spectrometer, is used to focus the light onto the spectrometer entrance slit. This ensures the grating is filled. The focused white light is collimated by a mirror and reflected onto the diffraction grating, which splits white light into its component wavelengths. The whole collimated diffraction pattern is focused onto the output slit by a second mirror and the slit only lets a small wavelength range through. The wavelength of the light at the output slit depends on the angle of the grating. The spectral range is set as 1000 – 2000 nm by using a low pass filter to remove any higher order energy contributions to the spectrum. The light at the output of spectrometer is polarized and coupled onto the laser facet using a x 40 microscope objective. The microscope objective has a numerical aperture (NA) of 0.65 to maximize the coupling of light into the waveguide. The sample is mounted on an xyz-stage. The coarse adjusting of the stage is manual, with a piezoelectric fine adjustment operated using a Newport ESA-C microdrive controller. By chopping

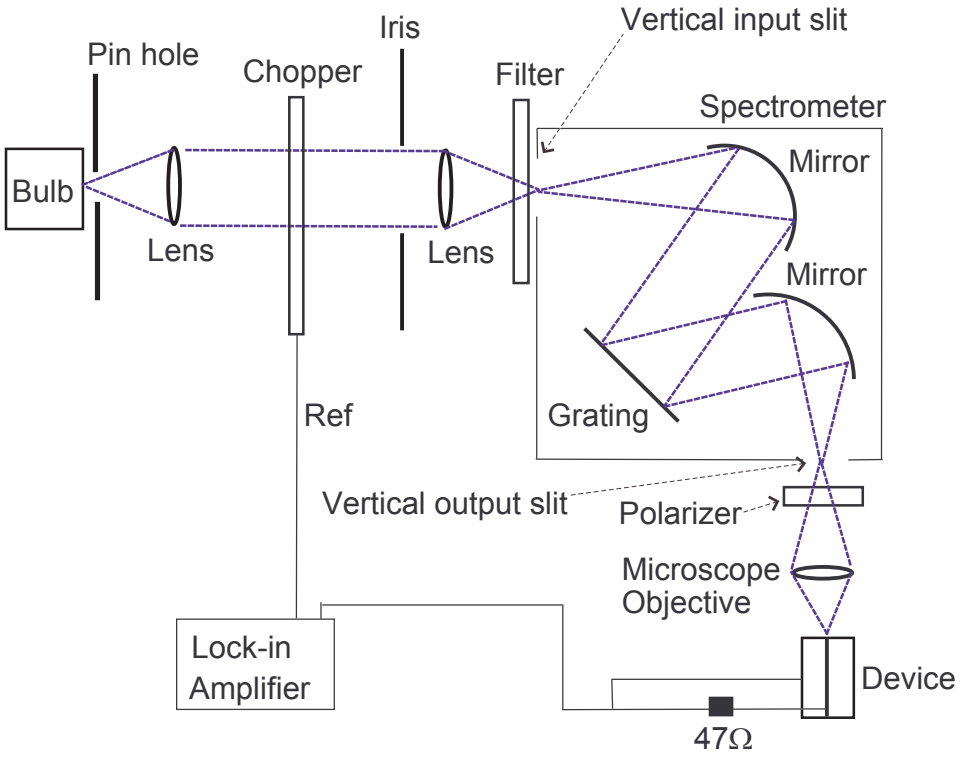

Figure 3.5: Schema of the set up used to measure polarized edge-photovoltage spectra at room temperature.

the light at a known frequency (typically 20 kHz), the E-PV can be detected using a lock-in amplifier.
A lock-in amplifier [54, 55] consists of a phase sensitive detector, which performs the AC to DC conversion of the input signal under investigation. Inside the lock-in amplifier the input signal is multiplied by a 50-50 duty cycle oscillator reference signal, which is generated with the same frequency as the AC input. The phase sensitive detector does not rectify the noise, which appears as an AC fluctuation on the DC output and is removed by a low pass filter so that the output of the lock-in amplifier is a DC voltage. In our case the model used is an EG&G 7260 DSP lock-in amplifier.

3.3.2 Experiment

The samples being investigated are buried heterostructures (BH) or ridge waveguides (RW) with an optical axis along the (110) direction. In this configuration, E-PV emission polarized along the (1-10) direction ($TE_{(1-10)}$), and TM-polarized E-PV spectra are measured. This will be revisited in more detail below. In order to carry out polarization dependent spectral measurements, the polarization dependence of the grating must be removed. In this thesis most of the $TE_{(1-10)}$ and TM-polarized E-PV spectra are measured in two configurations, with the heterostructure growth direction (001) aligned parallel and perpendicular to the spectrometer slits respectively. The coupling in both configurations has to be optimal in order to couple light into the same part of the waveguide. First the system response is removed from each spectrum. The four spectra are then used to remove the effects of the polarization dependence of the experimental set up, due to the grating in the spectrometer. Alternatively one can use a half-wave plate, as in chapter 7.

Spectral Corrections

In an optical system, most components have some wavelength dependence, leading to a system response which must be measured and removed as it affects the shape of the measured spectrum. The set up used to measure the system response of the polarized E-PV experiment is similar to that in Fig 3.5, except that the sample is replaced by the calibrated detector from an Ando AQ2140 powermeter. A system response spectrum is collected for the two polarizations and each E-PV spectrum is corrected by dividing out the system response. A second correction is then used to remove the polarization dependence of the spectrometer grating, following the method presented in Ref [53]. Errors in this collection and correction method are be due to misalignment, leading to photovoltage not being generated from the

same region of the junction, but are minimised by careful alignment.
The polarized E-PV spectra are referred to as having been collected with the (001) crystal axis parallel *(p)* or perpendicular *(h)* to the spectrometer slits. The measured polarized E-PV spectrum is denoted as $S_k(\lambda, i)$ if collected in an orientation k for a polarization i. In order to correct the spectra, two pairs of spectra collected with the (001) axis aligned p and h to the spectrometer slits need to be considered. The spectrally corrected polarization dependent spectra are labeled, $P(\lambda, p1)$ and $P(\lambda, p2)$, for polarizations $p1$ and $p2$ respectively. O_p and O_h give the orientation dependence of the spectrum collected in the p or h orientation. I_{IN} represents the magnitude of the incident photon flux on the sample in a photovoltage spectrum. The collection efficiencies, $R_p(\lambda)$ and $R_h(\lambda)$, are assumed to be the same for a pair of spectra in a particular orientation and represent the fraction of the light transmitted into the sample.
Spectra, $S_p(\lambda, p1)$ and $S_p(\lambda, p2)$, taken with the sample oriented parallel to the spectrometer slits for polarizations $p1$ and $p2$ are written as

$$S_p(\lambda, p1) \propto R_p(\lambda) P(\lambda, p1) O_p I_{IN} \tag{3.1}$$

$$S_p(\lambda, p2) \propto R_p(\lambda) P(\lambda, p2) O_p I_{IN} \tag{3.2}$$

For the sample oriented perpendicular to the spectrometer slits, the spectra are $S_h(\lambda, p1)$ and $S_h(\lambda, p2)$, noting that changing the sample orientation by 90° swaps the orthogonal polarizations. The ratio of a pair of spectra collected in the same orientation, for example parallel to the spectrometer slits, can be written as

$$\frac{S_p(\lambda, p1)}{S_p(\lambda, p2)} \propto \frac{P(\lambda, p1)}{P(\lambda, p2)} \tag{3.3}$$

Looking at equation (3.3), the spectrally corrected polarization dependent spectrum, $P(\lambda, p1)$ can be written as a function of $P(\lambda, p2)$, if the ratio of the two spectra collected parallel to the spectrometer slits is known. Taking the ratio of the measured spectra collected perpendicular to the spectrometer slits, $S_h(\lambda, p1)$ and $S_h(\lambda, p2)$ and coupling it with equation (3.3) enables us to write the ratio of the spectrally corrected polarization dependent spectra, $\frac{P(\lambda,p1)}{P(\lambda,p2)}$ as a function of the measured polarized spectra $S(\lambda, p1)$ and $S(\lambda, p2)$, collected parallel and perpendicular to the spectrometer slits, as shown in equation (3.4).

$$\frac{P(\lambda, p1)}{P(\lambda, p2)} \propto \sqrt{\frac{S_p(\lambda, p1)}{S_h(\lambda, p2)} \frac{S_h(\lambda, p1)}{S_p(\lambda, p2)}} \tag{3.4}$$

Therefore $P(\lambda, p1)$ can be written as a function of $P(\lambda, p2)$ and both spectra can be plotted on the same intensity axis, as the polarization dependence of the grating in the spectrometer has been removed.

Components of Polarized Spectra

Due to the direction of the electric field, polarized E-PV spectra generated by light incident on the facet of a device with its optical axis parallel to (110) cannot give any information about $TE_{(110)}$ polarized transitions, as seen schematically in Fig 3.6. In a quantum well, $TE_{(1-10)}$ and $TE_{(110)}$-polarized spectra are expected to be identical, due to rotational symmetry in the quantum well plane. This is not expected to be the case in quantum dash material due to the asymmetry of the dashes, which are elongated along the (1-10) direction.
In order to measure an E-PV spectrum for $TE_{(110)}$ and TM-polarizations, we attempted measurements where light was incident on the side of an oxide stripe laser, illustrated schematically as (b) in Fig 3.6. An oxide stripe quantum dash laser was cleaved along the gold contact to expose the active region, mounted and

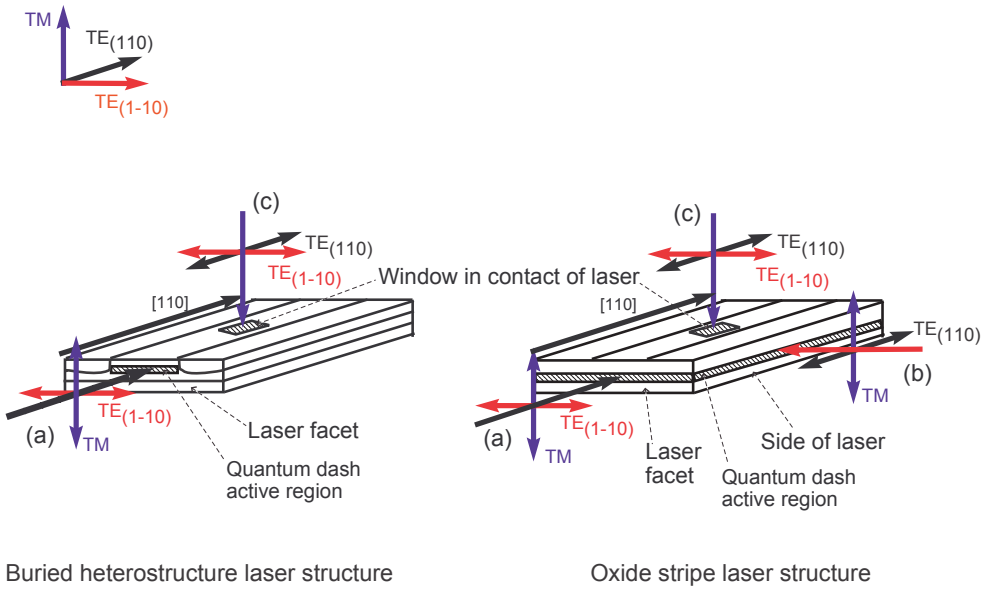

Figure 3.6: Schematic view of polarized photovoltage in a buried heterostructure and oxide stripe laser. Due to the direction of the electric field (indicated by a single headed arrow), (a) $TE_{(1-10)}$ and TM-polarized PV spectra are measured when light is incident on the facet of the laser. (b) $TE_{(110)}$ and TM-polarized PV spectra are measured when light is incident on the side of the oxide stripe laser. The active region is not accessible from the side of the BH laser. (c) When light is incident parallel to (001), $TE_{(1-10)}$ and $TE_{(110)}$ PV components can be measured. The directions of the electric fields are included in the top left corner respectively.

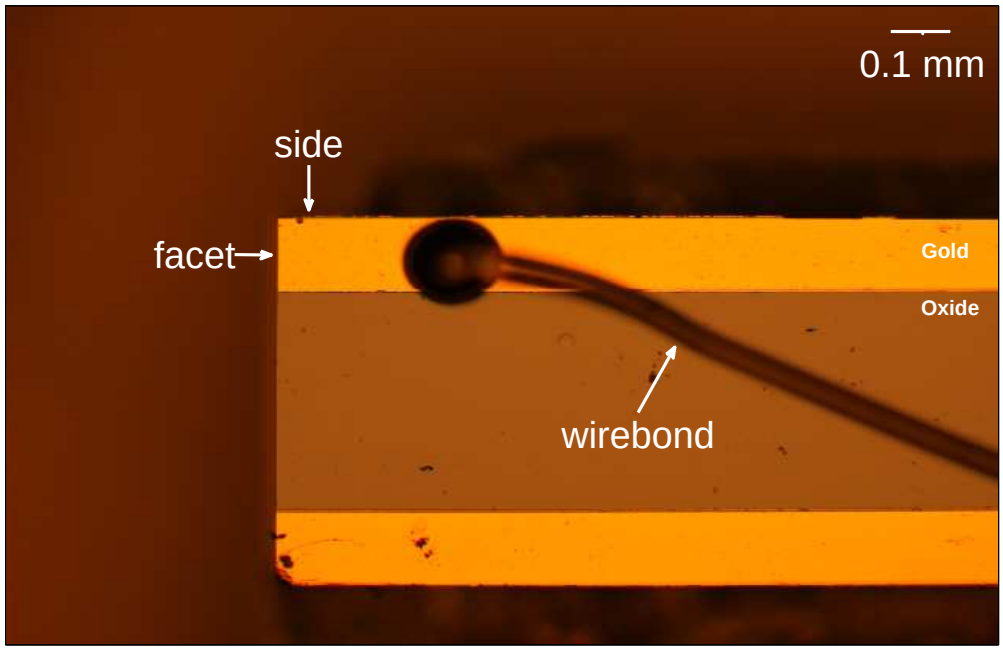

Figure 3.7: Photo of a quantum dash oxide stripe laser used to measure polarized PV spectra from the side and facet. The two yellow regions are the gold p-contacts of lasers. The orange region is oxide. The top laser is the test laser and has a wire bonded which can be seen in the photo.

wire bonded as shown in Fig 3.7. Polarized E-PV spectra were then measured at the side of the facet, close to the cleaved side, as well as along the side of the laser, close to the laser facet. This was to try to ensure that E-PV was generated from the same dash ensemble at the facet and at the side of the laser. The spectra collected at the facet and side were corrected as outlined in section 3.3.2. The intensity of the corrected TM-polarized PV spectra collected at the facet and side were normalised and plotted, as shown in Fig 3.8. However, the TM-polarized E-PV spectra measured at the side and at the facet were spectrally different, due presumably to stresses and resultant strain of the active region. Given the difference between the two TM-polarized spectra, which should be identical, we concluded that this was not an appropriate approach to compare the $TE_{(1-10)}$ and $TE_{(110)}$-polarized spectra.

Alternatively, we investigated whether $TE_{(1-10)}$ and $TE_{(110)}$-polarized PV could be measured directly by focusing light into the material in a direction parallel to (001), as shown schematically by (c) in Fig. 3.6. However, the quantum dash materials analysed in this thesis have very low optical absorption cross-section per dash and therefore a very low voltage was generated when light was coupled into a window milled in the p or n-contacts of the laser. Light from the tungsten bulb was coupled through the spectrometer and into a window in the p-contact

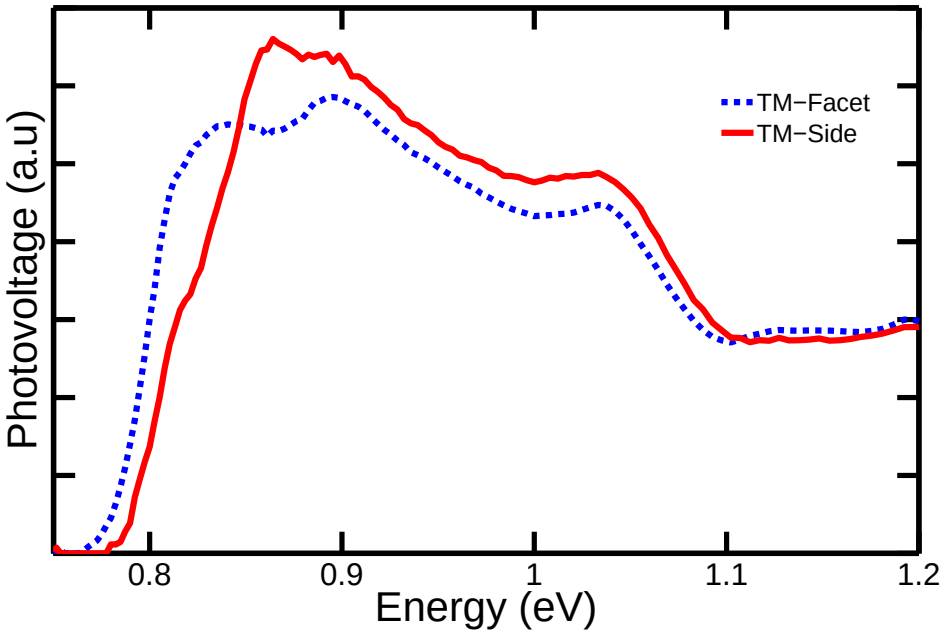

Figure 3.8: Corrected TM-polarized photovoltage spectra for an oxide stripe laser. The blue dash data was measured using light incident on the facet, and the red line was measured using light incident on the side of the laser.

of the laser, a very small voltage was measured and the signal to noise ratio was too low. A larger PV signal was measured by coupling fibre-coupled light from a tunable laser into a window milled in the n-contact of the laser. Test experiments were carried out using polarization-maintaining fibre but the output polarization of the tunable laser module was found not to be sufficiently stable. In view of this, the method chosen in this thesis to analyse both TE components involves free-space spontaneous emission (SE) spectral measurements, and will be presented in section 3.4.

In summary, this section included a description of the experimental set up used to carry out polarized E-PV spectroscopy. The methods used to correct the spectra by removing system response and the polarization dependence of the grating in the spectrometer were also outlined. Although the corrections are applied to E-PV spectra in section 3.3.2, they can be applied to any spectral measurement taken for two orthogonal polarizations, including the SE measurements presented in the next section.

3.4 Spontaneous Emission

Studying spontaneous emission is widely used in the characterisation of semiconductor lasers as it provides information about intrinsic material and device properties [42, 56, 57]. Some authors [58] refer to amplified spontaneous emission (ASE) measurements measured at the laser facet as spontaneous emission. The spontaneous emission (SE) measurements presented in this work involve unamplified, 'pure' SE measured in a direction perpendicular to the device waveguide.
SE spectra can be collected from the side of an oxide stripe laser, which has been cleaved along the gold contact to expose the active region. In a ridge waveguide laser, SE can be collected through the side of the laser without any special processing. SE can also be collected vertically through a window in the p- or n-side electrode of any laser or semiconductor optical amplifier structure. The window can be made during the processing [56, 59] or can be milled [39] as outlined in section 3.2. When measuring SE, the direction of collection governs which components can be measured in a similar way to that described for photovoltage in Fig. 3.6. Collecting SE through the side of an oxide stripe or ridge waveguide laser gives access to $TE_{(110)}$ and TM-polarized components. However, in order to simultaneously collect $TE_{(1-10)}$ and $TE_{(110)}$, SE is collected vertically through

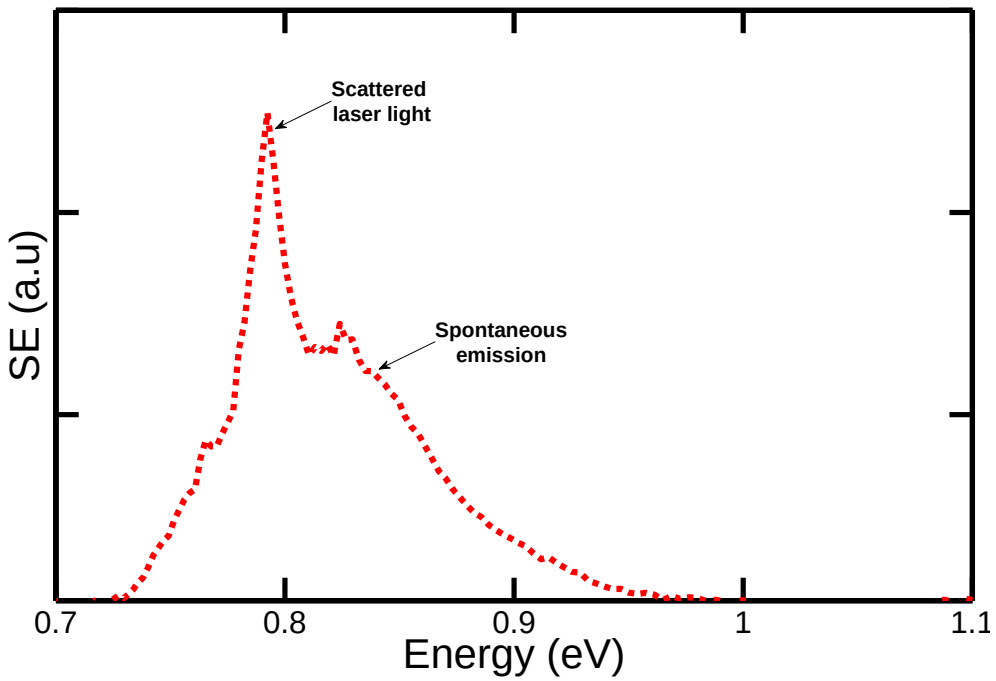

Figure 3.9: SE spectrum measured above threshold in free space for a test laser, showing the scattered laser peak.

windows milled in the p and n-contact of the devices.
SE can be collected using a microscope objective or an optical fibre and measured using a power meter, spectrometer and photodetector or optical spectrum analyser (OSA). Two set ups, seen schematically in Figs 3.10 and 3.14, were used in this work to collect SE. When SE spectra are collected from a window milled in a laser for currents greater than threshold, a scattered laser peak is observed, as seen in Fig. 3.9, where the narrow laser line has been broadened by the 10 nm spectrometer resolution. Therefore when SE spectra were polarized and measured as in section 3.5, the device was operated below the lasing threshold to avoid any scattered stimulated emission.

3.5 Spontaneous Emission Spectral Measurements

$TE_{(1-10)}$ and $TE_{(110)}$-polarized transitions in quantum dashes are not expected to be of equal magnitude. However, due to the low cross dash absorption, measuring polarized E-PV spectra along (001) was not experimentally possible. By applying a bias to the test device and measuring the polarized SE spectra, information can be obtained about the in-plane anisotropy of the optical properties in quantum dashes. The set up used is described in section 3.5.1 and tested on a multiple quantum well (MQW) device in section 3.5.2. Finally the set up and the method used to measure wide range unpolarized SE spectra is presented in section 3.5.2.

3.5.1 Set Up

Polarized SE spectra are collected using a free-space set up at room temperature. The device is mounted n-side down on a carrier and wire-bonded. The laser light-current-voltage (LIV) characteristics are measured from the facet before a window (6μm x 10μm, and $\sim 1\mu$m deep) is milled on the p-side. The facet LIV characteristics are measured again after milling to ensure no damage has occurred due to the FIB. The window is then inspected under a microscope and the window emission is observed using an IR camera, as outlined in section 3.2. The carrier is mounted perpendicular to the optical bench on a piezoelectric xyz-stage. The SE set up can be seen schematically in Fig 3.10. An Agilent 81101A Pulse Generator (pulser) is used to drive the laser with a 50% duty cycle. The amplitude of the bias current is measured using a current probe, inside which the voltage from the pulser induces a current in a coil, which can be measured on an oscilloscope, via a 50 Ω resistor or on a lock-in amplifier. The frequency of the pulser is chosen to match the detector and current probe frequency specifications. A microscope objective (x 40) with a large NA and small focal length is used to selectively collect window emission. A

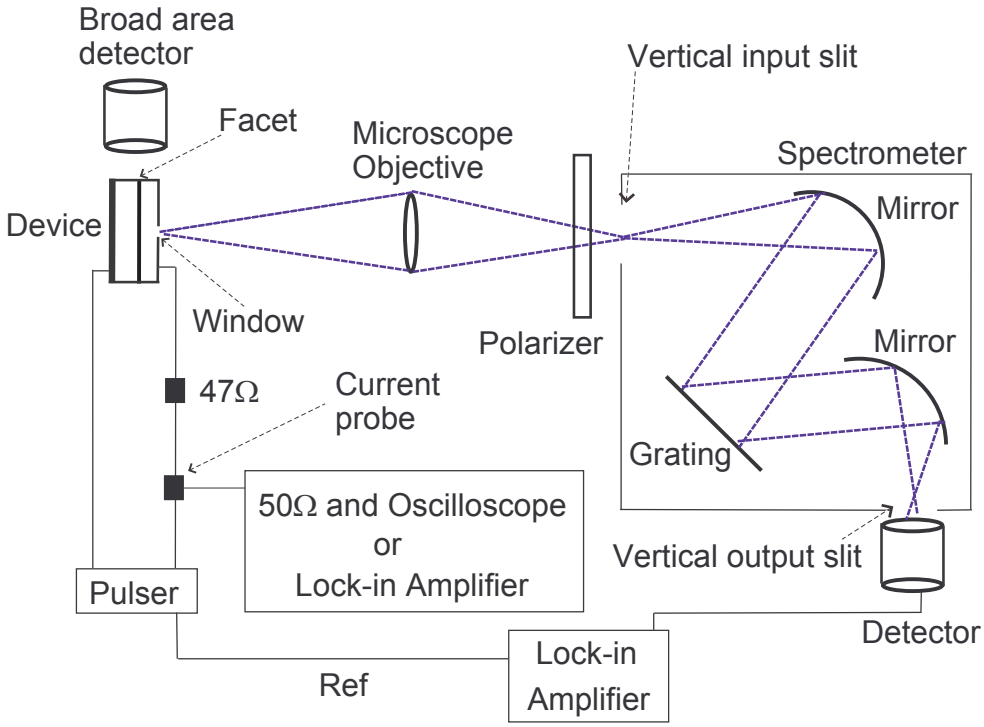

Figure 3.10: Schema of the set up used to measure polarized spontaneous emission spectra at room temperature.

polarizer is used to discriminate between $TE_{(1-10)}$ and $TE_{(110)}$-polarized SE. The polarized SE is then coupled through the spectrometer and onto a photodetector. The BNC output of the detector is connected to a lock-in amplifier, to measure the optical power incident on the detector. In this set up the facet emission from the device can also be collected using a broad area detector.

3.5.2 Experiment

As outlined in section 3.3.2 any polarized spectrum collected in free space using a spectrometer has to be corrected to remove the polarization dependence of the spectrometer grating, as well as the system response. First $TE_{(1-10)}$ and $TE_{(110)}$-polarized SE spectra are collected through a window as a function of current in the parallel configuration. The measurement is then repeated once the window had been coupled up for the device in the perpendicular configuration. The spectra are then corrected to remove the system response and the polarization dependence of the grating, using the method outlined in section 3.3.2. The $TE_{(1-10)}$ and $TE_{(110)}$ SE spectra can then be plotted on the same scale and their magnitudes compared. In order to confirm that the polarization dependence of the measurement set up has been correctly accounted for, $TE_{(1-10)}$ and $TE_{(110)}$ polarized SE spectra were

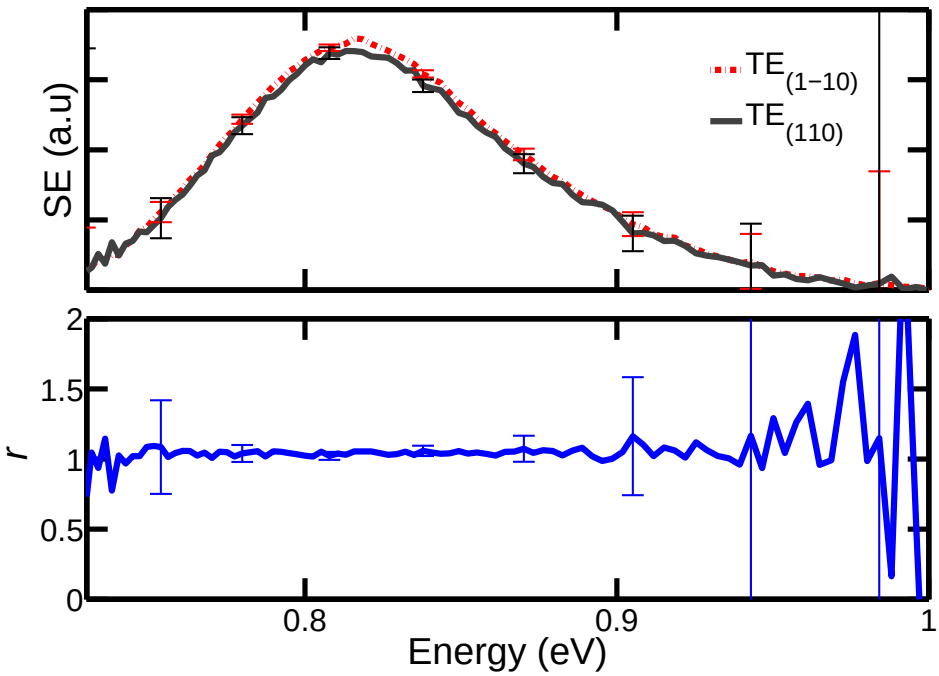

Figure 3.11: Top panel: Polarized SE spectra where $TE_{(1-10)}$ spectrum is plotted as red dash dot and $TE_{(110)}$ as black line. Bottom panel: ratio $r = TE_{(1-10)}/TE_{(110)}$ for a MQW device.

measured for a MQW test device. The sample was mounted with the (110) crystal axis parallel and then perpendicular to the spectrometer slits and spectra were measured at 50 mA. The spectrally corrected polarized SE spectra are shown in the top panel of Fig. 3.11. As expected both TE components are equal within experimental error. Plotting the ratio $r = TE_{(1-10)}/TE_{(110)}$ in the bottom panel of Fig. 3.11, it can be seen that there is no energy dependence of r in the MQW sample. This is to be expected, because the two polarization directions are equivalent in a quantum well structure [32]. Fig. 3.11 therefore confirms that the calibration of the polarized SE set up for the measurements undertaken on quantum dashes in chapters 4 and 6.

Wide Spectral Range Unpolarized SE Measurement

In order to measure whether any SE is emitted from the barrier regions we measure unpolarized spontaneous emission spectra as a function of current over a wide spectral range (1000 – 2000 nm) using a similar set up to that shown in Fig 3.10. A high pass filter with 1300 nm cut of frequency is used when measuring the spontaneous emission from the barrier to ensure that no scattered light or higher order contributions from the spectrometer grating are mistakenly measured. The

wide range spectra are only corrected to remove the system response
To summarise, this section includes an overview of the set up used to measure polarized and unpolarized SE spectra. The polarized SE spectra are corrected as in section 3.3.2. The set up is tested on a MQW device in section 3.5.2 where as expected the magnitude of both polarizations is the same.

3.6 Temperature-Dependent Facet and Spontaneous Emission Measurements

As part of the laser characteristion and analysis, we measure how the integrated SE varies as a function of drive current and temperature, from 40 – 330 K. We also make facet measurements over the same temperature range to determine the temperature dependence of the threshold current and of the external differential quantum efficiency.
A closed cycle helium cryostat is used to carry out these temperature-dependent facet and spontaneous measurements. The lasers used in this part of this work are bare chips. The LIV characteristics are measured before a window is milled on the n-substrate, and are again measured after windowing to confirm the lasers have not been damaged during milling. The cryostat set up and the experiment used in this part of the work are explained in detail in the following sections.

3.6.1 Set Up

This section includes a description of the closed cycle helium cryostat used in this work, as well as the laser mount on which the samples are tested.

The Closed Cycle Cryostat

A schematic view of a closed cycle helium cryostat can be seen in Fig 3.12. In a cryostat system there are two independent systems, the vacuum cycle and the helium cycle. The vacuum cycle is made up of a rotary and turbo pump combination allowing the system to reach pressures of $\sim 10^{-6}$ mBar. The helium cycle used in this work is made up of a Leybold Coolpak 6200 compressor, which includes a water cooling system, a cold head, Fl4.5 flexlines and a model 9700 temperature controller [60]. The temperature stability of the cryostat system was +/- 0.01 K due to the wide temperature range. The compressor cools the helium gas, which leaves the compressor unit under high pressure. The gas travels through a flexline to the cold head. On reaching the cold head the gas expands and as it does so, it cools the cold head and sample chamber. The low pressure helium gas is then

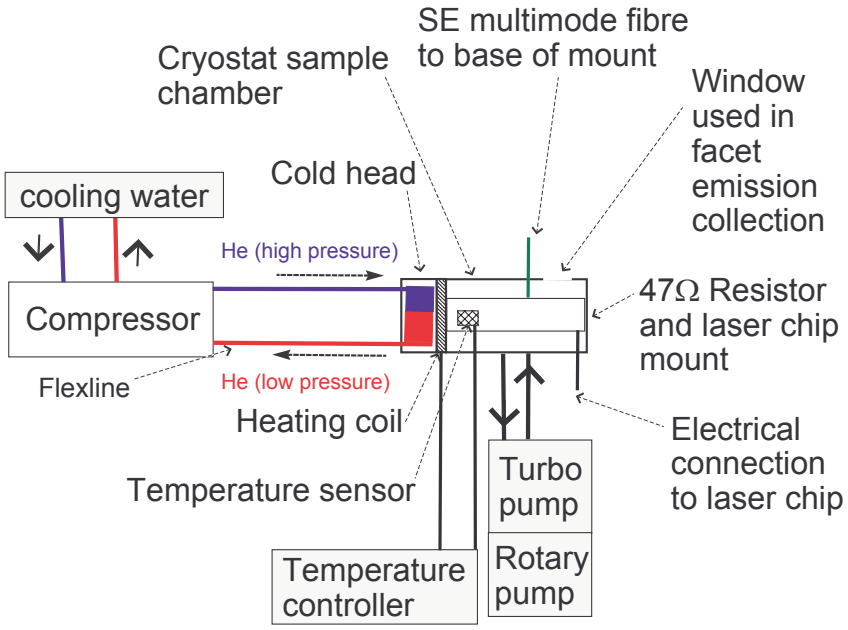

Figure 3.12: Schematic view of the close cycle helium cryostat used in this work.

returned to the compressor via a flexline. The heat generated in compressing the helium is removed from the system by a water-cooled heat exchanger in the compressor. A cryostat system can only cool. The temperature in the sample chamber can be varied from 6 – 330 K using an external temperature controller unit which works by changing the current passing though a heating coil mounted in the sample chamber. The temperature controller unit measures the temperature of the sample chamber by using a temperature sensor which is screwed into the laser chip mount. For a set current, the unit measures the voltage across a calibrated Si diode and the temperature is displayed on the front of the temperature controller unit. In the sample chamber a 47 Ω resistor is also included in series with the laser diode being tested on the laser chip mount.

The Laser Chip Mount

The laser chip mount, seen schematically in Fig 3.12 and 3.13, enables the collection of SE through the substrate with a constant collection efficiency and provides an electrical connection to the bare chip laser. The base is made of brass and can be mounted in the sample chamber, next to the heating coil. The 47 Ω resistor, bush and contact probe are all mounted onto the base. The bush is a 1 cm long brass cylinder with a 150 μm diameter hole drilled in the centre of one end. A 900 μm diameter counter-bored hole is drilled half way through the bush at the centre of the other end. A multimode fibre has been glued in the bush with the

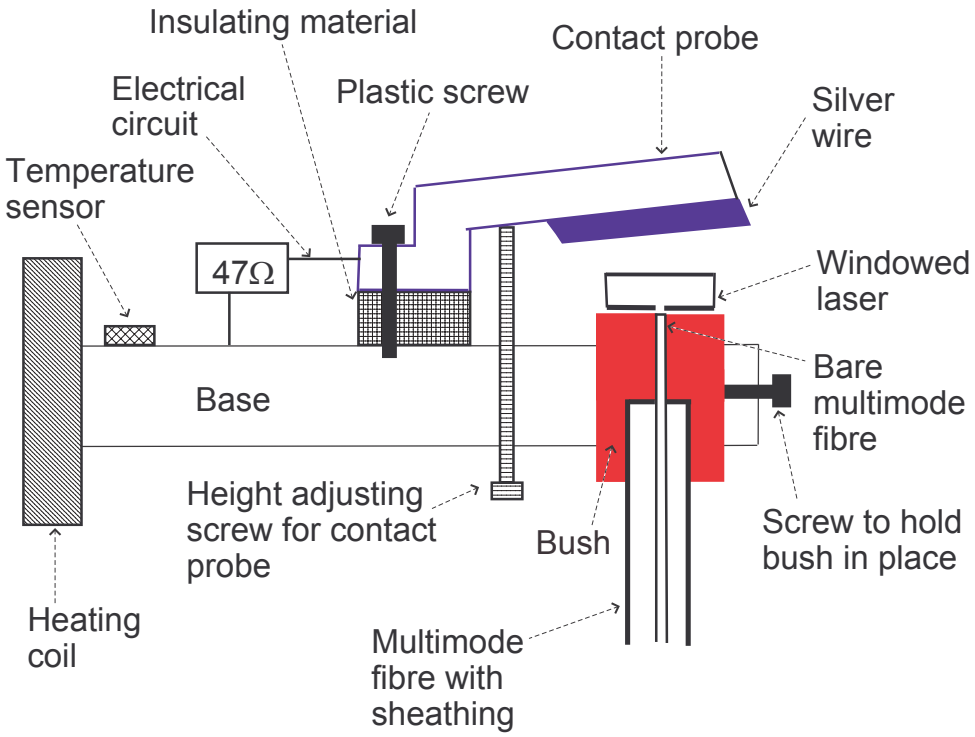

Figure 3.13: Schema of the laser chip mount and heating coil in the cryostat sample chamber.

150 μm diameter hole holding the bare multimode optical fibre flush with the end of the bush while the counter-bored hole holds the fibre sheathing in place. The bush is fitted into the base and held in place with a screw. Electrical connection to the n-contact of the laser is made through the bush and base. A copper contact probe and a piece of insulating material are mounted into the base using a plastic screw, as seen schematically in Fig 3.13. The p-contact with the laser is made through a silver wire mounted onto the end of the probe. The contact probe was designed and tested to ensure that it holds the laser chip in place, without any movements, during a thermal cycle, ensuring the SE collection efficiency is kept constant throughout the measurement. In order to change the laser sample, the height of the contact probe can be changed by moving a screw in the base.

3.6.2 Experiment

The coupling of both the spontaneous emission and facet emission must remain constant throughout the measurement from 40 – 330 K. A schematic view of the set up used to carry out the temperature-dependent measurements can be seen in Fig 3.14. The laser chip is placed at the centre of the bush and electrical contact is only made with the laser being tested. SE is collected from the test device

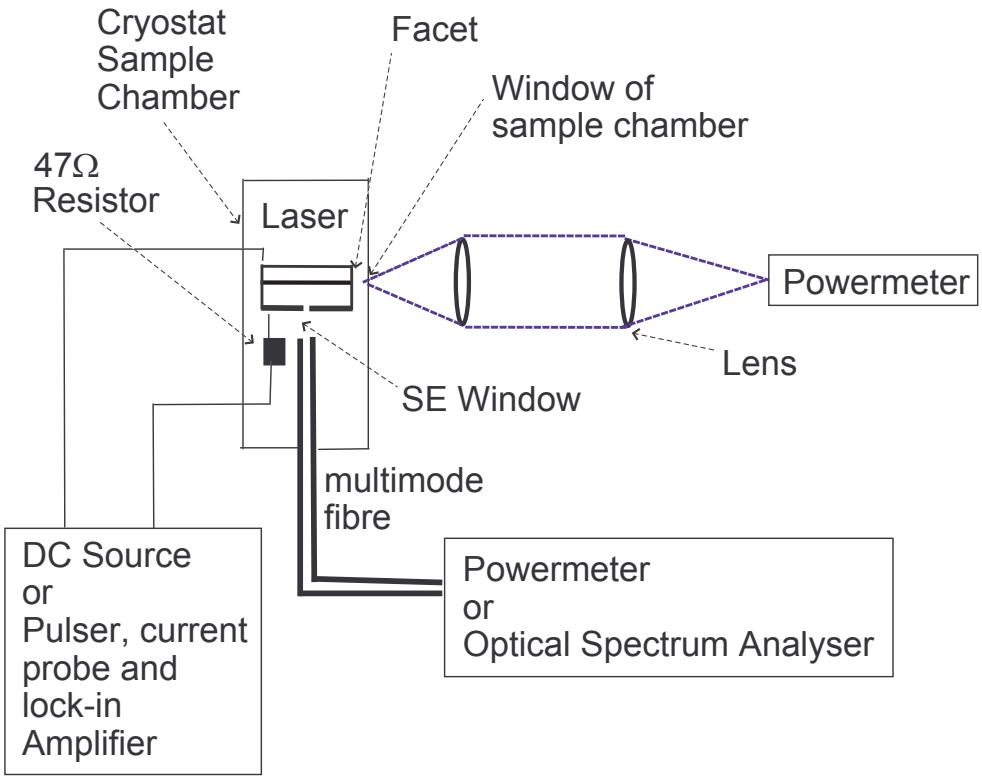

Figure 3.14: Schema of the set up used to measure the facet and spontaneous emission in the cryostat.

using a multimode fibre. The SE spectra are measured on an optical spectrum analyser (OSA). Measuring a SE spectrum can only be carried out for a small number of currents at each temperature, implying large current steps between the different measurements. The measurement can also be carried out for smaller current steps, with the integrated spontaneous emission power measured on the fibre coupled channel of an Ando AQ2140 powermeter. Outside the cryostat window a pair of lenses are used to collimate the facet emission and focus it onto the broad area photodiode channel of an Ando AQ2140 powermeter. Stray light, which may be collected by the broad area photodiode, must be blocked out for the duration of the experiment.

The current is either DC or pulsed, depending on the sample. Lasers with low threshold currents are measured using a 2400 Keithley DC source. For devices with larger threshold currents, an Agilent model 81101A pulser is used to drive the laser with a 2% duty cycle (1μs pulses at 20 kHz) and the current is measured using a current probe and a lock-in amplifier.

The total threshold current, I^{th}_{total}, is found by measuring the current for the onset of lasing from the facet. The radiative component of I^{th}_{total}, I^{th}_{rad}, is extracted from

the integrated SE. The error in this experiment relates to accurately measuring threshold, especially at low temperatures.
In summary, this section contains an overview of the set up used to measure facet and spontaneous emission as a function of current and temperature. Measurements are taken from 40 – 330 K, with the set up designed to ensure that the coupling efficiency of both optical measurements remains constant throughout the measurement.

3.7 Summary

In summary this chapter provides an overview of the main experimental methods used in this work. Firstly an outline of the window milling process is given in section 3.2. Next a description of the set up and experimental procedure used to measure room temperature polarized edge-photovoltage is given in section 3.3. Spontaneous emission is presented in section 3.4 and the experimental method used to measure room temperature polarized spontaneous emission spectra is given in section 3.5. Lastly the set up and experimental method used to collect facet and spontaneous emission as a function of temperature is described in section 3.6.

Chapter 4

Analysis of InAs/InGaAsP/InP Quantum Dash Lasers

4.1 Introduction

Semiconductor lasers with quantum dot or wire active regions have long been proposed for future optoelectronic laser devices, with potential benefits including low and temperature insensitive threshold current, zero linewidth enhancement factor, and reduced chirp [4, 61]. Despite the advances in this technology only some of these benefits have been achieved. To date, much of the effort in developing quantum dot lasers has been based on the development of GaAs devices emitting around 1.3 μm [5, 62]. However, as with quantum well devices, there remains difficulty in extending GaAs-based devices to the second telecommunications window at 1.55 μm, and InP remains the most suitable substrate choice for this spectral region.

Growth of quantum dots on the commercially favoured (100) orientated InP substrate can result in quantum dots elongated along the (1-10) axis, called *quantum dashes*. InAs/InGaAsP/InP quantum dash lasers have been demonstrated to have many impressive characteristics such as high modal gain per layer and high characteristic temperature [7]. In addition to these figures of merit, these dash lasers have been shown to have a greater insensitivity to optical feedback than quantum well structures [63], and they can also be used for mode-locking without an active or passive saturable absorber [64]. In addition the use of quantum dashes may also enable polarization stable vertical cavity surface emitting lasers [65]. Nevertheless, there has to date been little detailed analysis reported of the consequences of dash formation on the electronic structure and intrinsic device characteristics.

This chapter includes an experimental analysis of InAs/InGaAsP/InP quantum dash-in-a-well (DWELL) and dash-in-a-barrier (DBAR) devices. Details of the

materials and devices studied are given in section 4.2. An overview of the theoretical analysis carried out by Dr. Sorcha Healy, which is relevant to the interpretation of experimental results, is presented in section 4.3. Results indicate that the low electron mass and small conduction band offset lead to electrons not being confined in the dash in the case of a DWELL structure and are only weakly confined in the dash in a DBAR structure. By contrast, the heavy hole states see a large band offset. The combination of strain and dash shape lead to the optical matrix elements being strongly enhanced for light polarized parallel to the dash long axis, and hence to an anisotropy in the TE-polarized gain and spontaneous emission in the growth plane. The strain also leads to strongly reduced TM-polarized emission at the band edge, as is also found in compressively strained quantum well lasers [53]. It is also observed that the electron and hole calculated integrated density of states are quantitatively very similar within an energy range of $\sim$ 50 meV of the band edge.

The first part of the experimental analysis presented in sections 4.4.1 and 4.4.2, confirms the presence of the anisotropy in the optical characteristics. First polarized edge-photovoltage (E-PV) spectroscopy is used to confirm the suppression of TM-polarized recombination at the band edge. Then polarized spontaneous emission (SE) measurements are taken through a window in the top laser contact to confirm the anisotropy in the growth plane. The second part of the experimental work included in section 4.4.3 involves studying the recombination processes present in quantum dash lasers by comparing the measured dependence of the integrated SE rate to the total current as a function of temperature. Experimental results show that the temperature performance of these 1.55 μm InP-based devices remains limited by Auger recombination, as was previously shown for 1.55 μm quantum well lasers [39]. The analysis also shows a correlation in one device between the onset of current leakage paths and a reduction in the external differential quantum efficiency. In the absence of current leakage paths the external differential quantum efficiency is limited by optical losses. The issue of carrier transport effects in the dashes is also addressed. GaAs-based quantum dot lasers emitting at 1.3 μm typically show strong evidence of poor carrier transport at low temperatures, resulting in the threshold current typically increasing with decreasing temperature for T $\leq$ 200 K [66, 67]. This anomalous variation in threshold current is much weaker in the devices studied here, suggesting that the weak electron localization and quantum wire-like valence band density of states allows a more rapid thermalisation of carriers in quantum dash lasers compared to 1.3 μm quantum dot devices. A summary of the work presented in this chapter is included in section 4.5.

4.2 Materials and Devices

This section includes an outline of the materials and devices studied in this chapter. The material was grown at Alcatel – Thales III – V Lab by gas source molecular beam epitaxy on the commercially favoured (100) InP-substrate orientation [7, 68] and is made up of six stacks of dashes. The first two sets of devices studied, DW1 and DW2, have a DWELL design, where the dashes are embedded in a 6 nm InGaAsP quantum well, which is lattice-matched to an InGaAsP barrier. The schematic flat band profile for the DWELL design can be seen in Fig. 4.1. The barrier and separate confinement heterostructure (SCH) layers are 40 nm and 80 nm thick in DW1. These layers are narrower in DW2, with values of 30 nm and 40 nm respectively. DW2 also has an increased level of p-doping in the upper p-cladding layer. The other two sets of devices studied, DB1 and DB2, have a DBAR structure where the dashes are now embedded in the InGaAsP barrier layer. The flat band profile for the DBAR design can also be seen schematically in Fig. 4.1. The p-doping levels in the cladding and the width of the barrier and SCH layers are as in DW1.

The typical dash height is $\sim$ 2 nm. The dashes in DW1, DW2 and DB1 are elongated with the long axis of the dashes orientated along (1-10) and the shorter axis along (110). The dashes have approximate in-plane dimensions of 20 nm x 200 nm along (110) and (1-10) respectively. In DB2, the dashes are more dot-like with in-plane dimensions of $\sim$ 20 nm along (110) and $\sim$ 40 nm along (1-10) due to different growth conditions.

The materials were processed as buried ridge stripe lasers or semiconductor optical amplifiers (SOA) at Alcatel-Thales III-V Lab. All lasers have an optical axis along the (110) crystal axis and as-cleaved facets. The SOA samples are 2 mm long with an angled cavity at 7° to the (110) crystal axis and have antireflection coated facets. The SOAs are used in this chapter only for material property measurements.

The devices studied in sections 4.4.1 and 4.4.2 are mounted and wire bonded. In section 4.4.1 all samples are 600μm long lasers which have a ridge width of 1.5μm. The DW1 and DB1 samples in section 4.4.2 are lasers with a ridge width of 1μm and length 300μm and 320μm respectively. The DW2 sample is a 600μm long laser with a ridge width of 1.5μm, while the DB2 sample is an SOA. This difference in samples in these two sections does not affect the results as material properties are being investigated. In section 4.4.3 temperature-dependent measurements are carried out on bare laser chips which are 600μm long and have a ridge width of 1.5μm.

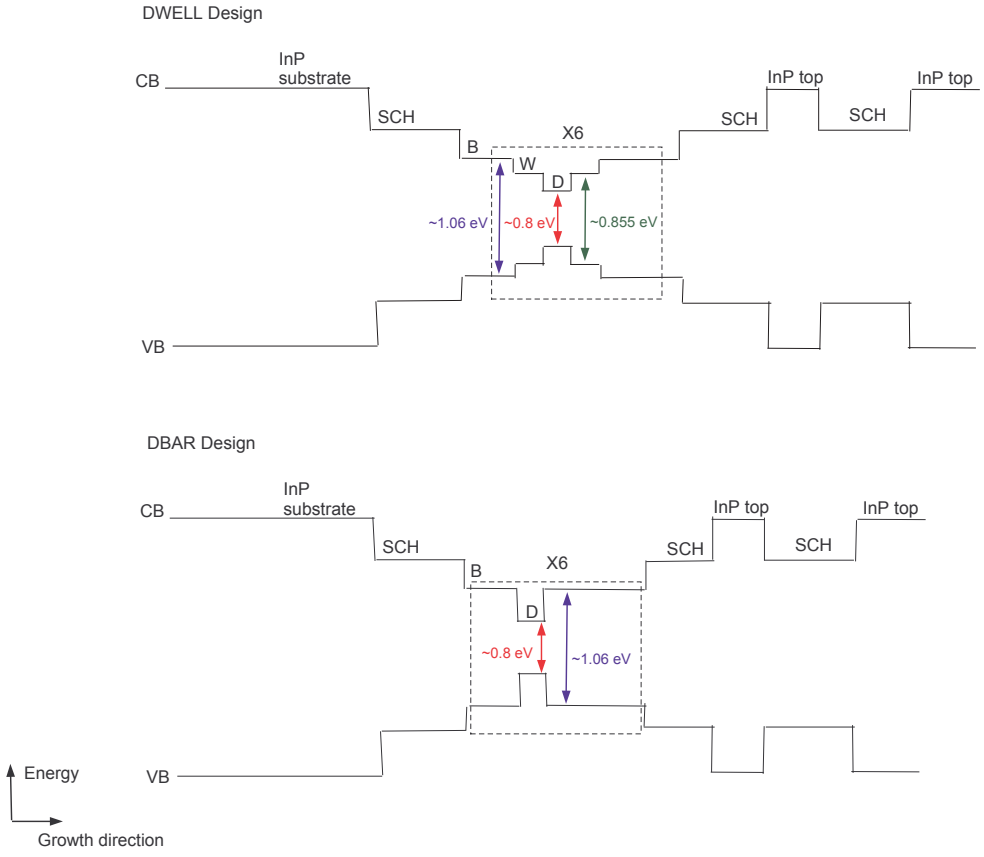

Figure 4.1: Flat band schema of the conduction and valence band profile of the DWELL (top) and DBAR (bottom) design with 6 stacks of dashes. The energy of the dash (D), well (W) and barrier (B) transitions are included for the DWELL while the dash (D) and barrier (B) transition energies are marked for the DBAR.

4.3 Theoretical Modeling

This section includes a summary of the relevant theoretical results of calculations carried out by Dr. Sorcha Healy. These will be compared to experimental results in sections 4.4.1 and 4.4.2.

4.3.1 Overview of Theoretical Analysis

The band offsets are calculated using material parameters in Ref [69], with the effects of strain incorporated following the method in Refs [70, 71]. The energy states and wavefunctions of the lowest confined conduction and valence band state are calculated by solving Schrödinger's equation for an 8-band k.p envelope function Hamiltonian using the plane wave expansion technique [71].
Calculations are performed for two types of materials. The first material is a DWELL design similar to DW1 with a 1.3 nm (001) x 15 nm (110) x 80 nm (1-10)

InAs dash embedded in a 6 nm lattice-matched InGaAsP quantum well (~ 0.855 eV material absorption edge) in a lattice matched InGaAsP barrier (~ 1.06 eV). In the second material, which is a DBAR design, the InAs dashes have the same in-plane dimensions as the DWELL but are 1.9 nm tall (along (001)). The InAs dashes are confined by a bulk barrier with ~ 1.06 eV absorption edge. In both materials the theoretical dash height has been chosen to give an optical gap of 0.8 eV (1.55 μm).

In order to ensure convergence of the ground state and lowest excited state energies in the DWELL and DBAR materials the dimension of the long dash axis along (1-10) is reduced to 80 nm from the experimentally measured value of ~ 200 nm. The difference in the dash length along the long axis has a negligible effect provided the in-plane areal coverage of dashes is constant. The experimentally measured surface density of dashes ranges between $1 - 4 \times 10^{10}$ cm^{-2} [7]. The dashes were measured using cross-section transmission electron microscopy (TEM) to have a lens-shaped cross-section [7]. However previous calculations on InAs/InGaAlAs dashes [72] have shown that it is reasonable to approximate a dash with lens-shaped cross-section by a dash with rectangular cross-section. The net strain over the supercell is constrained to be zero. Using supercells with dimensions of 16 nm along (001), 50 nm along (110) and 100 nm along (1-10), gives a filling factor of 0.24 and a dash density of 2×10^{10} cm^{-2}. The energy states and wavefunctions are calculated using a basis of 11, 17 and 17 plane waves along the (110), (1-10) and (001) directions respectively. The ground state electron and hole states are then converged to within a few meV. The convergence of the higher energy states will tend to decrease with increasing energy separation from the band edges, but this does not affect any of the analysis or conclusions of this work. Lastly, TEM measurements [7] show the dashes sitting on a thin wetting layer (WL). However because of the small CB offset, the WL CB states only slightly perturb the continuum of quantum well and barrier conduction states. The deep VB well ensures that the WL states are well separated from the dash valence states. Hence we conclude that for this discussion it is reasonable to ignore the WL states when modeling InAs/InGaAsP/InP quantum dashes.

4.3.2 Overview of Theoretical Results

The insets in Fig. 4.2 show the calculated band profile and lowest confined state energies for the DWELL and DBAR material. Due to the low InAs electron mass and small InAs/InGaAsP conduction band offsets, the electron states are poorly confined in both materials. In the DWELL, the electron ground state is not confined in the InAs quantum dashes, but rather in the surrounding quantum well

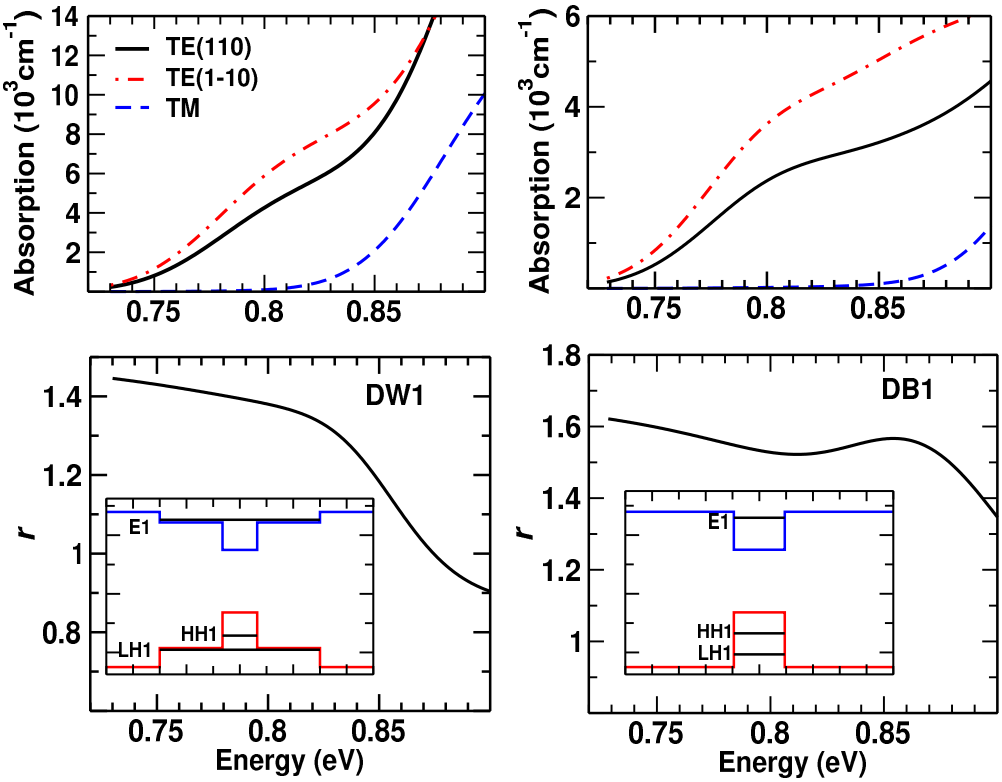

Figure 4.2: Calculated absorption curves (top) multiplied by filling factor ζ of DWELL (left) and DBAR (right). Also shown (bottom) are the corresponding anisotropy ratios, r=$|M^{(1-10)}|^2/|M^{(110)}|^2$ for the DWELL (left) and DBAR (right). Insets show the calculated band profile and lowest confined state energies for the DWELL (left) and DBAR (right).

layer. The lowest lying heavy-hole (HH) valence band states, HH1, are however well confined within the quantum dash in both materials due to the combination of hydrostatic and axial strain in the dashes. Results predict that the lowest lying light-hole (LH) states, LH1, are shifted downwards considerably in both the DWELL and DBAR because of the large axial strain component. We will investigate the predicted valence band dispersion in both samples in section 4.4.1 by measuring the polarization of transitions at the band edge using polarized E-PV spectroscopy.

The calculated electronic structure is used to determine the momentum matrix elements, describing transitions between all electron and hole levels within 120 meV of the ground state [73] at room temperature, and so to calculate the absorption at room temperature. The expression for absorption follows from the gain expressions in Refs [72, 74] and [5], modified by the inclusion of the dash filling factor ζ in

order to take account of the dash area density.

$$\alpha(p, h\nu) = \frac{\pi e^2 \zeta}{m_0^2 \epsilon_0 c n_r \omega} \frac{1}{V} \sum_i^{n_c} \sum_j^{n_v} |M_{ij}^p|^2 G\left(E_{c,i} - E_{v,j} - h\nu\right) \tag{4.1}$$

where p indicates the polarization direction, ζ is dash filling factor takes account of the dash area density, V is the volume of the quantum dash, $|M_{ij}^p|$ is the momentum matrix element in each of the relevant directions ($TE_{(110)}$, $TE_{(1-10)}$ and TM) for the ij^{th} transitions with energy separation $E_{c,i} - E_{v,j}$, $h\nu$ is the photon energy, and $G(x)$ is the Gaussian broadening function. n_c indicates the number of conduction band states while n_v indicates the number of VB states. The Gaussian broadening function is included to account for the presence of inhomogeneous broadening in a real quantum dash ensemble.

The calculated absorption spectra shown in the top row of Fig. 4.2 have a broadening of 30 meV, as measured experimentally in section 4.4.1. Calculations indicate that absorption polarized along the dash long axis is larger than along the other in-plane direction in both the DWELL and the DBAR. The bottom row of Fig. 4.2 shows the ratio between the two calculated in-plane absorption values, $\frac{\mathrm{TE}_{(1-10)}}{\mathrm{TE}_{(110)}}$. The causes of the enhancement of $TE_{(1-10)}$-polarized transitions over $TE_{(110)}$-polarized transitions will be discussed in more detail in section 4.4.2.

In summary, due to the effect of carrier confinement, strain and dash shape, an anisotropy of the optical properties is predicted in both DWELL and DBAR material, as seen in Fig. 4.2.

4.4 Experimental Analysis

Having reviewed the relevant theoretical results, we present in this section an experimental analysis of quantum dash materials and lasers. Polarized edge-photovoltage (E-PV) and spontaneous emission (SE) spectra are presented in sections 4.4.1 and 4.4.2, to evaluate the anisotropy of the optical properties of the quantum dash material. An understanding of the features of the polarized spectra and the causes of the anisotropy is gained by using the results presented in section 4.3. Having established the optical characteristics of InAs/InGaAsP/InP quantum dash materials experimentally, quantum dash lasers are then studied as a function of current and temperature in section 4.4.3. In this analysis the temperature dependence of the threshold current and its radiative component are measured and analysed in order to identify the dominant carrier recombination processes and losses, and their temperature dependence.

4.4.1 Polarized Edge-Photovoltage Spectroscopy

Polarized E-PV spectroscopy is used to determine the energy distribution and character of transitions between electrons and HH and LH valence band states [50, 52]. Typically TM-polarized spectra are due predominantly to transitions involving LH states, as outlined in chapter 2.

In this experiment, light from a broadband tungsten light source is spectrally resolved using a spectrometer, polarized and focused onto the laser facet. The generated voltage is measured using a lock-in amplifier. The measured polarized E-PV spectra are corrected for spectral variations, allowing the two orthogonal polarizations to be plotted on the same intensity scale [53], as outlined in chapter 3. In the quantum dash samples studied in this chapter, E-PV spectroscopy can only give information about $TE_{(1-10)}$ and TM-polarized transitions. Transitions involving $TE_{(110)}$ are hidden because the laser cavity is parallel to the (110) crystal plane and access to this polarization direction from the side of a buried heterostructure (BH) laser is not possible, as illustrated schematically in Fig. 4.3. Further information about the experimental set up used to measure polarized E-PV spectra was presented in chapter 3.

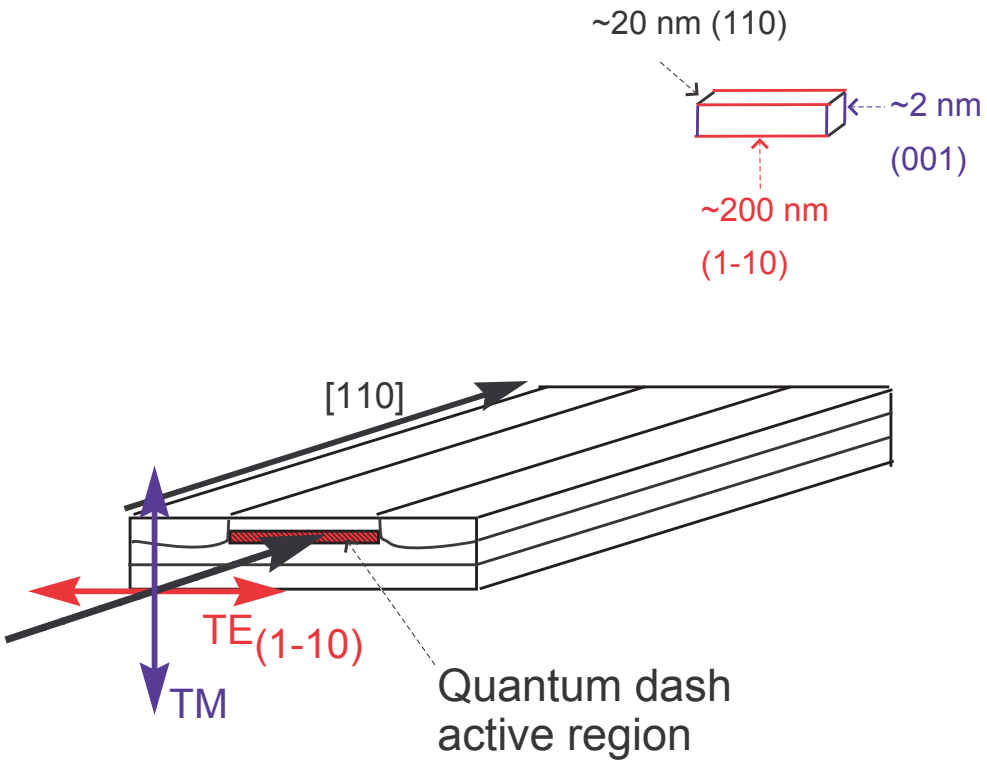

Figure 4.3: Schema of experimental configuration for E-PV measurement with polarized light is incident on the laser facet. The dash orientation is shown in the top right.

Spectra

Fig. 4.4 shows the polarized E-PV spectra collected for four samples where the $TE_{(1-10)}$ and TM-polarized spectra are shown by the red dash-dot and blue dashed lines respectively. A large difference between the $TE_{(1-10)}$ and TM-polarized absorption edges can be seen in all four panels of Fig. 4.4. This result is due to the strain-induced splitting between HH and LH valence band states, and is in good agreement with the theoretical results summarised in section 4.3. Based on the modeling in section 4.3 the features of the E-PV spectra are interpreted as originating from the dash states and the surrounding InGaAsP alloys, as indicated by the labels in Fig. 4.4. Considering first the top row of Fig. 4.4 the lowest energy transition ($\sim$ 0.8 eV) in DW1 and DB1 is attributed to recombination between HH ground state in the dash and ground state electrons. Several further peaks are clearly visible in these two spectra. The peak just below 0.9 eV in DW1 is associated with transitions between quantum well states. A clear shoulder close to 0.9 eV is found in the $TE_{(1-10)}$-polarized spectrum for DB1, close to the main peak in the TM-polarized spectrum. This feature is attributed to recombination between bound electron states and higher states with predominantly LH character. The InGaAsP barrier material is seen at $h\nu$ $\approx$1.1 eV in DW1 and DB1. Considering

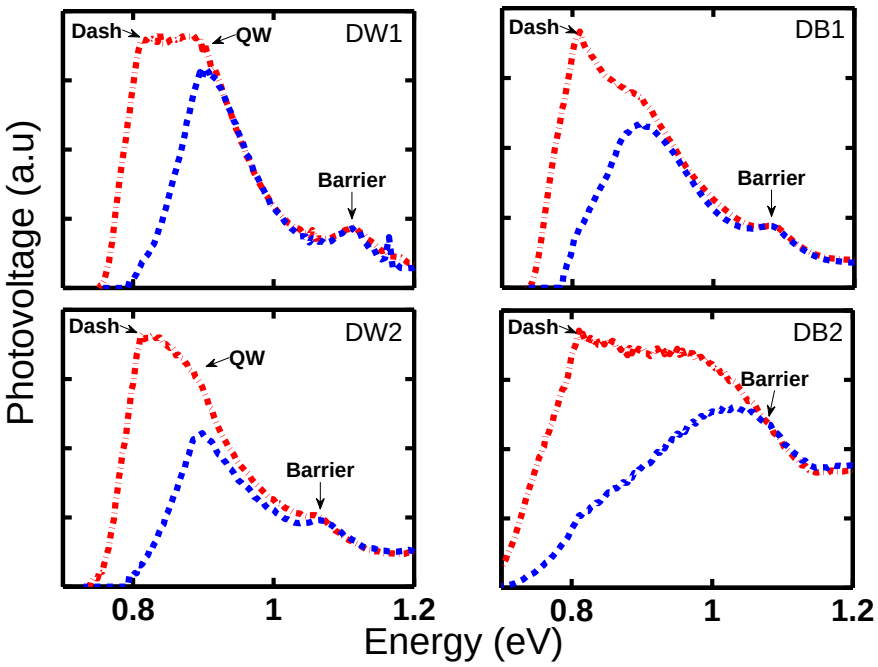

Figure 4.4: Polarized E-PV spectra for DW1, DB1, DW2 and DB2. The red dash-dot lines show $TE_{(1-10)}$-polarized spectra and the blue dash lines show TM-polarized spectra. Black arrows indicate the approximate energy of peaks corresponding to different transitions.

now the bottom left panel of Fig. 4.4 the spectrum for DW2 has similar spectral features to those seen in DW1. The polarized E-PV spectra measured in DB2 and included in the bottom right panel of Fig. 4.4 are much broader than in the other three samples. The lowest peak at $\sim$ 0.8 eV is attributed to transitions involving dash-like ground state heavy holes and electrons. The shoulder observed at $h\nu \approx$1.1 eV in DB2 is associated with bulk barrier transitions.

Dash Size Dispersion

Size and composition fluctuations in an ensemble of self organised quantum dashes leads to a distribution of energy levels and the presence of inhomogeneous broadening. The standard deviation (σ) of a Gaussian function fitted to the absorption edge of the $TE_{(1-10)}$-polarized E-PV spectrum, quantifies the amount of inhomogeneous broadening present in the ensemble. In the top panel of Fig. 4.5 a standard deviation of $\sim$ 30 meV is measured for the Gaussian function fitted to the $TE_{(1-10)}$-polarized E-PV spectrum for DW1. This value is used as the Gaussian broadening applied to the calculated absorption spectra in section 4.3. The estimate of the amount of inhomogeneous broadening is the same for DW1, DB1 and DW2 which have elongated dashes with in-plane dimensions of $\sim$ 20 nm (110) by $\sim$ 200 nm (1-10). The Gaussian function fitted to the DB2 $TE_{(1-10)}$-polarized E-PV spectrum can be seen in the bottom panel of Fig. 4.5 and has a standard deviation of $\sim$ 50 meV, indicating there is more dash size dispersion in this sample, as predicted by Gioannini [72]. The shorter (1-10) dimension in DB2 will contribute to a different distribution of energy states compared to DB1, as the in-plane dash dimensions are $\sim$ 20 nm by $\sim$ 40 nm along (110) and (1-10) respectively in DB2. The energy states along (1-10) form wire-like mini-bands in DB1, but such mini-bands are not as well defined in DB2. As both in-plane directions of the dash are significantly larger than the height, variations in the dash height and shape, as well as composition fluctuations are likely to contribute most to the inhomogeneous broadening.

To summarise, polarized E-PV spectroscopy is used to study transitions involving electrons and both HH and LH states and to differentiate between them. Results show that electron-LH transitions are suppressed at the band edge, in good agreement with the theoretical results presented in section 4.3. A Gaussian function is fitted to the absorption edge of the lowest energy state in order to estimate the amount of inhomogeneous broadening in the samples. The value measured for the elongated quantum dashes in DW1 is used to broaden the calculated absorption spectra in section 4.3.

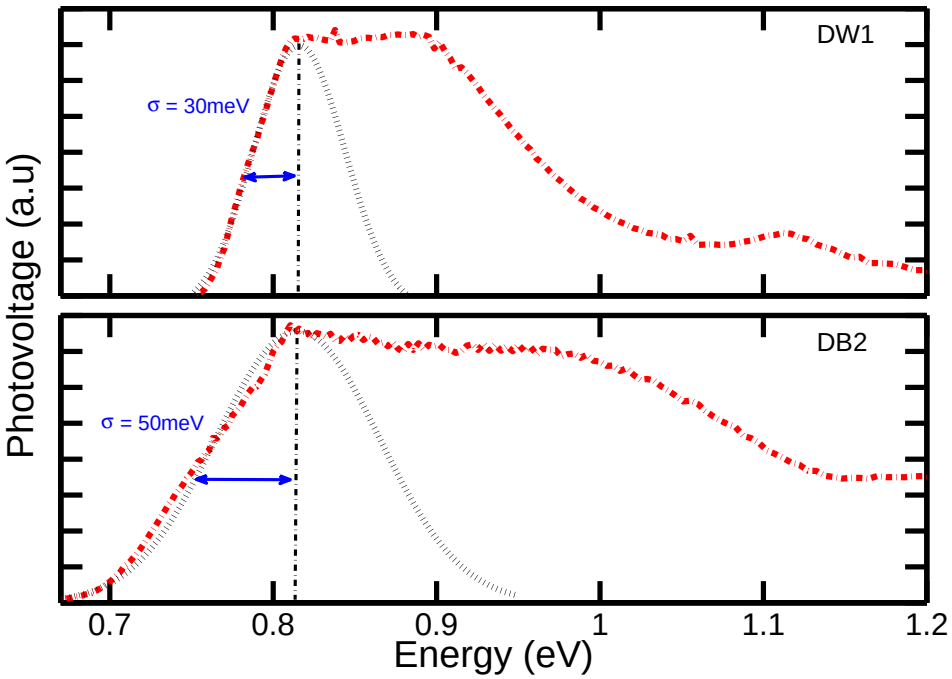

Figure 4.5: The red dash-dot line represents the $TE_{(1-10)}$-polarized E-PV spectrum for DW1 (top panel) and for DB2 (bottom panel) with a Gaussian function fitted to the absorption edge.

4.4.2 Anisotropy of TE Components of SE Spectra

The polarization anisotropy of the in-plane $TE_{(1-10)}$-polarized optical properties is a beneficial property of the dash structure, for example in vertical-cavity surface-emitting lasers (VCSELs) [65, 75], and also therefore to give higher gain and lower threshold for edge-emitting lasers that exploit the higher gain polarization direction [76]. The polarization anisotropy present in quantum dash samples is experimentally measured in this section and a good qualitative and quantitative agreement is found with the theoretical results summarised in section 4.3.

SE is measured through a window in the top contact of each device, using a polarizer to discriminate between $TE_{(110)}$ and $TE_{(1-10)}$-polarized emission. The collected SE spectra are corrected for spectral variations, again using the method described in Ref [53]. More information about the experimental set up and spectral correction used can be found in chapter 3. A sketch of the experimental set up is shown in Fig. 4.6, indicating the position of the window, the orientations of the dash and laser optical axis, and the different polarization directions. The calibration of this experimental set up is confirmed by measuring the polarized SE spectra from a multi quantum well sample. The results of this analysis are included in chapter 3 where, as expected [32], the measured $TE_{(110)}$ and $TE_{(1-10)}$

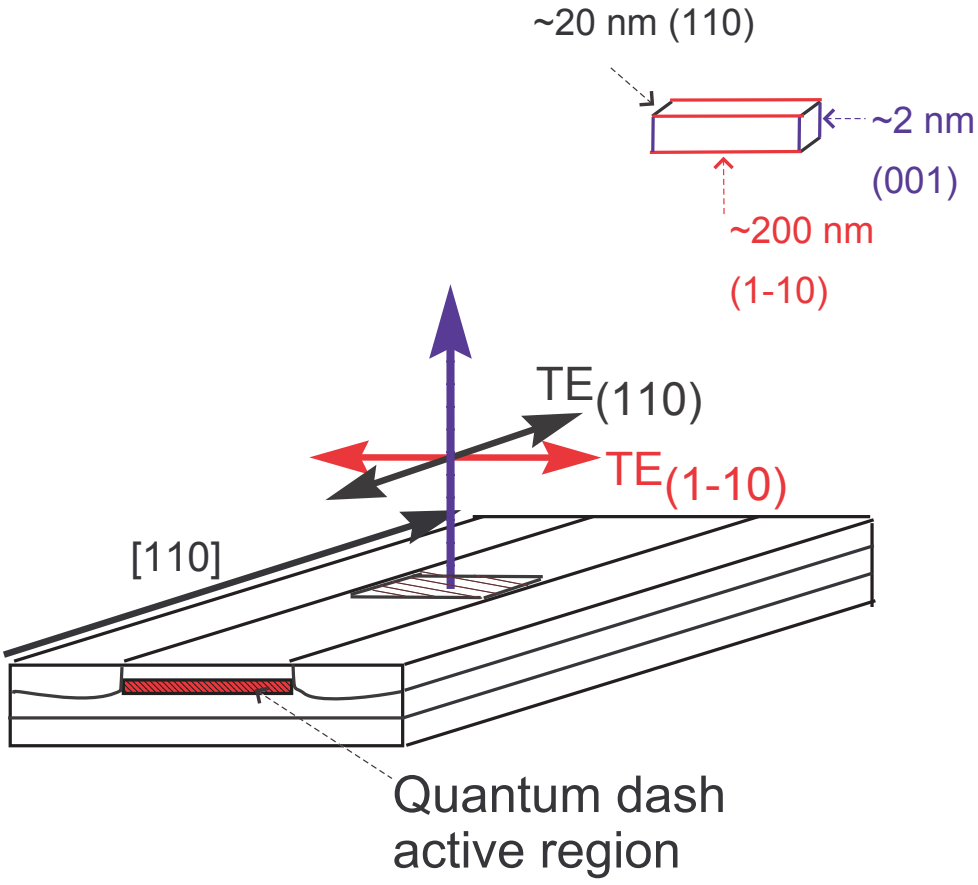

Figure 4.6: Schema of experimental set up for polarized SE measurements, where light is collected through a window in the top contact of the laser. A sketch of the dash orientation is shown in the top right.

polarized emission spectra have equal magnitude.

SE is collected for three laser samples (DW1, DB1 and DW2) below the lasing threshold to avoid any scattered laser light. Fig. 4.7 shows the measured SE spectra for DW1 (left panel) and DB1 (middle panel) at a current of 7 mA, corrected for spectral response. The spectral response correction leads to the large errors at low and high energy tails in all three panels of Fig. 4.7. The spectra collected for DW2 are not shown as they are similar to DW1. Polarized SE spectra are also collected through a window in the top contact of an SOA for DB2. The corrected spectra measured at a bias current of 61 mA are plotted in the right panel of Fig. 4.7. The current of the SOA was chosen so as to ensure the gain of the SOA was not saturated and that no amplified SE was coupled out of the window.

It is clear that there is an appreciable enhancement of $TE_{(1-10)}$ over $TE_{(110)}$ emission in all three panels of Fig. 4.7. Fig. 4.8 shows the ratio, r, of $TE_{(1-10)}$ to $TE_{(110)}$-polarized SE for DW1 (left panel), DB1 (middle panel) and DB2 (right panel) as a function of bias current. The ratio r does not depend on current,

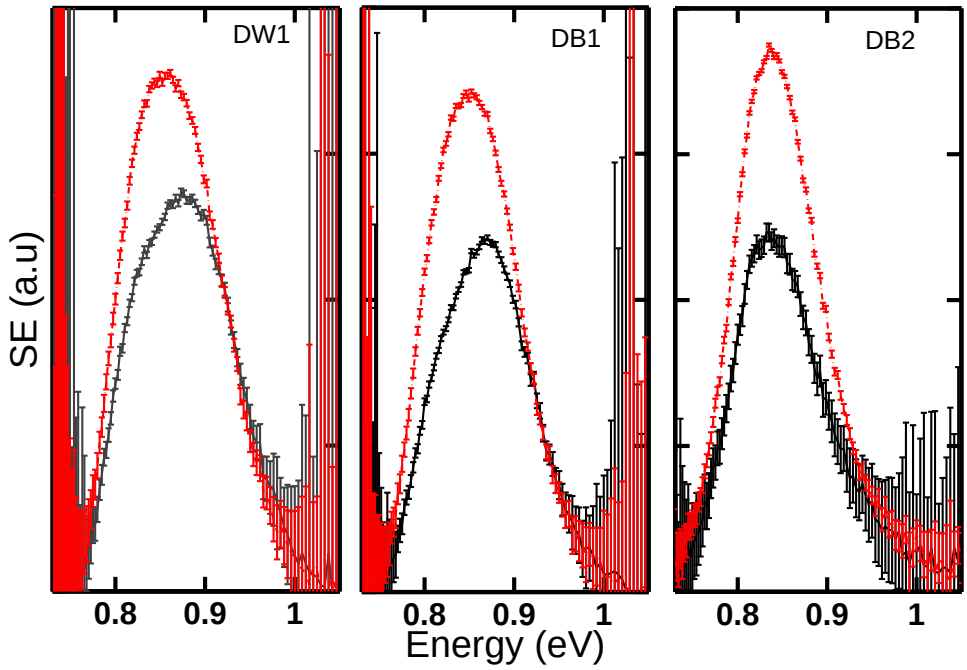

Figure 4.7: The $TE_{(1-10)}$ (red dash-dot) and $TE_{(110)}$ (black) SE spectra at 7 mA for DW1 (left panel) and DB1 (middle panel) and at 61 mA for DB2 (right panel). The large errors at the low and high energy tails are due to the spectral response correction.

indicating that it is an intrinsic property of the material. A good qualitative and quantitative agreement is seen between the measured ratio r for DW1 and DB1 and the ratio of the calculated absorption spectra, r, included in the bottom panel of Fig. 4.2.

Origin of TE Polarization Anisotropy

To understand the origin of the polarization anisotropy measured in the quantum dash samples, we recall the SE rate for a polarization, p, $R_{spon}(p, h\nu)$, written as in chapter 2

$$R_{spon}(p, h\nu) \propto h\nu \sum_{i}^{n_c} \sum_{j}^{n_v} |M_{ij}^{p}|^2 G\left(E_{c,i} - E_{v,j} - h\nu\right) \left(f_c(E_{c,i})(1 - f_v(E_{v,j}))\right) \quad (4.2)$$

where $|M_{ij}^{p}|$ is the momentum matrix element linking the conduction state with energy $E_{c,i}$ with the valence state with energy $E_{v,j}$ in each direction p ((001), (110) and (001)). $h\nu$ is the photon energy and $G(x)$ is a Gaussian broadening function included to account for the presence of inhomogeneous broadening in a real quantum dash ensemble. $f_c(E_{c,i})$ and $(1 - f_v(E_{v,j}))$ are the probability of occupation for an electron at $E_{c,i}$ in the conduction band and a hole at $E_{v,j}$ in the valence

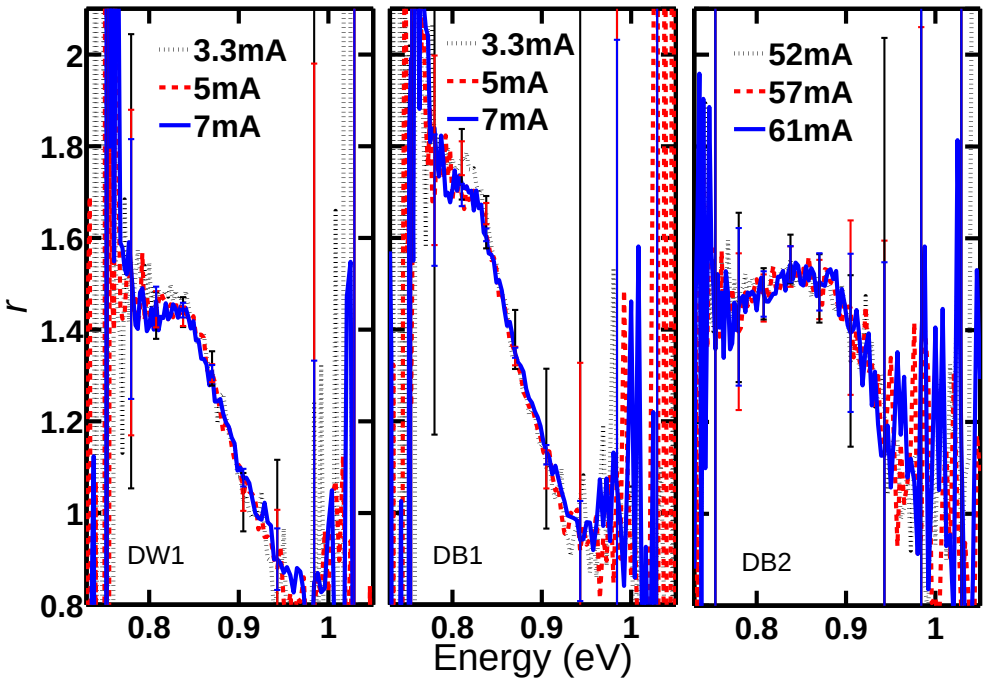

Figure 4.8: Ratio of SE spectra for DW1 (left panel), DB1 (middle panel) and DB2 (right panel) for three values of drive currents.

band.

In chapter 2 we showed that the ratio, r, of the two TE-polarized spectral components of the SE rate along (1-10) and along (110) is written as

$$r = \frac{R_{spon}^{TE_{(1-10)}}(h\nu)}{R_{spon}^{TE_{(110)}}(h\nu)} \propto \frac{\sum_{i,j}^{n_c,n_V} |M_{ij}^{(1-10)}|^2}{\sum_{i,j}^{n_c,n_v} |M_{ij}^{(110)}|^2} \tag{4.3}$$

and is the ratio of the square of the momentum matrix elements for $TE_{(1-10)}$ and $TE_{(110)}$-polarized recombination.

Considering the left panel of Fig. 4.8, $r \sim 1.5$ between 0.75< $h\nu$ <0.85 eV. Coupled with the E-PV spectra presented in Fig. 4.4 we see that the SE below 0.85 eV is due entirely to transitions involving anisotropic dash valence states. For $h\nu > 0.9\ eV$, the ratio r decreases below unity, as transitions involve well and barrier states with enhanced $TE_{(110)}$ character. In a quantum well matrix elements tend to have equal magnitude for recombination polarized along the (110) and (1-10) directions, due to the uniform distribution of carrier momentum along the two orthogonal directions in the well. Therefore the predicted and measured anisotropy below 0.85 eV is attributed to a larger momentum matrix element along (1-10) than along (110) for transitions involving quantum dash states.

The larger anisotropy in DB1 is attributed to a theoretically predicted larger dash

height and deeper lateral confinement potential for HH carriers in DB1 [77]. This leads to an enhancement of the wire-like characteristics of the dash and hence to the increase in r. A smaller ratio r (~ 1.5) is measured in DB2 compared to DB1. This reduction is attributed to the more dot-like dashes in this sample relaxing along both (1-10) and (110). Relaxation along (1-10) would not be expected in the other three quantum dash samples where the dashes are more elongated along (1-10).

To conclude polarized SE spectra are measured through a window fabricated into the top contact of a device to quantify the anisotropy of the TE-polarized components experimentally. A good qualitative and quantitative agreement is found between experiment and theory presented in section 4.3. The anisotropy is attributed to a larger momentum matrix element along (1-10) due to the effect of carrier confinement, strain and dash shape.

4.4.3 Recombination Processes and Optical Losses

In this section the recombination processes are studied in three laser structures with DW1, DB1 and DW2 active material. The DB2 laser is not investigated in detail as it is found to suffer from defect-related recombination.

Each sample is mounted in a closed-cycle helium cryostat capable of cooling between 40 K and 330 K. The set up used in this section is described in detail in chapter 3 but can be seen schematically in Fig. 4.9. Using a polished multimode fibre SE is collected through a window that has been milled in the substrate of the laser. The facet emission is also measured. The collection efficiency for both optical measurements is kept constant throughout. The integrated SE, L_{SE}, collected though the window is a lower bound measure of the radiative current, I_{rad}, as the contribution from TM-polarized SE (up to ~ 20 %), which cannot be measured through the window, is neglected.

Temperature Dependence of the Threshold Current and its Radiative Component

First the temperature dependence of the threshold current, I^{th}_{total}, and its radiative component, I^{th}_{rad}, are studied using an analysis presented in Ref. [39]. I^{th}_{total} is found by measuring the current for the onset of lasing from the facet. I^{th}_{rad} is extracted from the integrated SE. The analysis assumes that at low temperatures the current is dominated by radiative recombination enabling I^{th}_{rad} to be equated to I^{th}_{total} for temperatures $\leq$ 100 K. Fig. 4.10 shows a similar temperature dependence of I^{th}_{tot} and I^{th}_{rad} for both DW1 and DB1 in the left and middle panels respectively.

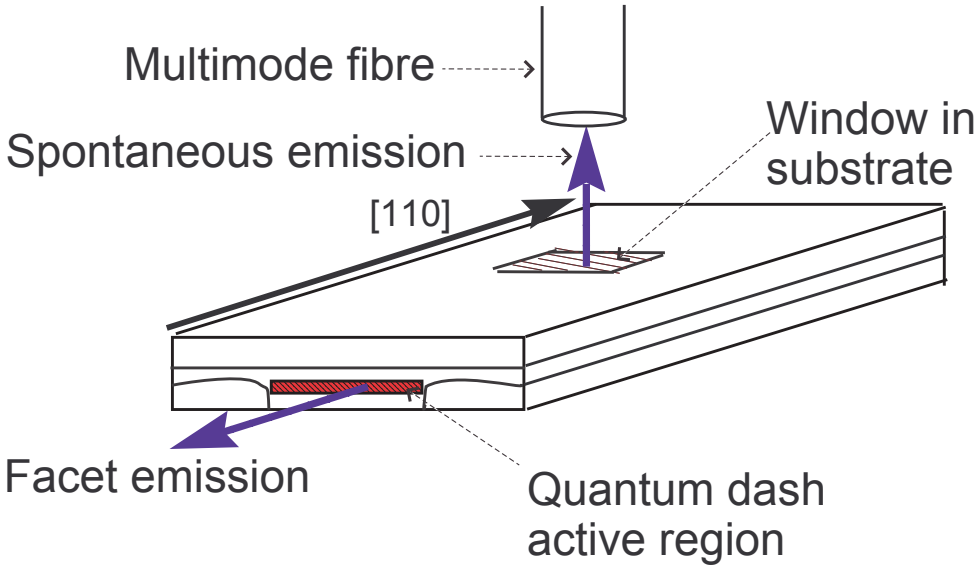

Figure 4.9: Schema of the experimental configuration for temperature dependent measurements. Spontaneous emission is collected through a window in the substrate of the laser. Facet emission is also measured. The collection efficiency is kept constant at the facet and window throughout the experiment.

Below 100 K, I^{th}_{total} and I^{th}_{rad} increase at the same rate with temperature supporting our assumption that radiative recombination dominates in this temperature range. At ∼130 K there appears a bump in the temperature dependence of the threshold current and its radiative component. A similar feature has been observed in 1.3μm undoped and p-doped quantum dot lasers [66, 67], where the effect is much stronger and occurs at a higher temperature. This anomalous variation in the temperature dependence of the threshold current has been attributed to poor carrier transport into and between dots leading to an increase in the threshold current at low temperature. The reduction in threshold current with increasing temperature is then due to improved carrier thermalisation at higher temperatures. The smaller bump at a lower temperature in the quantum dash lasers indicates that carrier localization is much weaker than in 1.3μm quantum dot lasers. The weaker localization and more rapid thermalisation of carriers is attributed to the theoretically predicted weak electron confinement and quantum wire-like valence band density of states in quantum dash lasers.
Above 150 K, I^{th}_{tot} increases more rapidly than I^{th}_{rad}, indicating the onset of a non-radiative recombination process. Between 200 K and 300 K I^{th}_{tot} increases with a characteristic temperature, $T_0 \approx 70$ K which is larger than values measured on other InGaAsP/InP-based lasers ($T_0 \approx 50 - 55$ K) [39, 78] indicating that quantum dash lasers can have improved temperature performance. The temperature dependence of I^{th}_{rad} with $T_0 \approx 200$ K in this range is accounted for by thermal

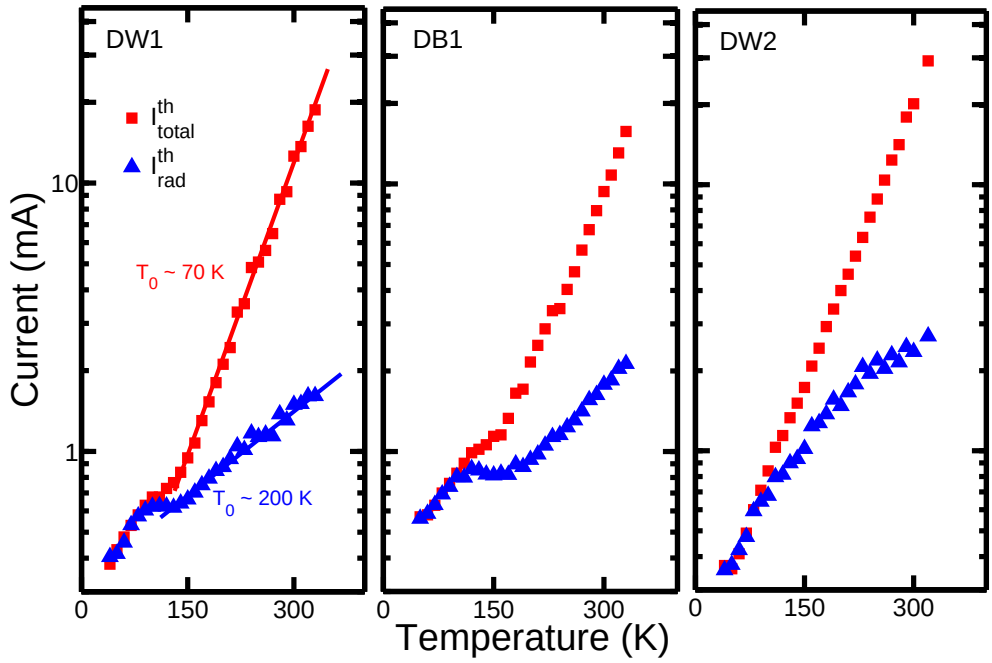

Figure 4.10: Plot of total threshold current, I^{th}_{total}, (filled red squares) and its radiative component at threshold, I^{th}_{rad}, (filled blue triangles) as a function of temperature for DW1 (left panel), DB1 (middle panel) and DW2 (right panel). The characteristic temperature, T_0, of I^{th}_{tot} and I^{th}_{rad} are also included for DW1.

broadening of the carrier distributions. At 300 K the internal quantum efficiency, η_i, defined as the ratio of radiative current to total current, is $\sim 10\%$ for DW1 and $\sim 20\%$ for DB1 at threshold. The room temperature value of η_i in DW1 is similar to that previously measured in other InP-based lasers [78, 79].

Considering the right panel of Fig. 4.10 we notice there is no bump in the temperature dependence of I^{th}_{tot} and I^{th}_{rad} for DW2 indicating improved carrier transport at low temperature. Above 150 K, the temperature dependence of I^{th}_{tot} behaves as in DW1 and DB1, indicating the onset of a non-radiative recombination process. We will return to discuss this further below.

To summarize, the temperature dependence of quantum dash lasers is attributed to the onset of a temperature-dependent non-radiative carrier process.

Current and Temperature Dependence of Carrier Recombination Processes

This section includes an analysis described in detail in chapter 2 to identify the dominant carrier recombination process as a function of current and temperature. It involves measuring the variation of the radiative current, I_{rad}, with total current, I_{tot}, as a function of temperature. The dominant recombination process can

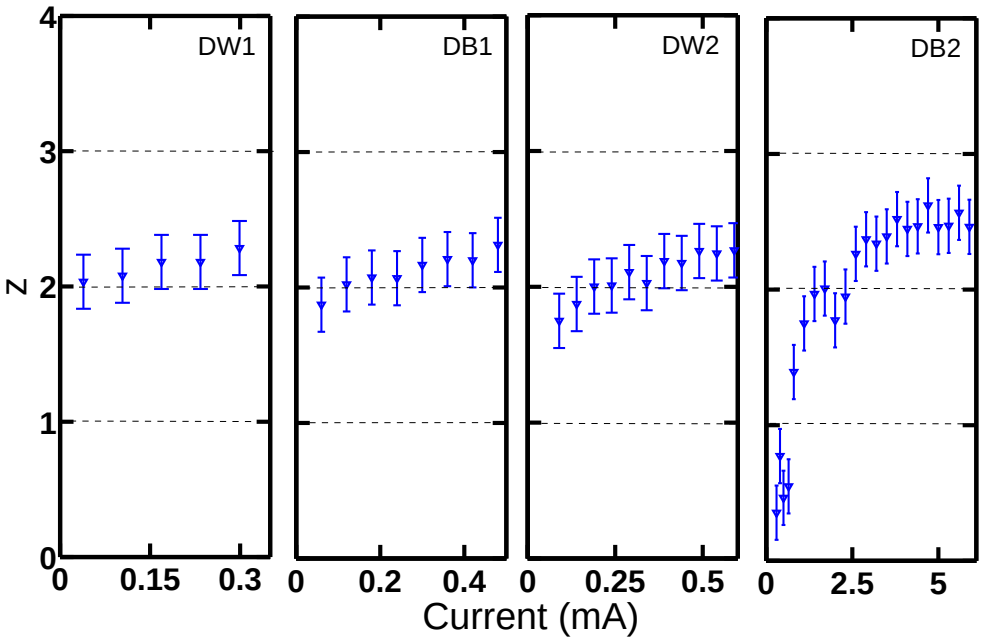

Figure 4.11: The power of the carrier density, z, as a function of drive current up to threshold for DW1, DB1, DW2 and DB2 at 100 K

be identified by finding the slope, z, of a plot of $ln(I_{tot})$ versus $ln(I_{rad}^{1/2})$.

First z is plotted at 100 K as a function of the total current, I_{tot}, up to threshold in Fig. 4.11. DW1, DB1 and DW2 are measured to be radiatively dominated, with $z \sim 2$ over the full current range, which is consistent with the normalisation of I_{rad}^{th} to I_{tot}^{th} at low temperatures in these lasers. In DB2 $z \sim 1$ at low currents, indicating the presence of defect-related monomolecular recombination. This is the reason for not investigating this sample further.

Fig. 4.12 shows the measured temperature dependence of the value of z at threshold, z_{th}, (blue diamonds) for DW1 and DB1 (left and middle respectively). In both lasers, $z_{th} \sim 2$ below 100 K and increases with increasing temperature. In DB1 $z_{th} \sim 3$ at 300 K consistent with Auger recombination as the dominant carrier recombination process. In DW1 $z_{th} \sim 3$ at 250 K, indicating the presence of Auger recombination. However above 250 K $z_{th} > 3$ in DW1, leading to a breakdown of the z analysis. This behaviour has previously been associated with the likely onset of a further non-radiative loss mechanism in this temperature range [39].

Temperature Dependence of the External Differential Quantum Efficiency

The z analysis presented above assumes the absence of leakage currents. However room temperature results for DW1 in Fig. 4.12 cannot be attributed to Auger

recombination alone as $z_{th} > 3$. The open red squares plotted on the right axes of Fig. 4.12 show the temperature dependence of the external differential efficiency, η_d^{ext}, normalised to its maximum value, $\eta_{d,norm}^{ext} = \eta_d^{eta}/\eta_d^{max}$, with $\eta_{d,norm}^{ext}$ plotted on a log_{10} scale. The maximum value of $\eta_{d,norm}^{ext}$ occurs around 150 K and 200 K for DW1 and DB1 respectively.

A small decrease in $\eta_{d,norm}^{ext}$ is seen for T $\leq$ 100K in DW1 and DB1, consistent with poor carrier transport and non-equilibrium distribution of carriers at low temperature. The negligible decrease in $\eta_{d,norm}^{ext}$ at low temperature indicates reduced carrier localisation in DW2. For DB1, increasing the temperature above 200 K results in an exponential decrease of $\eta_{d,norm}^{ext}$ to 50% at 300 K. By contrast, two distinct regions can be observed in the temperature dependence of $\eta_{d,norm}^{ext}$ in DW1; $\eta_{d,norm}^{ext}$ begins to decrease exponentially at 150 K and then starts to decrease more rapidly above 250 K. A correlation is observed between the second decrease in $\eta_{d,norm}^{ext}$ and $z_{th} > 3$ in the left panel of Fig. 4.12.

As outlined in chapter 2 a decrease in η_d^{ext} can be due to current spreading, current leakage or increased optical losses [38]. Current spreading is neglected because all samples are BH lasers. In DB1 the decrease in $\eta_{d,norm}^{ext}$ above 200 K is attributed to a temperature dependent optical loss, such as intervalence band absorption (IVBA). IVBA, which is described in detail in chapter 2, is often an issue in long-wavelength lasers where the energy separation between the split-off band and the HH band is equal to the band gap energy at finite wavevector k. The decrease in $\eta_{d,norm}^{ext}$ beginning at 150 K in DW1 is also attributed to IVBA. The additional loss mechanism in DW1 is most likely due to the development of a current leakage path with increasing temperature.

This assignment is supported by the measured room temperature variation of the SE spectra for DW1 and DB1 for currents above and below threshold, as shown in Fig. 4.13. SE from the barrier material is measured in DW1 (left panel) but is absent in DB1 (middle panel). SE clamps at threshold in DB1 but not in DW1, as seen in the insets of Fig. 4.13. The unclamped barrier emission above threshold in DW1 is consistent with the presence of a current leakage path [38].

This conclusion is supported further by analysing DW2, which is a laser with a narrower waveguide and more p-doping in the top contact but has a similar type of active region as DW1. Considering the right panel of Fig. 4.11, DW2 is radiatively dominated at low temperature. The right panels of Fig. 4.10 and 4.13 shows the threshold current characteristics and $\eta_{d,norm}^{ext}$ as a function of temperature for DW2. The absence of a bump in the threshold current and a negligible decrease in $\eta_{d,norm}^{ext}$ at low temperature indicate reduced carrier localisation in this sample. The value of z_{th} for DW2 increases from 2 to 3 with increasing temperature, but

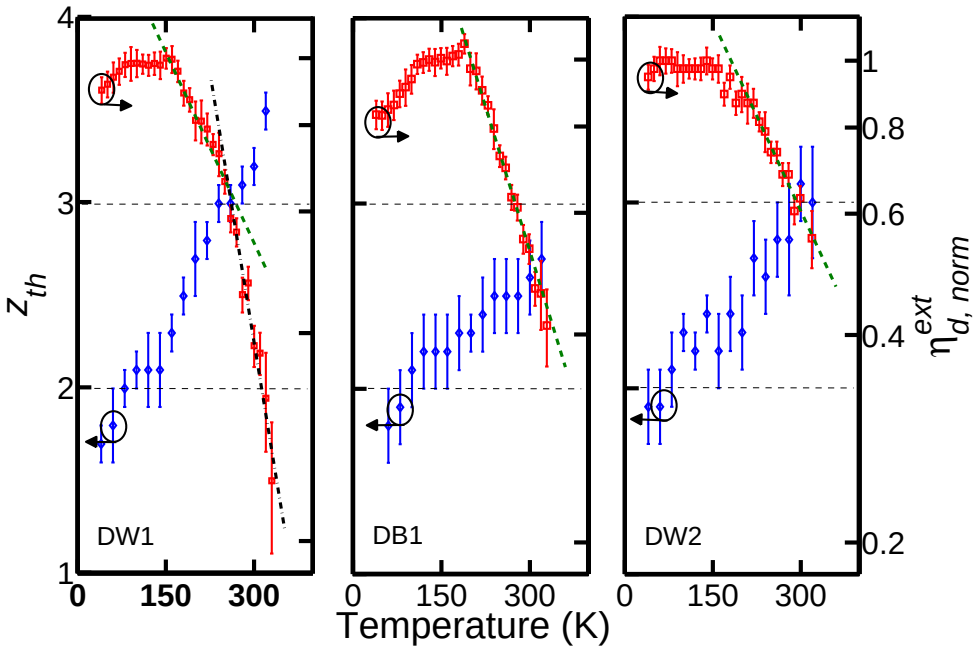

Figure 4.12: Plot of z_{th}(blue diamonds) and η_d^{ext} normalised to its maximum value (open red squares) as a function of temperature for DW1 (left panel), DB1 (middle panel) and DW2 (right panel)

does not exceed 3, indicating that Auger is the dominant recombination process at threshold in this laser at room temperature. $\eta_{d,norm}^{ext}$ shows a similar exponential decrease to that observed in DB1, with no second process observed to contribute to losses at higher temperature. Considering the right panel of Fig. 4.13 and the relevant inset, no barrier emission is measured and SE clamps at threshold in DW2 indicating the absence of a leakage path in this laser. It should be noted that the room temperature unpolarized SE spectra for DW1 and DB1 were measured on $\sim$ 300μm lasers while the DW2 laser was $\sim$ 600μm. Although it would be expected that a larger amount of barrier emission might be measured in a $\sim$300μm DW2 laser, the clamping of the carrier density at threshold in DW2 would not be expected to change. In summary, there is a clear correlation in DW1 between the onset of current leakage paths and a reduction in the external differential quantum efficiency. This leakage path is eliminated in DW2, which has a similar type of active region as DW1. Results of this analysis indicate that at room temperature Auger recombination remains dominant at threshold in quantum dash lasers and that in the absence of leakage currents the external differential quantum efficiency is limited by an optical loss. We also find that these quantum dash lasers have marginally improved temperature performance compared to InGaAsP/InP-based MQW and (311)B quantum dot lasers.

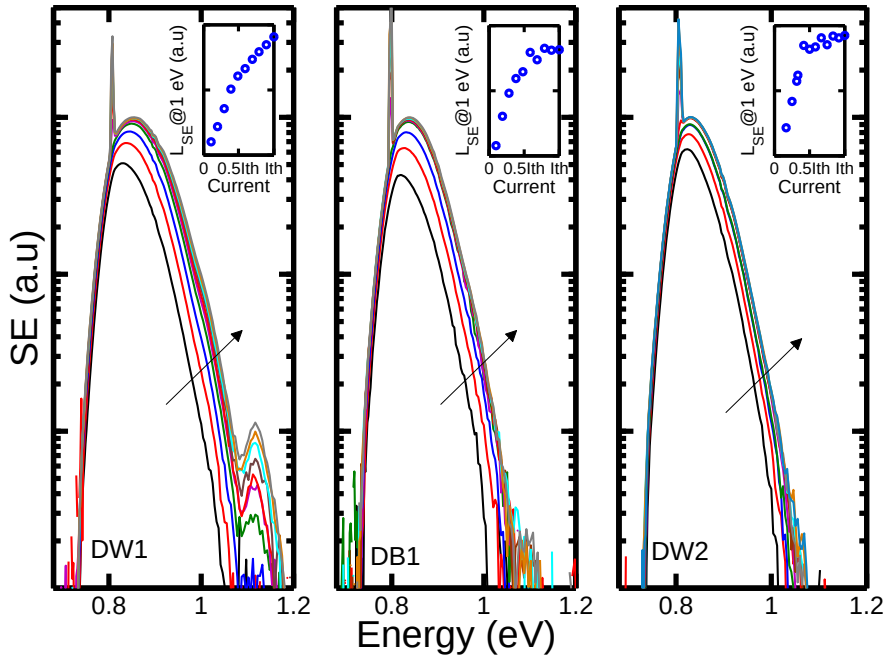

Figure 4.13: Plots of the unpolarized spontaneous emission as a function of current for DW1 (left panel), DB1 (middle panel) and DW2 (right panel). Data for DW1 (left panel) shows the presence of barrier emission which continues to increase above threshold. Insets: unclamped SE in DW1 at 1 eV, while SE measured at 1 eV clamps in both DB1 and DW2.

4.5 Summary

This chapter includes an analysis of InAs/InGaAsP/InP quantum dash lasers. An overview of the materials and devices studied is presented in section 4.2. Section 4.3 includes a summary of theoretical results calculated by Dr. Sorcha Healy. The model shows that, whilst the HH states are confined within the dash, the electron states in the DWELL are confined within the quantum well and are only weakly confined in the dash in the DBAR structure. An anisotropy of the optical properties is predicted due to the effect of carrier confinement, strain and dash shape.

The first part of the experimental analysis I have undertaken involves the study of the anisotropy in the optical characteristics in quantum dash materials, which is a beneficial property of the dash structure for laser applications. First polarized edge photovoltage spectroscopy is used to measure the suppression of electron-LH transitions at the band edge predicted by theory. Next polarized spontaneous emission spectra are analysed and the measured anisotropy of the in-plane polarizations is found to be in good qualitative and quantitative agreement with theory. The anisotropy, measured for transitions which involve dash states, is attributed

to an enhancement of the momentum matrix element along the long dash axis. Having established the anisotropy of the optical properties in quantum dash materials, the recombination processes present in quantum dash lasers are investigated in section 4.4.3. Results indicate that, at room temperature, Auger recombination remains the dominant intrinsic carrier recombination process at threshold despite the extra dimension of confinement provided by using a quantum dash active region. Further analysis suggests that in the absence of leakage paths an optical loss, such as IVBA, is the factor limiting the external differential quantum efficiency above $\sim$ 200 K. However, despite these limitations, the quantum dash lasers studied in this chapter have better temperature performance than conventional InGaAsP/InP quantum well [39] and (311)B quantum dot [78] lasers. The reduced temperature dependence of the threshold current and the anisotropy in the optical characteristics are of significant benefit for telecom laser applications.

Chapter 5

Recombination Processes in P-Doped Quantum Dash Lasers

5.1 Introduction

Quantum dots have been proposed as a means of increasing the modulation speed of lasers due to their potential to achieve a temperature insensitive threshold current and a high differential gain [4, 61], the latter enabling improved intrinsic modulation bandwidth of the laser.

In an ideal quantum dot there is a large energy separation between the ground state and other states. Carriers are confined in 3D electronic states and there is no thermal spreading of the injected carriers. This leads to the threshold current being temperature insensitive [4]. The energy levels of the electrons and holes are discrete in an ideal quantum dot and the quasi-Fermi levels separate symmetrically. Symmetric separation of the quasi-Fermi levels is beneficial as the differential gain is maximised when both quasi-Fermi levels are as close as possible to the band edge [32]. However due to the asymmetry in the electron and hole effective masses and charge neutrality under high injection conditions in a real quantum dot laser the quasi-Fermi levels separate more toward the valence band, as previously seen in quantum well lasers [32]. The symmetry of the quasi-Fermi level separation can be improved by p-doping the material as shown schematically in Fig 5.1.

A semiconductor is doped by adding a small controlled amount of another element, called a dopant. If this impurity atom has a greater number of valence electrons than the host semiconductor material, the extra electrons are known as donors and the semiconductor is n-doped. In the case of a p-doped semiconductor, the dopant has fewer valence electrons than the host material and accepts an electron from the valence band [80]. However p-doping the active region itself can alter the band structure near the band edge and degrade the laser performance [32]. A

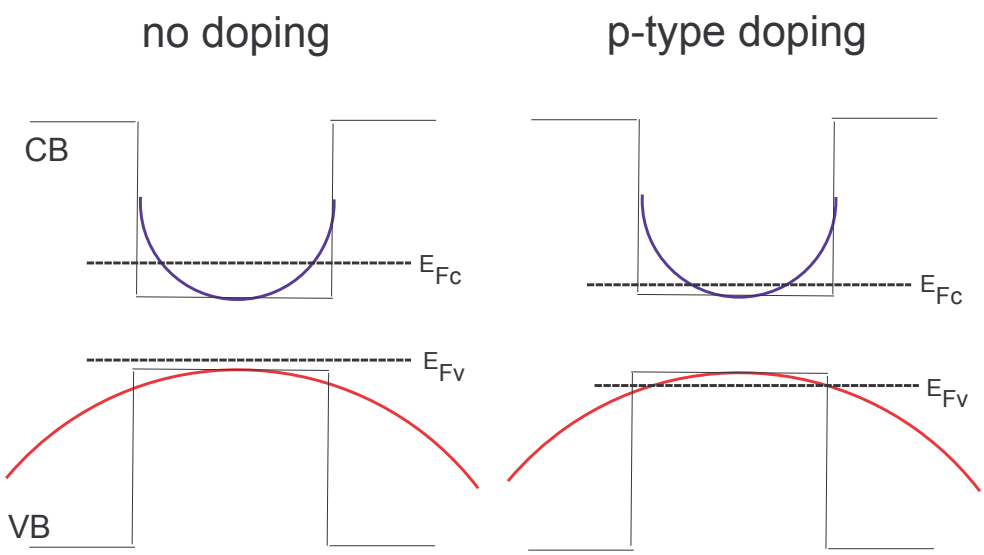

Figure 5.1: Illustration of how the quasi-Fermi levels are affected by p-type doping

symmetric separation of the quasi-Fermi levels can also be achieved by modulation doping where the dopant is placed in the barrier regions, and therefore physically separated from the active region [35].

Modulation-doping is widely used in electronic devices [80] and although modulation-doped quantum well and quantum dot lasers have been studied theoretically [81–83] and experimentally [84, 85] for twenty years, until recently they have not been widely used, due to problems such as increased optical loss and non-radiative recombination in quantum well lasers, and the initial difficulty in growing quantum dots. With the recent advances made in the growth of self-organised quantum dots, p-doping has once again been applied to quantum dot lasers. The impact of the p-doping is expected to be greater in quantum dots because of the reduction in the band edge density of states due to dot formation. Less dopant is therefore required than in quantum well lasers [82, 86–88].

As well as improving differential gain [82, 83, 87], other benefits have been theoretically predicted in p-doped quantum dots including a larger peak gain and later ground state gain saturation, as well as improved temperature performance [67, 89, 90].

The theoretically predicted benefits of p-doping have been investigated experimentally for InAs/GaAs quantum dot and for InAs/AlGaInAs/InP quantum dash lasers. A higher gain and differential gain at a given current compared to an undoped laser and later ground state gain saturation have been measured [86, 88, 91]. The higher differential gain has led to an improvement in the modulation bandwidth of the p-doped lasers [92, 93]. P-doped quantum dot lasers have also been

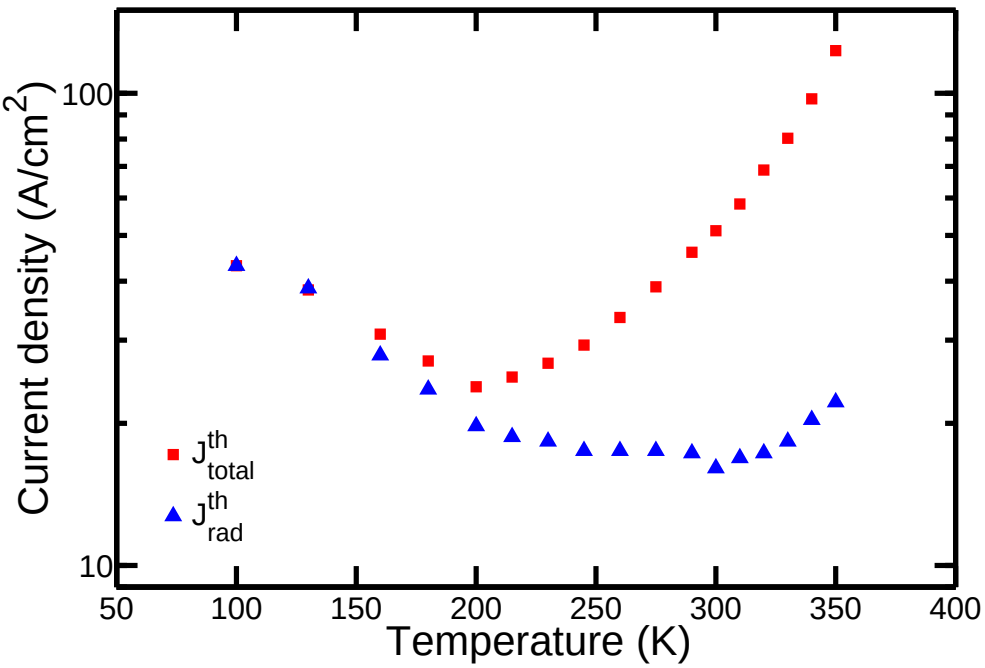

Figure 5.2: Plot of total threshold current density, J^{th}_{total},(filled red squares) and its radiative component at threshold, J^{th}_{rad},(filled blue triangles) as a function of temperature for an undoped InAs/GaAs 1.3 μm quantum dot laser, as in Ref [98].

found to have improved temperature performance with $T_0 \geq$150 K or even negative values of T_0 at room temperature [67, 86, 89, 91, 93–97] .

We measured for the undoped InAs/InGaAsP/InP lasers in chapter 4 a small bump in the measured threshold current as a function of temperature at lower temperatures ($T < 150\ K$) which we attributed to carrier thermalisation effects. At the lowest temperatures, once carriers are captured into the lowest energy states, the escape time for carriers to be excited from a given dot becomes too long to allow a thermal equilibrium distribution of carriers. As a consequence of the non-equilibrium carrier distribution, the threshold current density then increases with decreasing temperature. Similar, but stronger localisation effects are observed in undoped InAs/GaAs 1.3 μm quantum dot lasers, as illustrated for a typical device in Fig 5.2, where the total threshold current density, J^{th}_{total}, has a minimum value at $\sim$ 200 K, with the radiative component of the threshold current density, J^{th}_{rad}, continuing to decrease until room temperature [98]. The introduction of p-doping to InAs/GaAs quantum dot lasers further increases the thermalisation effects, thus accounting for the high or even negative T_0 values which are found in such devices [95].

Having gained an understanding of the undoped InAs/InGaAsP/InP material and its effect on lasers in chapter 4, this chapter includes an analysis both of

the localisation effects and of the recombination processes present in two p-doped InAs/InGaAsP/InP quantum dash lasers. Results are compared to those measured on a nominally identical undoped sample, to seek to identify the influence of p-doping in the case of quantum dash lasers.
Details of the samples studied in this chapter are included in section 5.2. The main results are presented in sections 5.3 to 5.5. Firstly the temperature dependence of the total threshold current and its radiative component are studied in section 5.3. As in other p-doped quantum dot lasers, carrier transport effects are found to be stronger in p-doped InAs/InGaAsP/InP lasers, with their influence persisting to a higher temperature than in the undoped sample. However, a more rapid thermalisation of carriers is measured in these p-doped quantum dash lasers compared to the p-doped 1.3 μm quantum dot devices. Next the dominant recombination processes present in the p-doped lasers are analysed as a function of current and temperature in section 5.4. Experimental results suggest that both p-doped samples suffer from defect-related recombination, which is quantified in section 5.5. We show for the p-doped laser where defect-related recombination is not dominant, that the threshold current remains dominated by Auger recombination at room temperature. We conclude with a summary of the work presented in this chapter in section 5.6.

5.2 Materials and Devices

This section presents an outline of the materials and devices studied in this chapter. Two sets of p-doped dash-in-a-barrier (DBAR) lasers are studied and compared to the undoped DBAR laser considered in detail in chapter 4. The material was grown at Alcatel – Thales III – V Lab using gas source molecular beam epitaxy on the commercially favoured (100) InP-substrate orientation [7, 68].

As outlined in chapter 4, the DBAR design involves growing InAs quantum dashes in an InGaAsP barrier layer, as shown schematically in Fig. 5.3, where the flat band profile for the undoped DBAR design is above and the modulation-doped DBAR design below. The undoped material, DB1, is made up of six stacks of dashes and has barrier and separate confinement heterostructure (SCH) layers which are 40nm and 80nm thick. As a laser referred to as DB2 has been studied in chapter 4, the p-doped materials will be referred to as DB3 and DB4, where DB3 thermalises before and has better characteristics than DB4. DB3 and DB4 also have six dash layers and have the same barrier and SCH layer thickness as DB1. However the 40nm barrier is made up of 20nm of Be-doped InGaAsP, sandwiched between two 10nm layers of undoped quaternary, as shown schematically in Fig. 5.3. The Be

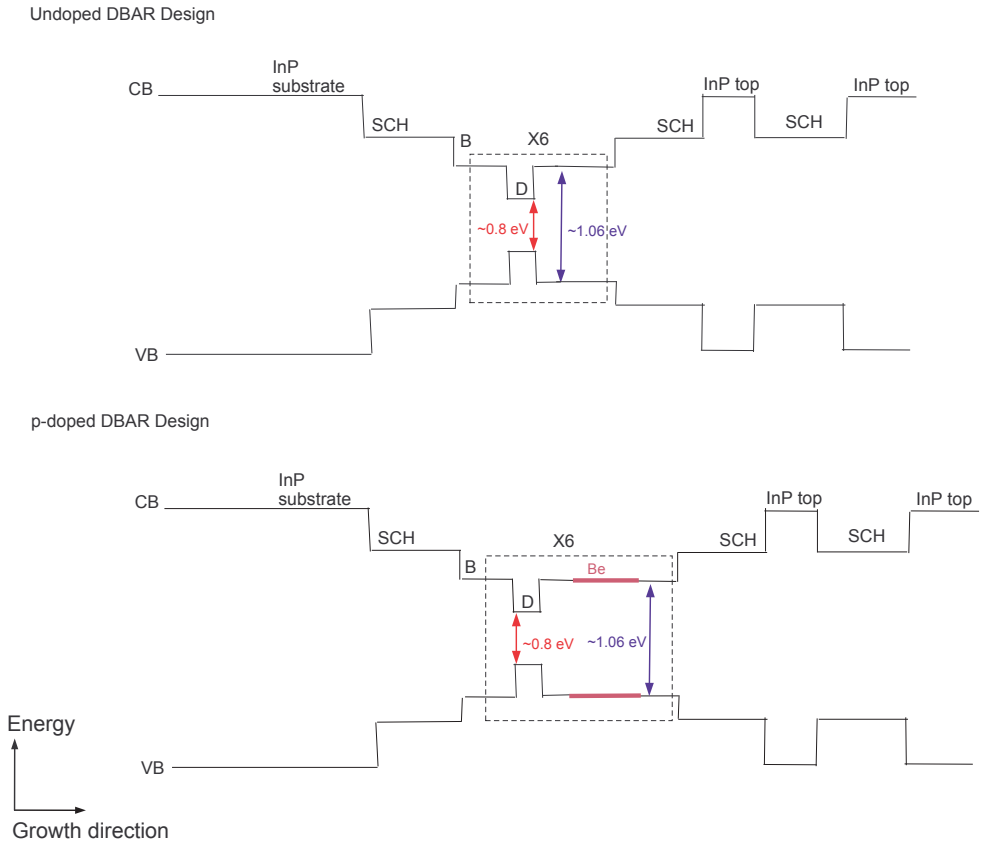

Figure 5.3: Flat band schema of the conduction and valence band profile of the undoped (top) and p-doped (bottom) DBAR design with 6 stacks of dashes. The energy of the dash (D) and barrier (B) transitions are included for both designs. The 20nm p-doped barrier is marked by the thick pink line in the p-doped DBAR design.

doping density is 1×10^{18} cm^{-3} in DB3 and 5×10^{17} cm^{-3} in DB4, equivalent to 80 and 40 acceptors per dash in DB3 and DB4 respectively. The dashes are elongated, with the long axis of the dashes oriented along (1-10) and the shorter axis along (110). The dashes have approximate in-plane dimensions of 20nm x 200nm along (110) and (1-10) respectively as in chapter 4. The typical dash height is $\sim$ 2nm.

The undoped DBAR material at processed by Alcatel – Thales III – V Lab into 600μm long buried heterostructure (BH) lasers with an active region width of 1.5μm and as-cleaved (C - C) facets, as described in chapter 4. In order to ensure the p-doped active region did not affect the laser, the two p-doped materials were processed by NanoPlus into 1200μm long ridge waveguide (RW) lasers with a ridge width and height of 2.5μm and a high-reflection (HR) coated back facet. The optical axis in both the BH and RW lasers is along the (110) crystal axis. Details of the three lasers are summarised in Table 5.1.

Table 5.1: Details of the three lasers studied in this chapter.

Device	Type	length (μm)	Facet	Be doping density (cm^{-3})
DB1	BH	600	C - C	0
DB3	RW	1200	C - HR	1×10^{18} cm^{-3}
DB4	RW	1200	C - HR	5×10^{17} cm^{-3}

5.3 Temperature Dependence of the Threshold Current and its Radiative Component

The p-doped RW lasers are studied as a function of current and temperature, but the results are best plotted as a function of current density when comparing the results to those measured on the undoped BH laser.

A closed-cycle helium cryostat system, described in detail in chapter 3, is used to study the temperature dependence of the recombination processes present in DB3 and DB4, from 40 – 330 K. Facet emission is collected through a window in the cryostat sample chamber and a polished multimode fibre is used to collect spontaneous emission, which is emitted through a window milled in the substrate of the laser. The collection efficiency at the facet and window remain constant throughout the measurement and the integrated SE, L_{SE}, collected though the window in the laser substrate, is a lower bound measure of the radiative current, I_{rad}, as outlined in chapter 4.

The temperature dependence of the threshold current density, J^{th}_{total}, measured in DB1, DB3 and DB4 is plotted on a log scale in the top row of Fig. 5.4. The larger value of the characteristic temperature, T_0, at room temperature in the p-doped lasers suggests improved temperature performance. However the reduced temperature dependence of J^{th}_{total} is at the expense of its magnitude. We cannot compare the exact value of the threshold current densities of the three lasers, due to the difference in length, device structure and facet coatings, but we do note that although the mirror losses are lower in the longer p-doped lasers, J^{th}_{total} is considerably larger in the p-doped lasers than the undoped laser at low temperatures, and slightly larger ($\sim 50\%$) at room temperature. At room temperature the larger threshold current may be due to internal losses, leakage current, defect-related recombination or current spreading. Due to the presence of p-doping, internal losses may be larger. As we are studying a DBAR design which was shown in chapter 4 not to have leakage currents, we expect leakage currents to be negligible in DB3 and DB4. We will show in section 5.4 both p-doped lasers suffer from defect-related recombination at room temperature. Current spreading affects the external differential quantum efficiency and the threshold current density in RW lasers [38],

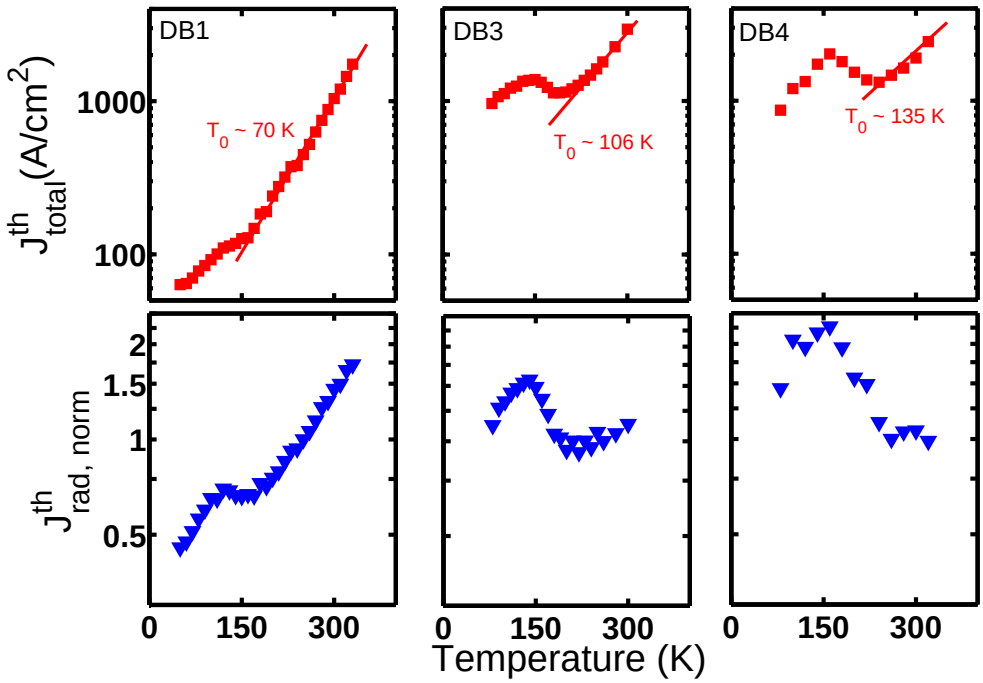

Figure 5.4: Plots on a log scale of the temperature dependence of the threshold current density, J^{th}_{total} (top panel), and its radiative component, J^{th}_{rad} arbitrarily normalised at 260 K (bottom panel), for DB1, DB3 and DB4 (left to right)

especially when the ridge width is narrow [99]. There are methods available to estimate the current spreading beyond the ridge [99, 100], but they require the knowledge of parameters such as the sheet resistance and carrier mobility of the material and are beyond the scope of this thesis. The presence of current spreading can be confirmed by measuring the spontaneous emission close to the facet [38]. We did not quantify the current spreading in DB3 and DB4 but expect it may play a role, as we are using 2.5 μm ridges. However we believe that the presence of current spreading will not change our conclusions.

Considering how J^{th}_{total} varies with temperature below 250 K, a larger bump at a higher temperature can be seen in DB3 and DB4 compared to the undoped sample, as previously measured in 1.3μm InAs/GaAs quantum dot lasers [67, 89, 95]. However the p-doped quantum dash lasers thermalise more quickly than the p-doped GaAs-based quantum dot lasers, leading to the temperature stable region being below 300 K. We attribute this more rapid thermalisation of carriers to the weaker electron localization in InAs/InGaAsP quantum dash states compared with InAs/GaAs quantum dot devices, as previously highlighted in chapter 4.

The measurement of an improved or negative temperature dependent threshold current in p-doped lasers has been attributed to a number of processes. It was originally suggested that it is the cumulative effect of decreasing Auger and radia-

tive current and the increase of leakage currents [89]. However, although the rate of Auger recombination decreases with increasing temperature due to an increase in the electron relaxation time [101], Auger recombination still increases with temperature as in bulk and quantum wells, contrary to the analysis presented by Fathpour *et al.* [89]. More recently Jin *et al.* analysed the temperature dependence of the threshold current of a p-doped laser by attributing it to a different filling of ground or excited states when the material is p-doped [67]. However, we believe the temperature dependence of the threshold current in p-doped lasers can be attributed to the interplay of carrier thermalisation and carrier recombination processes, as outlined in Ref [90]. The decrease in the threshold current at low temperature is attributed entirely to a decrease in the injection level required to reach a fixed gain, due to a more symmetric quasi-Fermi level separation in a p-doped laser. At these low temperatures the carriers are not in thermal equilibrium. A minimum in the threshold current is then measured when the carriers become thermally distributed at a higher temperature. The threshold current then increases again with temperature due to a combination of the increase in the injection level required to reach the set gain and the increase in non-radiative recombination. It has been suggested that the later carrier thermalisation in p-doped lasers is due to a more symmetric quasi-Fermi level separation and an increased confinement of electrons due to the presence of excess holes in a p-doped laser [90, 91, 95].

In addition to measuring the total threshold current, J^{th}_{total}, we have also measured the temperature dependence of the radiative component of the threshold current, J^{th}_{rad}. The results are shown on a log scale in the bottom row of Fig. 5.4, with J^{th}_{rad}, arbitrarily normalised to the value at 260 K. In both p-doped lasers $J^{th}_{rad,norm}$ decreases with increasing temperature over the same temperature range as J^{th}_{total}, and then remains almost constant up to 300 K. This behaviour is very different from the increase measured in DB1.

Comparing the top panels in Fig. 5.4, we see that J^{th}_{total} at 150 K is almost an order of magnitude larger in DB3 and DB4 compared to the undoped sample, DB1, but only $\sim 50\%$ larger at room temperature. This difference may arise due to the larger number of holes in the doped dashes at low temperature compared to the undoped dashes. The larger bump observed in J^{th}_{rad} for the doped samples then occurs because of a combination of thermalisation and doping density effects.

In summary, although both p-doped lasers have improved temperature performance compared to the undoped laser, a much higher threshold current is measured in both p-doped lasers at low temperatures, with the magnitude of the radiative current measured to decrease as the temperature rises above 150 K. We argue below how this is related to the large number of holes in the p-doped dashes at

low temperature, and also present evidence that there may be additional defect-related, non-radiative recombination in the p-doped samples.

5.4 Current and Temperature Dependence of Carrier Recombination Processes

In this section we analyse the total current, I_{tot}, and its radiative component, I_{rad}, as a function of temperature in order to identify the dominant carrier recombination process at threshold in two p-doped lasers. Using the analysis from chapter 2 for the undoped samples in chapter 4 we were able to assume that the total current, I_{tot}, can be written as a function of carrier density n as

$$I_{tot} = qV(An + Bn^2 + Cn^3) + I_{leakage} \tag{5.1}$$

where the electron density, n, is equal to the hole density, p, and where $qVAn$ describes monomolecular defect-related recombination; $qVBn^2$ is the radiative current; $qVCn^3$ is due to intrinsic, non-radiative, Auger recombination, and $I_{leakage}$ is due to leakage current paths. All four processes were described in detail in chapter 2. However the situation becomes more complicated in p-doped samples. If we assume P_0 holes are transferred into each dash from the acceptors and also assume overall charge neutrality, there will then be $p = (P_0 + n)$ holes in each dash when n electrons are injected into each dash. The radiative current, I_{rad}, will then be given in the Boltzmann approximation by

$$I_{rad} = qVBnp = qVBn(P_0 + n) \tag{5.2}$$

with

$$I_{rad} \approx qVBnP_0 \tag{5.3}$$

when $P_0 \gg n$, as expected to be the case at low temperature.
As described in chapter 2, Auger recombination involves recombination of a conduction band electron and valence band hole, followed either by excitation of a conduction band electron to a higher conduction band state, or else by excitation of a hole into a split-off valence band state. The former process, referred to as a CHCC Auger process, varies with the carrier density in the Boltzmann approximation as $I_{Auger}^{CHCC} = qVC_{CHCC}n^2p$, while the latter process, referred to as a CHSH Auger process, varies as $I_{Auger}^{CHSH} = qVC_{CHSH}np^2$. Theoretical and experimental analysis both support that CHSH is the dominant Auger recombination process in InGaAsP-based lasers [102, 103], so that the Auger recombination rate will then

vary with n as

$$I_{Auger} \propto qVCnP_0^2 \tag{5.4}$$

when $n \ll P_0$.

Finally defect-related recombination will also be limited by the electron density, n, when $n \ll P_0$, so that the total current in this case, is given by

$$I_{tot} = qV(An + BnP_0 + CnP_0^2) + I_{leakage} \tag{5.5}$$

Given the increased hole density in p-doped samples, we expect that the threshold electron density, n_{th}, will be reduced in p-doped samples compared to undoped samples. However the overall threshold hole density, $P_0 + n_{th} (\approx P_0)$, will be considerably higher at low temperature in the p-doped samples compared to the undoped case. It is also likely that $Bn_{th}P_0$ and $Cn_{th}P_0^2$ in equation (5.5) will be considerably larger in the p-doped samples than the equivalent terms in equation (5.1) for the undoped samples. This explains why the threshold current at low temperatures ($T < 150\ K$) is about an order of magnitude larger in DB3 and DB4 compared to DB1.

In chapter 4 we were able to identify that DB1 is radiatively dominated at very

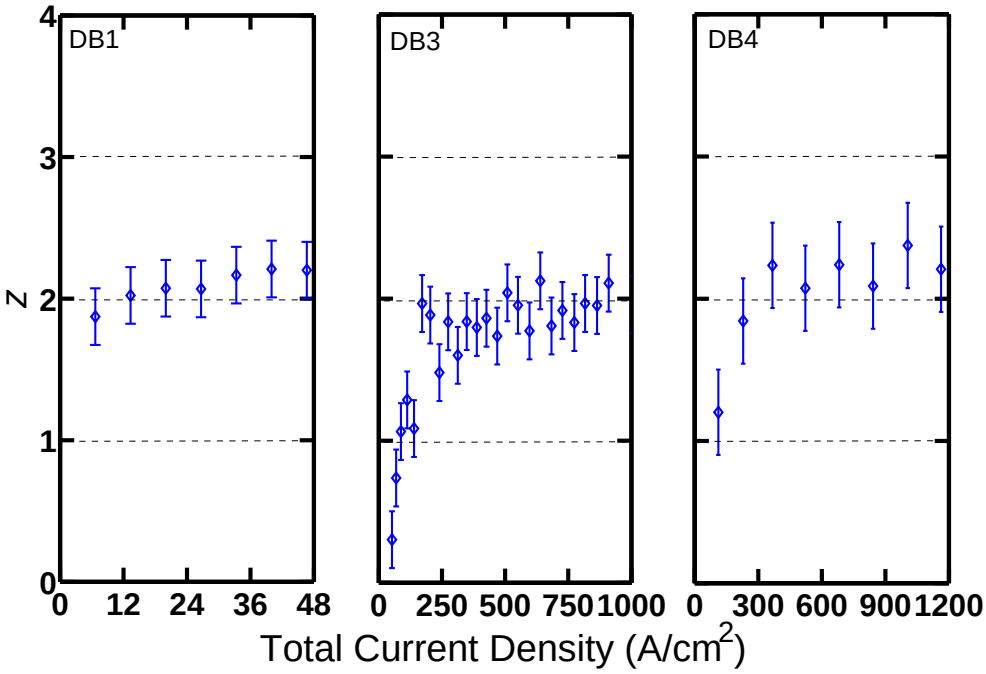

Figure 5.5: The measured variation of the coefficient, z, as a function of total current density up to threshold for DB1 (undoped), DB3 ($\sim$ 80 acceptors per dash) and DB4 ($\sim$ 40 acceptors per dash) at 100K.

low temperature, and to equate I_{rad} to I_{tot} for $T \leq 100\ K$. We see however that we can no longer do this in a p-doped sample assuming that $P_0 \gg n$ in each dash at very low temperature. We see from equation (5.5) that each of the recombination processes now varies linearly with injected carrier density, n. By analysing the value of z in the undoped sample, and finding $z \sim 2$ at low temperatures, we were able to conclude that Auger recombination is eliminated at low temperature in DB1. We cannot however from the present analysis determine whether Auger recombination is also eliminated at low temperature in DB3 and DB4. Firstly defect, Auger and radiative currents are expected to have a similar dependence on n at low temperature in DB3 and DB4, so cannot be distinguished using a z analysis. Secondly the overall magnitude of the Auger term at threshold, $\sim\ Cn_{th}P_0^2$, is expected to be considerably larger in the p-doped samples than in the undoped case, and could be significantly large to make a non-negligible contribution to the threshold current at low temperature. We expect that the relative importance of Auger could be determined, for example, by measuring the threshold current as a function of applied hydrostatic pressure at low temperature [39]. Laser emission frequency increases with hydrostatic pressure, Auger decreases with increasing energy gap while the radiative current at threshold tends to increase slightly with increasing energy gap. Hence the variation of threshold current with pressure could be used to determine the relative importance of the Auger and radiative current contributions at low temperature. Such a measurement is however beyond the scope of this thesis. Therefore, although $z \sim 2$ at low temperature in DB3 and DB4 in Fig. 5.5 we cannot use this result to identify the dominant recombination process. This is the reason for normalising J_{rad}^{th} at an arbitrary temperature of 260 K in the bottom panel of Fig. 5.4.

At threshold at room temperature, n is calculated to be ~ 25 electrons per dash in an undoped sample [77], while P_0 can be up to 80 and 40 holes per dash in DB3 and DB4 respectively. Although there are still more holes than electrons in DB3 and DB4, we expect that the form of the total current can be approximated by

$$I_{tot} = qV(An^{\alpha} + Bn^{\beta} + Cn^{\gamma}) + I_{leakage} \tag{5.6}$$

at higher temperatures close to and at 300 K, where the values of α, β and γ are not exactly 1, 2 and 3 as in equation (5.1) but where $\alpha < \beta < \gamma$. When defect-related recombination is the dominant recombination process, we then expect $\frac{\beta}{\alpha} < 2$ while $\frac{\gamma}{\alpha} > 2$ when Auger recombination is the dominant process.

Therefore we use the z analysis to investigate as far as possible the relative importance of the different current contributions at threshold in the p-doped devices, DB3 and DB4, assuming that I_{tot} is best described by equation (5.5) at low tem-

perature and by equation (5.6) at higher temperatures, close to 300 K.
In the following section we consider how the threshold value of z, z_{th}, changes with temperature for DB3 and DB4 as well as how z changes with current density at 300 K.

5.4.1 Temperature Dependence of Carrier Recombination Processes at Threshold

As outlined above care must be taken when applying the z analysis to p-doped lasers. At low temperature the effects of the dopant density per dash, P_0, dominate and we cannot identify different processes by their carrier density dependence. However as the temperature increases and carriers can start to escape we assume that the total current can be written as in equation (5.6).
We begin by considering the measured temperature dependence of the value of z at threshold, z_{th}, and plot it for DB1, DB3 and DB4 in Fig. 5.6. As seen in Fig. 5.5, $z_{th} \sim 2$ in all three lasers at very low temperature. In chapter 4 we identified radiative recombination as the dominant process at low temperature in DB1. However, as outlined above, we cannot use the measured value of z at low temperature to identify the dominant recombination process in DB3 and DB4, as each of the carrier recombination processes in equation (5.5) varies linearly with n. However as the temperature increases toward 300 K, we assume that the value of n approaches that of P_0 and therefore assume that the total current is more closely described by equation (5.6). Comparing the left and middle panel of Fig. 5.6 the temperature dependence of z_{th} is similar in DB1 and DB3, with $z_{th} \sim 3$ at 300 K, suggesting the dominance of Auger recombination at threshold in DB3. For $T \geq 150\ K$ in DB4 the value of z_{th} first increases toward 3, before falling toward 1.5 and reaching ~ 2 at 300 K. The unusual temperature dependence of z_{th} in DB4 requires further analysis in order to identify the dominant recombination process at threshold at 300 K in this laser.

We therefore plot z as a function of the total current density, J_{total} at 300 K for DB1, DB3 and DB4 in Fig. 5.7. We first consider the left and middle panels of Fig. 5.7. DB3 is seen to suffer from monomolecular defect-related recombination at low current densities, as $z < 2$, which is not the case in DB1. However z goes above 2 and toward 3 as the current increases, indicating that Auger is the dominant recombination process at threshold at room temperature in DB3. Considering now the right panel of Fig. 5.7, we observe that $z < 2$ up to threshold in DB4. This result suggests that defect-related recombination plays an important role in DB4 at room temperature, but that it may not be the only recombination process

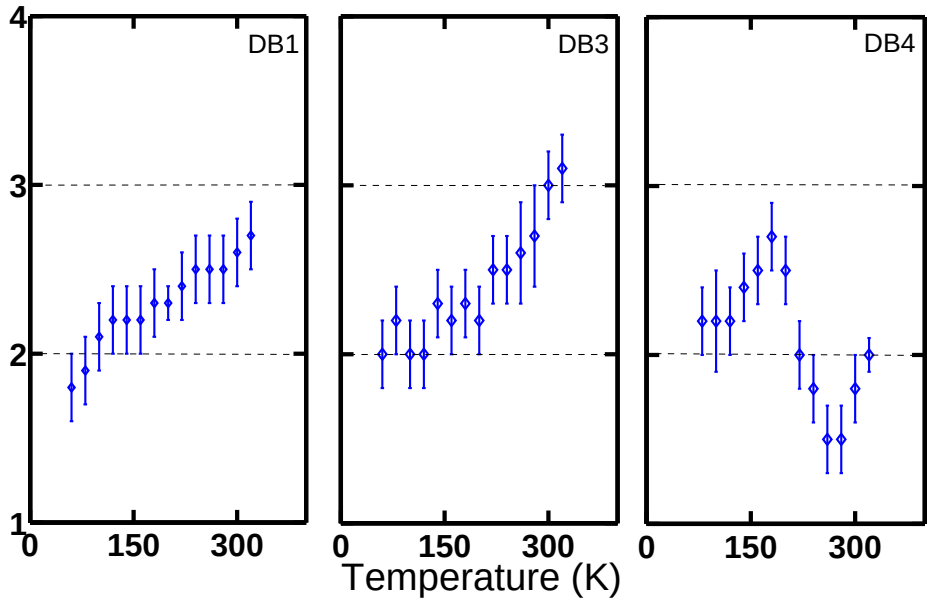

Figure 5.6: The power of the carrier density at threshold, z_{th}, plotted as a function of temperature for DB1 (undoped), DB3 ($\sim$ 80 acceptors per dash) and DB4 ($\sim$ 40 acceptors per dash).

present at threshold, where $z \sim 2$.

To summarise, although the z analysis cannot be used to differentiate between different recombination processes at low temperature in p-doped lasers, we can nevertheless study how z_{th} changes with temperature, as well as how z changes with current at room temperature, in order to identify the dominant threshold recombination process at 300 K in DB3 and DB4. DB3 is found to behave in a similar way to DB1 at threshold, indicating that Auger recombination is the dominant recombination process at 300 K, although defect-related recombination is present in DB3 at low current densities. Considering the same data for DB4 indicates that the dominant recombination mechanism is quite different to that in DB3. Our results suggest that DB4 suffers from a higher level of defect-related recombination than DB3. However the analysis cannot identify the dominant recombination process at threshold, because $z_{th} \sim 2$ in DB4 at 300 K, which should indicate that the laser is radiatively dominated. Therefore more than one recombination process may be playing a role at threshold at room temperature in this laser, as analysed further in the next section.

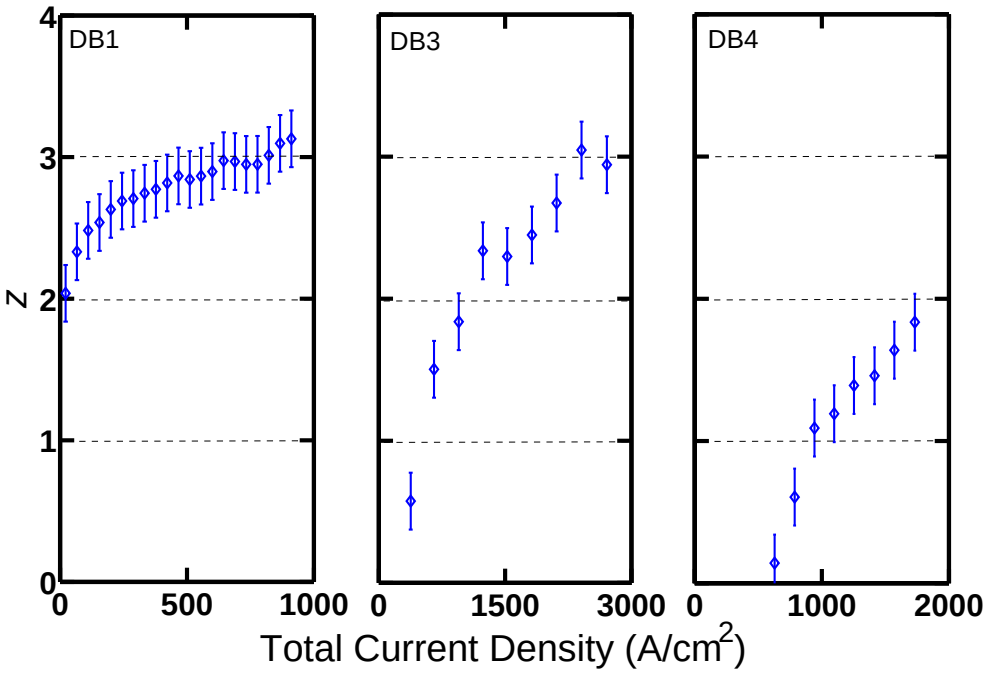

Figure 5.7: The power of the carrier density, z, as a function of total current density up to threshold for DB1 (undoped), DB3 ($\sim$ 80 acceptors per dash) and DB4 ($\sim$ 40 acceptors per dash) at 300K.

5.5 Quantifying Monomolecular Defect-Related Current and its Temperature Dependence

By quantifying the amount of current lost to defect-related recombination as a function of current and temperature, we gain an understanding of the different recombination processes present in DB4, and identify, in particular, which recombination processes dominate at threshold at room temperature in DB4.

The analysis, presented in Ref [104], involves plotting $ln(I_{total})$ versus $ln(L_{SE}^{1/2})$ at a given temperature and fitting a line of slope = 1 to estimate the monomolecular defect-related current, $I_{defects}$, to the current range over which it dominates. Plotting a line of slope 1 is based on assuming $\frac{\beta}{\alpha} = 2$ in equation (5.6), equivalent to $\alpha = 1$ and $\beta = 2$. Extrapolating the line of slope = 1 to threshold enables us to estimate the contribution of $I_{defects}$ to the total current at threshold.

5.5.1 Contribution of the Defect Current to the Total Current at Threshold at Room Temperature

First the contribution of $I_{defects}$ is studied at 300 K as seen in Fig. 5.8. A poor fit is observed between the line of slope = 1 and the DB1 data in the left most panel of Fig. 5.8. This is consistent with results presented in chapter 4 indicating DB1 to have no defect-related recombination pathway at 300K.

Applying the same analysis to DB3, a good fit between the line of slope = 1 and the experimental data is observed at low currents in the middle panel of Fig. 5.8. Looking at the linear fit, less than half of the total threshold current at 300 K is attributed to defect-related recombination. Although DB3 still suffers from defect-related recombination at threshold at room temperature, this result is consistent with Auger being the dominant recombination process, as identified in Figs. 5.6 and 5.7.

In the right panel of Fig. 5.8 the current range over which the line of slope = 1 fits the experimental data for DB4 is much larger than in DB3. This result indicates that more than three quarters of the threshold current is lost to defects and that DB4 is dominated by defect-related recombination at threshold at 300 K. However

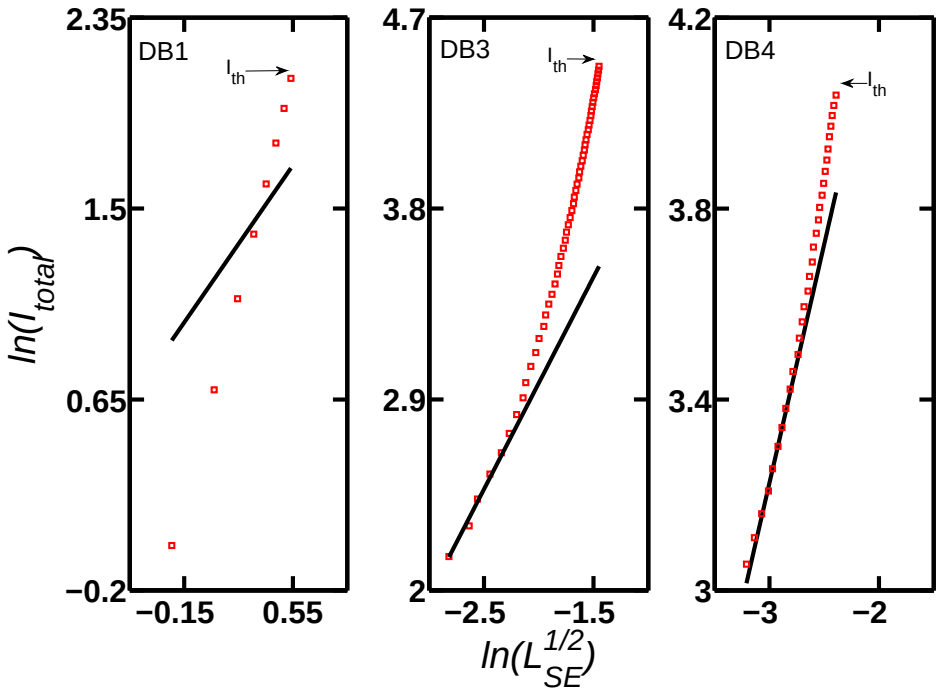

Figure 5.8: Plot of $ln(I_{total})$ versus $ln(L_{SE}^{1/2})$ (open red squares) up to threshold, I_{th} at 300K for DB1 (undoped), DB3 ($\sim$ 80 acceptors per dash) and DB4 ($\sim$ 40 acceptors per dash) at 300K. The black line, with slope = 1, represents the monomolecular defect-related current, $I_{defects}(\propto$ An).

in the presence of defect-related recombination only one would expect $z_{th} < 2$ in DB4 at 300 K, which is not the case. In the following section we therefore consider how the contribution of $I_{defects}$ to the threshold current changes with temperature.

5.5.2 Temperature Dependence of Monomolecular Defect-Related Current at Threshold

Having identified monomolecular defect-related recombination as the dominant process in DB4 at 300 K, the threshold value of $I_{defects}$, $I^{th}_{defects}$, is investigated as a function of temperature in order to clarify why $z_{th} \sim 2$ in DB4 at 300 K. Plotted in the top panels of Fig. 5.9 is the temperature dependence of the monomolecular defect-related current, $I^{th}_{defects}$, in both p-doped lasers. For low temperatures $I^{th}_{defects}$ is similar in both p-doped lasers, however as outlined above, care must be taken with this analysis at low temperature, as each recombination process in equation (5.5) varies linearly with injected carrier density, n. We see that in DB4 that $I_{defects}$ increases more strongly with temperature than in DB3. Plotted in the

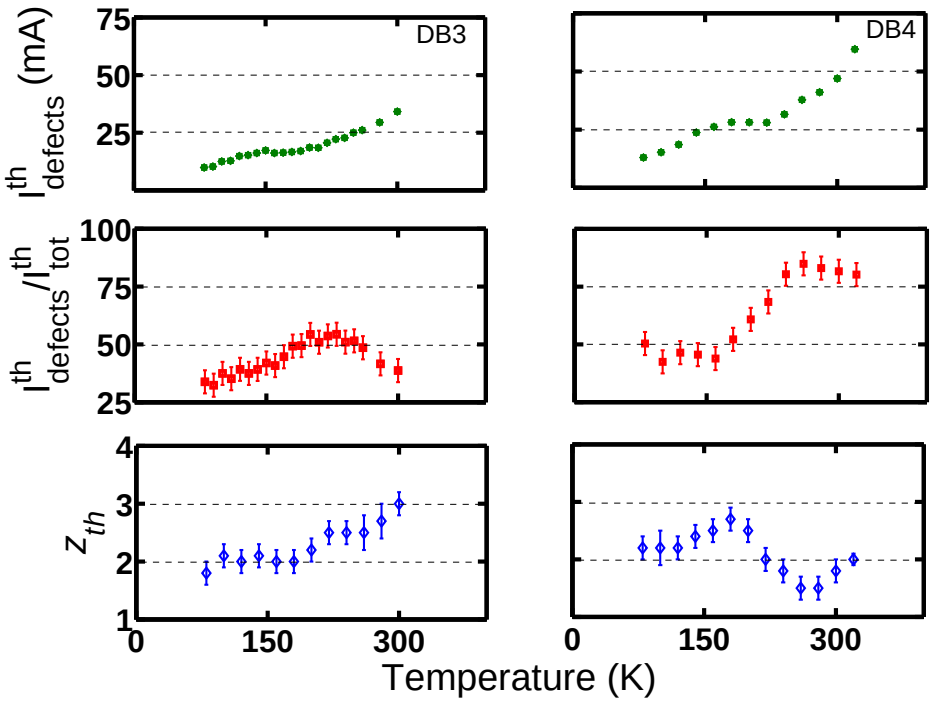

Figure 5.9: In this figure all the plots in the left panel are for DB3 ($\sim$ 80 acceptors per dash), while those in the right panel are for DB4 ($\sim$ 40 acceptors per dash). Top row: Plot of the temperature dependence of the monomolecular defect-related current at threshold, $I^{th}_{defects}$. Middle panel: Plot of the temperature dependence of the ratio of the monomolecular defect-related current at threshold, $I^{th}_{defects}$, to the total threshold current, I^{th}_{tot}. Bottom row: The threshold value of z, z_{th} as a function of temperature.

middle panels of Fig. 5.9 is the ratio of $I^{th}_{defects}$ to the total threshold current, I^{th}_{tot}, as a percentage. We see that the contribution of $I_{defects}$ increases strongly with temperature and begins to dominate above 180 K in DB4.
The temperature dependence of z_{th} in DB4, plotted in the bottom right panel of Fig. 5.9, can be understood by considering that the dominant monomolecular process ($z_{th}< 2$) may be coupled with Auger recombination ($z_{th}> 2$), leading to the measured $z_{th} \sim 2$ in DB4. DB3 may also suffer at low current densities from the monomolecular non-radiative defect-related recombination process present in DB4, but in this laser it is not dominant. In summary the value of $z_{th} \sim 2$ at room temperature in DB4 is attributed to the interplay between a monomolecular defect-related recombination process, which dominates above 180 K, and intrinsic Auger recombination.

5.6 Summary

In summary this chapter provides an analysis of two p-doped InGaAsP-based quantum dash lasers grown on InP. Modulation doping and the benefits of p-doping are reviewed in section 5.1. An overview of the materials and devices studied are included in section 5.2 while the results can be found in sections 5.3 to 5.5. We study the temperature dependence of the total threshold current density for two p-doped lasers as well as a nominally identical undoped quantum dash laser in section 5.3. P-doping leads to a reduction in the temperature dependence of threshold current density at room temperature, as previously measured in InAs/GaAs quantum dot lasers. InAs/InGaAsP/InP quantum dash lasers thermalise more quickly than GaAs-based quantum dots lasers, due to weaker electron localization, as seen in chapter 4. This leads to the most temperature stable region being below 300 K in p-doped InAs/InGaAsP/InP quantum dash lasers. The reduced temperature dependence of the threshold current density in the p-doped lasers is however at the expense of the magnitude of the threshold current density, especially at low temperatures where the effects of the p-dopant dominate.
We find that both p-doped samples have similar threshold current densities (J^{th}_{tot} and J^{th}_{rad}) and similar temperature performance. However results indicate that the dominant recombination process at threshold at 300 K is very different in DB3 and DB4. Due to the presence of a dopant care was taken when using the z analysis to identify the dominant carrier recombination process, especially at low temperature. Results on DB3 indicate that although defects are present at low current densities, Auger recombination is the dominant recombination process at threshold at room temperature, as in the undoped DB1 laser. DB4 seems to be

dominated by a monomolecular recombination process above 180 K. This process, coupled with intrinsic Auger recombination, leads to $z_{th} \sim 2$ in DB4.
It has been suggested [85, 94] that it may be possible to optimize p-doped lasers so that the benefits of a more symmetric movement of the quasi-Fermi levels outweigh problems such as the increased non-radiative recombination. However in an undoped InAs/InGaAsP/InP quantum dash laser, the integrated density of states for electrons and holes is not as asymmetric as in MQW or InAs/GaAs quantum dots, due to the difference in electron and hole confinement, suggesting that p-doping may therefore not have as strong a beneficial effect on the movement of the quasi-Fermi levels as expected as in p-doped InAs/GaAs quantum dot lasers [77, 105].

Chapter 6

Analysis of InAs/AlGaInAs/InP Quantum Dash Lasers

6.1 Introduction

Lasers which emit at 1550 nm are usually based on quantum wells grown on an InP substrate. There are two competing material systems, InGaAsP wells and barriers or AlGaInAs wells and barriers grown on InP. InGaAsP/InP is the most widely used combination. However the conduction band offset is low between InGaAsP wells and barriers, as shown schematically for InGaAsP/InP in the left panel of Fig. 6.1, leading to a poorly confined electron. Poor electron confinement can lead to electrons leaking out of the well, and leakage currents degrade laser performance.

Growing AlGaInAs structures on InP, shown schematically in the right panel of Fig. 6.1, leads to a different band line up. The conduction band offset in this material system is larger than in InGaAsP/InP so electrons are well confined in the well. The presence of aluminium lowers the barriers in the valence band, so holes are not as well confined as in InGaAsP/InP. The loss of hole confinement is less important than the increase in electron confinement in AlGaInAs/InP, due to the larger hole effective mass.

Although the improved electron confinement in AlGaInAs/InP has been known for a number of years [21], InGaAsP/InP remains more widely used. Using AlGaInAs makes device processing more challenging as the aluminium alloys oxidise. The oxidation of aluminium-containing materials makes it more difficult to etch and regrow material and is also detrimental to device reliability. However in recent years problems related to processing AlGaInAs-based multi quantum well (MQW) devices have been addressed [21, 106]. AlGaInAs/InP MQW lasers now show improved performance over InGaAsP-based MQW lasers [21, 106, 107]. There is

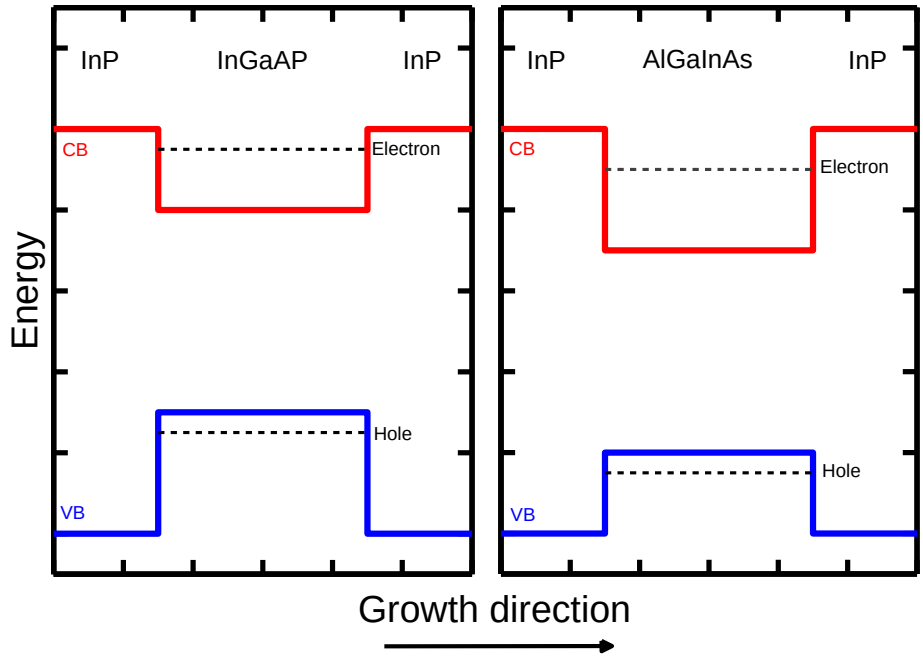

Figure 6.1: Schematic illustration of how the confinement of the electron and hole states are different in InGaAsP/InP and AlGaInAs/InP. The conduction band offset is larger in presence of AlGaInAs than InGaAsP. The holes are not as well confined in AlGaInAs/InP but the loss of hole confinement is less important due to the larger hole effective mass.

therefore an interest in growing quantum dots on Al-containing materials, in order to obtain improved temperature performance as well as 3D carrier confinement. InAs quantum dots, grown in AlGaInAs on the commercially favoured (100) InP-substrate orientation, are elongated and known as *quantum dashes*. These dashes have the long dash axis along the (1-10) crystal plane [108–110] similar to InAs dashes grown on InGaAsP/InP.

The aim of the work in this chapter is to compare the characteristics of AlGaInAs-based quantum dashes with those of the InGaAsP-based dashes studied in chapter 4. An overview of the materials and devices studied in this chapter is included in section 6.2. We summarise in section 6.3 the theoretical results presented for InAs/AlGaInAs/InP quantum dash-in-a-well (DWELL) and quantum dash-in-a-barrier (DBAR) materials [37, 72, 111], which are relevant to the interpretation of experimental results presented in section 6.4.

The anisotropy of the optical properties in InAs/AlGaInAs/InP quantum dash material is studied in sections 6.4.1 and 6.4.2. We first use polarized edge-photovoltage spectroscopy to confirm the theoretically predicted suppression of TM-polarized recombination at the band edge. Next polarized spontaneous emission measurements are taken through a window in the top laser contact. The results

confirm that InAs quantum dashes grown on AlGaInAs/InP have anisotropic in-plane optical characteristics, as shown in chapter 4 for InAs/InGaAsP/InP quantum dashes.
The second part of the analysis included in section 6.4.3 involves studying the recombination processes present in InAs/AlGaInAs/InP quantum dash lasers by comparing the radiative current to the total current at room temperature. It was intended to carry out a full analysis of the devices from 40 K to 330 K. However it was found that both the DWELL and DBAR devices degraded rapidly when low temperature measurements were carried out. At room temperature, the DWELL laser suffers from defect-related recombination, which is quantified in section 6.4.4 and found to be the dominant recombination process. Leakage currents play a significant role in the DBAR laser, as previously suggested by Marko *et al* [112]. In the absence of defect-related recombination and leakage currents the temperature performance of these 1.55 μm InAs/AlGaInAs/InP quantum dash lasers appears to be limited by Auger recombination as in AlGaInAs/InP MQW lasers [107]. Therefore the laser characteristics of AlGaInAs/InP quantum dash lasers may improve in the presence of intrinsic carrier processes only. It was not however possible to test or quantify this possible improvement because of the presence of defect-related recombination and leakage-related losses, and the device degradation at lower temperatures. A summary of the work presented in this chapter is included in section 6.5.

6.2 Materials and Devices

This section includes an outline of the materials and devices studied in this chapter. The material was grown at the University of Würzburg by gas source molecular beam epitaxy on the commercially favoured (100) InP-substrate orientation [110] and is made up of four stacks of dashes. All layers except the quantum dashes are lattice-matched to InP and the dash density is $\sim$ 2 x 10^{10}cm^{-2}.
Two sets of devices are studied. The first set, Al-DW, has an asymmetric dash-in-a-well (DWELL) active region design, where InAs dashes are embedded in a 10 nm AlGaInAs quantum well ($\sim$ 0.89 eV). The quantum wells, which consist of 4 nm below and 6 nm above the dashes, are separated from each other by 10 nm of AlGaInAs barriers ($\sim$ 1.05 eV). The second set of devices studied, Al-DB, has a dash-in-a-barrier (DBAR) active region design. Four InAs dash layers, each separated by 15 nm AlGaInAs barriers ($\sim$ 1.05 eV), were grown under identical conditions to Al-DW [110].
The schematic flat band profile for the DWELL and DBAR designs can be seen

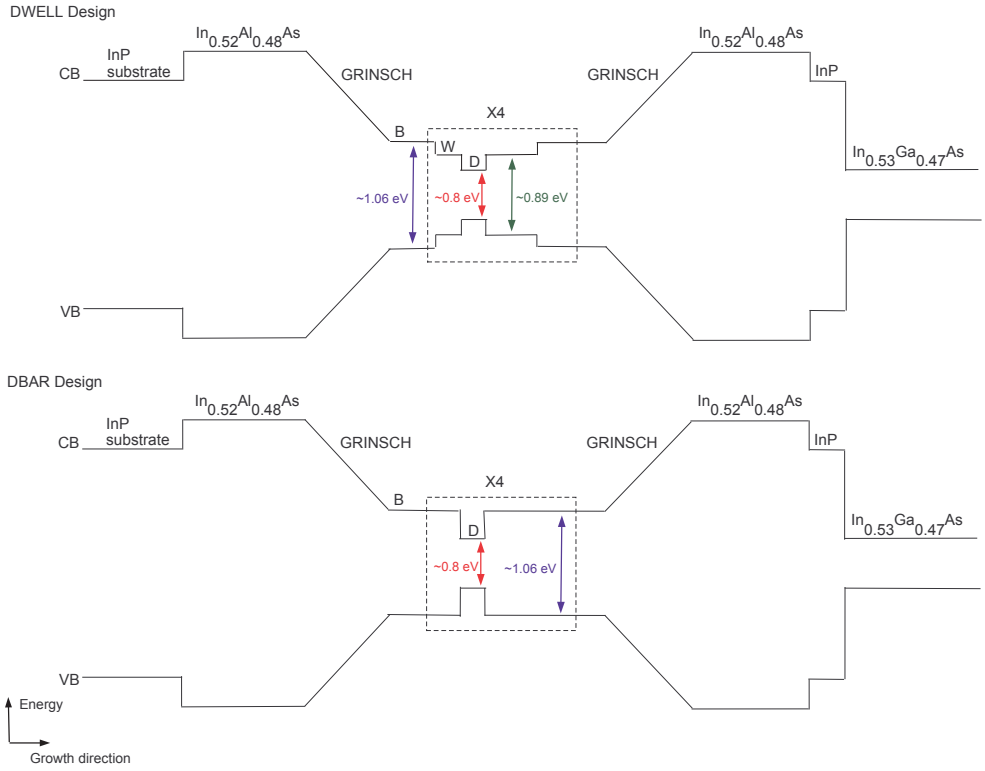

Figure 6.2: Flat band schema of the conduction and valence band profile of the DWELL (top) and DBAR (bottom) design for the aluminium-containing samples, which are made up of four stacks of dashes.

in Fig. 6.2. The Al-DW and Al-DB active regions were embedded into a 400 nm AlGaInAs graded index separate confinement heterostructure (GRINSCH) realised by short period superlattices of InAlAs and InGaAs layers. The GRINSCH is surrounded by 200 nm thick InAlAs cladding layers. The top cladding is capped by InP and InGaAs [110].

The dashes are elongated with the long axis of the dashes orientated along (1-10) and the shorter axis along (110). The dashes have approximate in-plane dimensions of 20 nm x 350 nm along (110) and (1-10) respectively [110].

The materials were processed into ridge waveguide (RW) lasers at the University of Würzburg. All lasers have an optical axis along the (110) crystal axis, as-cleaved facets and are mounted and wire bonded. Al-DW lasers are 600 μm long and have a ridge width of 5 μm. The threshold current density is 1330 $A\ cm^{-2}$ at 293 K. The Al-DB lasers are 800 μm long and have an ridge width of 3.5 μm. Although the Al-DB lasers have reduced mirror losses due to the increased cavity length, the threshold current density at 293 K is 1790 $A\ cm^{-2}$.

6.3 Theoretical Modeling of the Dash Band Structure

Elongated InAs quantum dots, called *quantum dashes*, grow on both (100) oriented AlGaInAs/InP and InGaAsP/InP. The dimensions and orientation of the dashes are similar in both material systems. This section includes a summary of the relevant results of calculations carried out on InAs/AlGaInAs/InP quantum dash material [37, 72, 111]. These will be compared to theoretical results for InAs/InGaAsP/InP quantum dash material presented previously in chapter 4.
We consider two AlGaInAs-based designs, a DWELL design [111] and a DBAR design [37, 72], and compare each one to a similar material design based on InGaAsP. As outlined in chapter 4 the InGaAsP-based DWELL design has a 1.3 nm (001) x 15 nm (110) x 80 nm (1-10) InAs dash embedded in a 6 nm lattice-matched InGaAsP quantum well ($\sim$ 0.855 eV) in a lattice matched InGaAsP barrier ($\sim$ 1.06 eV). In the InGaAsP DBAR design, the InAs dashes have the same in-plane dimensions as the DWELL but are 1.9 nm tall (along (001)). The InAs dashes are confined by a bulk barrier ($\sim$ 1.06 eV). In both InGaAsP-based lasers there are 6 layers of dashes.
In the AlGaInAs DWELL design analysed in Ref [111], the dashes are modeled as a 5 nm (001) x 25 nm (110) x 300 nm (1-10) InAs dash embedded in a 7.5 nm compressively strained AlGaInAs quantum well ($\sim$ 0.952 eV) in an AlGaInAs barrier ($\sim$ 1.052 eV), which is lattice matched to InP. In the DBAR design of Ref [72] the dashes are modeled as a 2.1 nm (001) x 15 nm (110) x 180 nm (1-10) InAs dash embedded in an AlGaInAs barrier ($\sim$ 1.052 eV) lattice-matched to InP. Results have also been calculated using 2.5 nm (001) x 15.6 nm (110) InAs wires embedded in an AlGaInAs barrier lattice matched to InP ($\sim$ 1.052 eV) [37], as it has been demonstrated that AlGaInAs-based quantum DBAR material is wire-like in nature [113]. In the AlGaInAs-based DBAR lasers there are 4 layers of dashes.

6.3.1 Dash Confined State Energies

Considering first the DWELL quantum dash material, results indicate that the electron ground states are confined in the quantum dash in the AlGaInAs-based DWELL material, but that the confinement is poor. The heavy hole valence band ground states are well confined in this material and an energy splitting is predicted between ground state heavy-hole (HH) and light-hole (LH) valence band states [111]. Similar results were presented in chapter 4 for InGaAsP-based DWELL material; however the electron ground state is not confined in the InAs quantum dashes, but rather in the surrounding quantum well layer. Considering

now the aluminium-containing DBAR quantum dash material, calculations indicate that, in the absence of the wetting layer, the electron and hole ground and excited states are confined in the dash [72]. Calculations, which include the effects of the wetting layer and the quantum mechanical coupling between adjacent quantum dashes, indicate that the electron and hole ground states remain well confined [37]. The wetting layer is not found to affect the hole excited states either, but the electron excited states for adjacent dashes become significantly coupled. These results are quite different from those calculated for InAs/InGaAsP/InP DBAR lasers and summarised in chapter 4. In the InGaAsP-based DBAR material many hole states are confined, but only the ground state electron state is confined in the quantum dash. However the confinement is poor for electrons due to the low InAs electron mass and small InAs/InGaAsP conduction band offsets, while the lowest lying HH valence band states are well confined. Results also indicate that the wetting layer can be ignored in InAs/InGaAsP/InP quantum dashes, as it is found not to significantly affect the conduction band states or the dash valence states.

6.4 Experimental Analysis

Having summarised the details of carrier confinement in AlGaInAs-based quantum dash material grown on (100) oriented InP, we now turn to carrying out an experimental analysis of the two types of AlGaInAs-based quantum dash lasers supplied by the University of Würzburg. First, the anisotropy of the optical properties of the quantum dash material is measured using polarized edge-photovoltage (E-PV) and spontaneous emission (SE) spectroscopy. The results of these measurements are provided in sections 6.4.1 and 6.4.2. A comparison is made with the anisotropy of the optical properties presented in chapter 4 for InGaAsP-based quantum dash materials. In section 6.4.3 we analyse the facet and unamplified spontaneous emission collected as a function of current at room temperature for the AlGaInAs-based quantum dash lasers. This analysis suggests that defect-related recombination is dominant in the DWELL sample, while there is a leakage current path in the DBAR. We analyse and quantify these further in sections 6.4.4 and 6.4.5.

6.4.1 Polarized Edge-Photovoltage Spectroscopy

Polarized E-PV spectroscopy and the set up used are described in detail in chapter 3. Linearly polarized light, with energy greater than or equal to the bandgap, incident on the laser facet, is absorbed and the photovoltage generated is measured for $TE_{(1-10)}$ and TM-polarization. The measured polarized E-PV spectra are corrected to remove the polarization-dependence of the spectrometer grating

as outlined in chapter 3. Studying the peaks of the polarized E-PV spectra enables us to identify interband transitions and their character because transitions involving LH states are predominantly TM-polarized.

The spectrally corrected polarized E-PV spectra for the AlGaInAs-based DWELL and DBAR lasers, Al-DW and Al-DB, are shown in Fig. 6.3. In both panels, an energy splitting is observed between the $TE_{(1-10)}$ and TM-polarized spectra. This is in qualitative agreement with results presented in Ref [111]. Comparing Fig. 6.3 to the spectra presented in chapter 4 for InGaAsP-based quantum dash materials, we attribute this energy splitting in InAs/AlGaInAs/InP quantum dash material to the effect of strain.

Considering first the DWELL, theory [111] suggests that the ground state electron and heavy hole states are confined in the dash. In the left panel of Fig. 6.3 we observe two low energy peaks (~ 0.78 eV and ~ 0.81 eV) in the $TE_{(1-10)}$-polarized E-PV spectrum. We are unsure why these two peaks occur but suggest they are due to dash-like electron and hole ground state transitions and may indicate the presence of a bimodal distribution of dashes. We attribute the shoulder at ~ 0.9 eV where the spectra become equal to transitions involving the lattice-matched AlGaInAs quantum well states. More than one peak is also observed in right panel of Fig. 6.3. We again suggest that the peaks are due to confined electron and hole

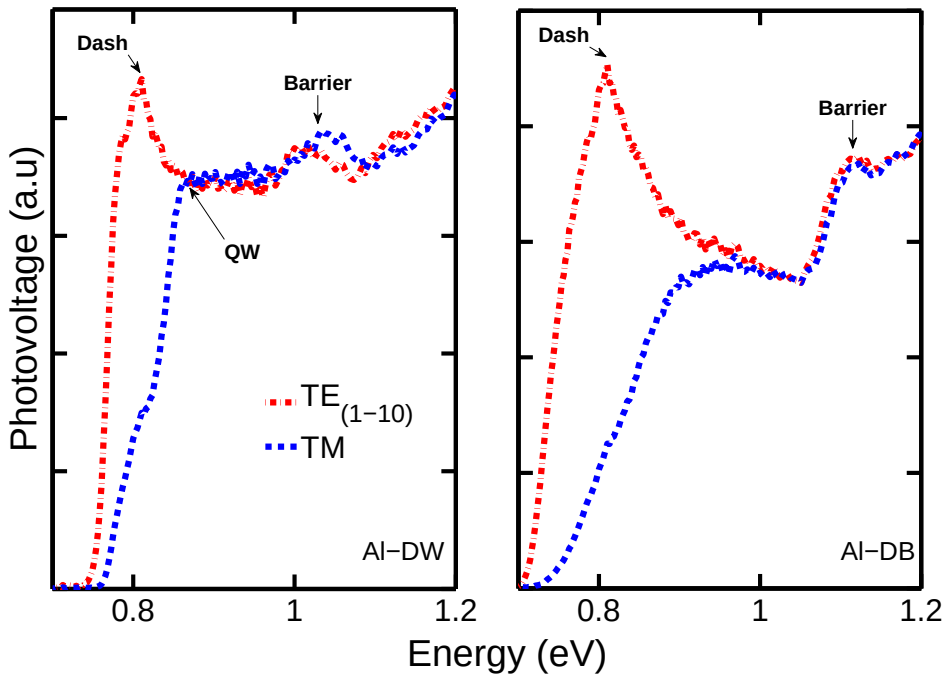

Figure 6.3: Polarized E-PV spectra for Al-DW and Al-DB. The red dash-dot lines show $TE_{(1-10)}$-polarized spectra and the blue dash lines show TM-polarized spectra. Black arrows indicate the approximate energy of peaks corresponding to different transitions.

ground state transitions predicted by theory [37, 72] in a possible trimodal distribution of dashes, as outlined below. We attribute the shoulder at 0.9 eV in Al-DB to transitions involving bound electron states and higher order states of mainly LH character, as in chapter 4, as DWELL theoretical results only include heavy hole states [37, 72]. In both panels of Fig. 6.3 a peak close to 1.1 eV is attributed to barrier transitions. The increase in the E-PV spectra at high energies in both panels is attributed to the graded-index separate-confinement heterostructure (GRINSCH) present in both Al-DW and Al-DB.

Dash Size Dispersion

As outlined in chapter 4 the amount of dash size variation in an ensemble of quantum dashes can be quantified by extracting the standard deviation (σ) of a Gaussian function fitted to the absorption edge of the $TE_{(1-10)}$-polarized E-PV spectrum. As outline above, at least two peaks are measured close to 0.8 eV in the $TE_{(1-10)}$-polarized E-PV spectrum of both Al-DW and Al-DB.
In Al-DW a pair of Gaussians with a standard deviation of $\sim$ 15 meV are required to fit the band edge of the $TE_{(1-10)}$-polarized E-PV spectrum in the top panel of Fig. 6.4. In the bottom panel of Fig. 6.4 three Gaussians with a standard deviation

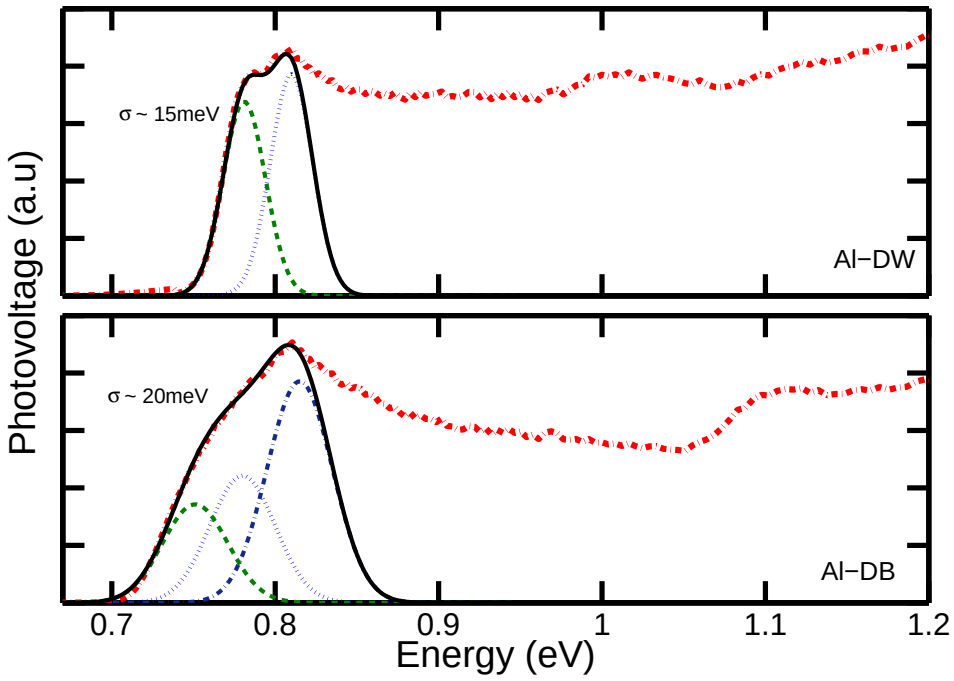

Figure 6.4: The red dash-dot line represents the $TE_{(1-10)}$-polarized E-PV spectrum for Al-DW (top panel) and for Al-DB (bottom panel). The black line is fitted to the absorption edge with a pair of Gaussian functions for Al-DW (top panel), while Al-DB (bottom panel) requires three Gaussian functions for a good fit to the absorption edge.

of $\sim$ 20 meV are required for a good fit of the band edge. The larger value of σ in Al-DB indicates that the same size fluctuations can have a larger effect in the DBAR sample because of the deeper confining potential. Although variations in dash compositions and dimensions lead to inhomogeneous broadening, variations in the dash height are likely to contribute most to this broadening, as both in-plane dash dimensions are significantly larger than the dash height.

6.4.2 Anisotropy of TE Components of SE Spectra

In-plane polarization anisotropy is a beneficial property of quantum dash material [65, 75, 76]. In chapters 2 and 4, we showed that the intrinsic in-plane polarization anisotropy of the material can be quantified by measuring the ratio of the $TE_{(1-10)}$ to $TE_{(110)}$-polarized SE spectra collected through a window in the p-contact. This section includes a study of the $TE_{(1-10)}$ and $TE_{(110)}$-polarized emission spectra measured in the Al-DW and Al-DB structures. The spectra are collected using the set-up outlined in detail in chapter 3.

Considering both panels of Fig. 6.5, we see that $TE_{(1-10)}$-polarized emission is enhanced over $TE_{(110)}$-polarized emission as previously observed for the InGaAsP-based structures in chapter 4. We measure the polarized SE spectra as a function

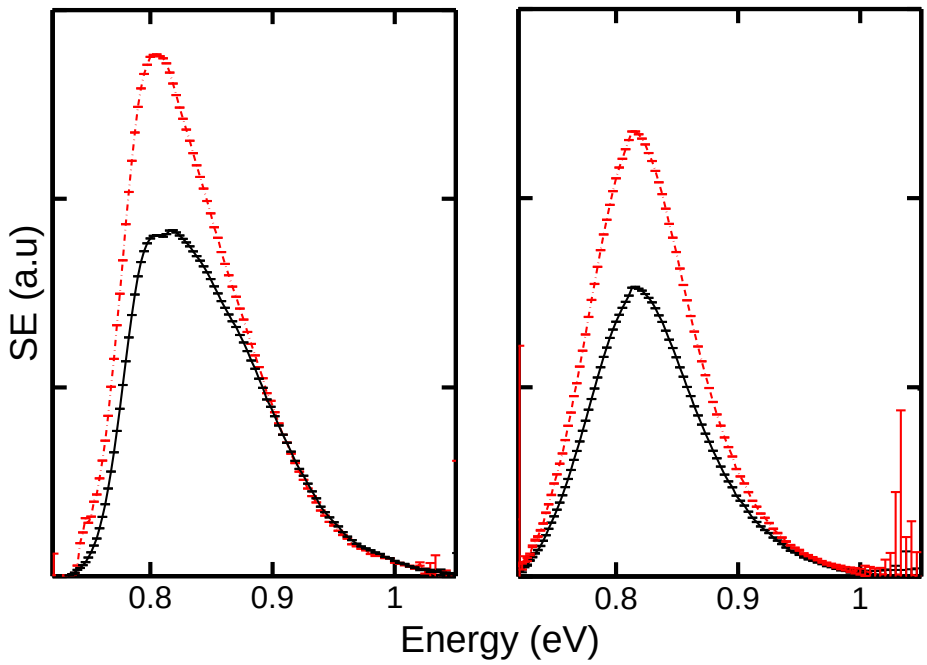

Figure 6.5: The $TE_{(1-10)}$ (red dash-dot) and $TE_{(110)}$ (black) SE spectra for Al-DW (left panel) and Al-DB (right panel), for a drive current of 28.4 mA and 31.5 mA respectively, where both currents are below threshold in the respective laser.

of current and plot the ratio, r, of $TE_{(1-10)}$ to $TE_{(110)}$ polarized SE in the top panels of Fig. 6.6. As r is current-invariant, the ratio is an intrinsic property of the material, as outlined in chapter 4.

The bottom panels of Fig. 6.6 contain the ratios measured in the InGaAsP-based DW1 and DB1 and previously presented in chapter 4. Considering first the DWELL samples in the left column of Fig. 6.5, an anisotropy is measured for energies where transitions involve dash-like states. Both the ratios decrease below 1 at ~ 0.9 eV, above the onset of quantum well and light-hole related transitions. However r in Al-DW decreases from ~ 2 at 0.78 eV to ~ 1.5 at 0.81 eV. This behaviour is not observed in the InGaAsP-based DWELL and is not fully understood. We note that the two energies are consistent with the peak energies of the two peaks identified in section 6.4.1. Considering now the DBAR samples in the right column of Fig. 6.5 we again observe an anisotropy for energies < 0.9 eV. As in the DWELL lasers, the ratio r in Al-DB decreases toward 1 for energies ≥ 0.9 eV. We do not however observe any significant change in r close to the absorption edge in Al-DB, contrary to what was observed in Al-DW. This may be due to the presence of a larger amount of broadening in the Al-DB material. In chapter 4 a larger anisotropy is measured in the DBAR laser and is attributed to a greater carrier confinement. This is also the case in Al-DB, for energies close to 0.8 eV, in

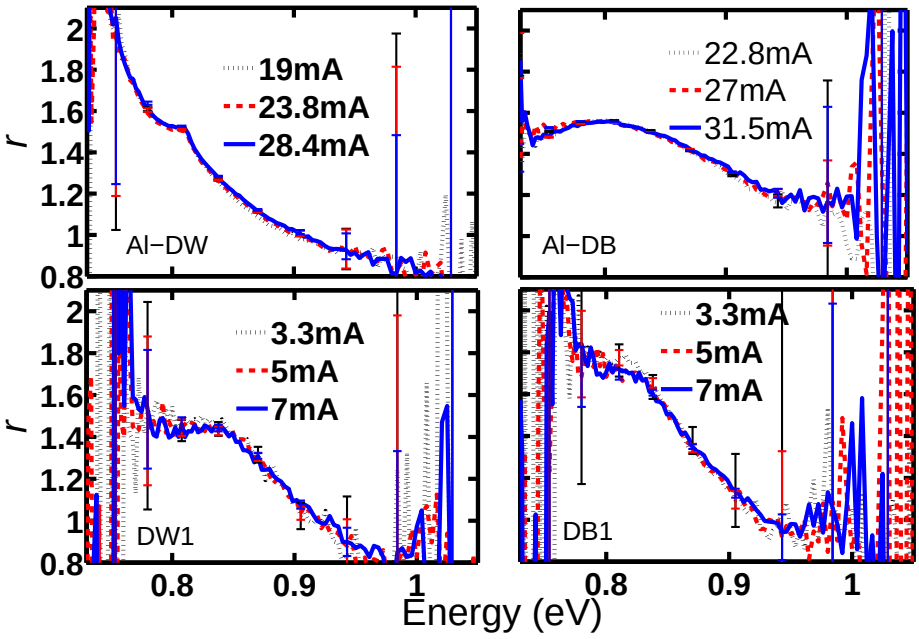

Figure 6.6: Top panels: Ratio r of the $TE_{(1-10)}$ to $TE_{(110)}$ SE spectra for Al-DW (left panel) and Al-DB (right panel) for three values of drive currents. Bottom panels: Ratio of the SE spectra for DW1 (left panel) and DB1 (right panel) for three values of drive currents, as previously presented in chapter 4.

agreement with theory [37, 72, 111], however the enhancement measured in Al-DB is not as large as in the InGaAsP-based DBAR.
In summary we quantified the anisotropy of the in-plane optical properties by measuring polarized SE spectra through a window fabricated into the top contact of each laser. The anisotropy is attributed to a larger momentum matrix element along (1-10) for transitions involving dash-like states, due to the elongation of the dashes along that direction, as previously presented in chapter 4 for InAs/InGaAsP/InP quantum dash materials.

6.4.3 Recombination Processes and Optical Losses

Having established that the polarization characteristics of the AlGaInAs-based quantum dashes are similar to those of InGaAsP-based dashes considered in chapter 4, we turn in this section to investigate the recombination processes present in Al-DW and Al-DB at room temperature (293 K). The main possible carrier recombination processes which can occur in a forward-biased laser are monomolecular defect-related recombination, radiative recombination, Auger recombination, carrier leakage and current spreading, which are explained in detail in chapter 2.
We measure the integrated spontaneous emission, L_{SE}, as a function of current through a window in the top contact of the laser. Recalling that L_{SE} is proportional to the radiative current, we study how the recombination processes change with current up to threshold by comparing the radiative current to the total current at 293 K. Because Al-DW and Al-DB have different cavity length and ridge width, we compare results as a function of current density. As mentioned earlier, it was intended to analyse the devices over a wider temperature range, but this did not prove possible due to device degradation when operated at cryogenic temperatures.

Current Density Dependence of Carrier Recombination Processes at Room Temperature

The analysis presented here involves measuring the variation of the radiative current density, J_{rad}, with total current density, J_{tot}, at room temperature. Assuming $J_{rad} \propto n^2$ and that leakage currents are negligible, the dominant recombination process can be identified by finding the slope, z, of a plot of $ln(J_{tot})$ versus $ln(J_{rad}^{1/2})$. If the device is dominated by defect-related non-radiative recombination, $z \sim 1$, while $z \sim 2$ in a radiatively dominated device, and $z \sim 3$ if non-radiative Auger recombination is dominant. More details can be found about this analysis in chapter 2, as well as in chapters 4 and 5.

In Fig. 6.7, z is plotted at 293 K as a function of the total current density,

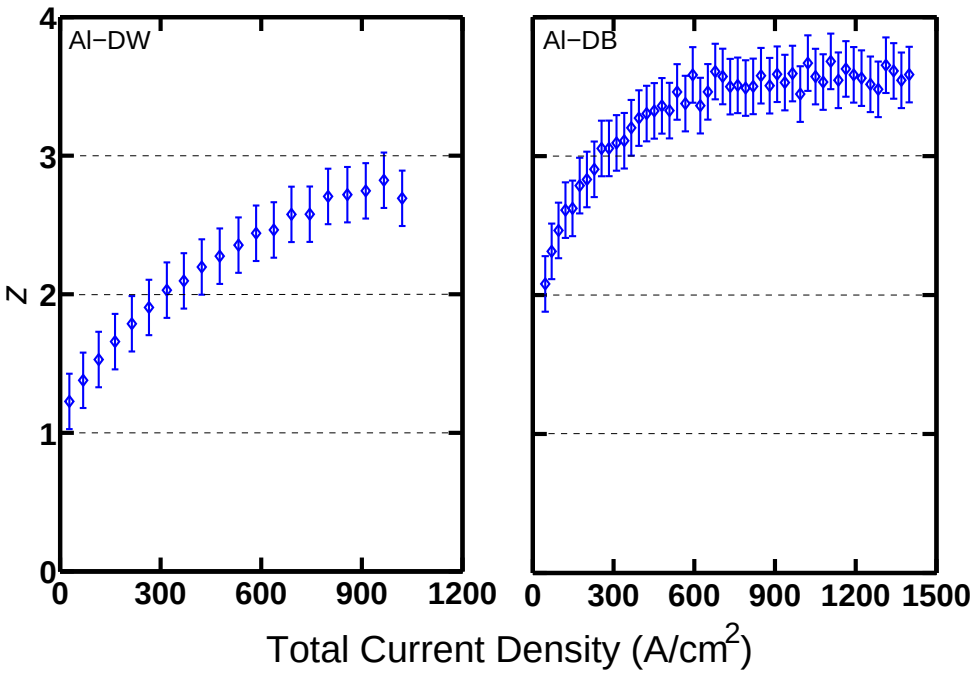

Figure 6.7: Value of the slope, z, of a $ln(J_{tot})$ versus $ln(J_{rad}^{1/2})$ plot, as a function of total current density up to threshold for Al-DW (left panel) and Al-DB (right panel) at 293 K.

J_{total}. In the left panel of Fig. 6.7 Al-DW is seen to suffer from defect-related recombination at low current densities, as $z \sim 1$. Results however suggest that Auger recombination is dominant at threshold where $z \sim 3$. Very different z behaviour is observed in Al-DB in the right panel of Fig. 6.7. At low current densities $z \sim 2$, indicating that Al-DB may be radiatively dominated. As the current density increases, z increases rapidly, reaching ~ 3 at approximately a quarter of the threshold current density, and then rising above 3 at higher currents. We attribute the increase of z above 3 to the presence of another recombination processes, such as current spreading and/or leakage currents. This will be investigated further in section 6.4.5.

To summarise, although we believe Auger recombination is present in both lasers at threshold, the dominant recombination process at room temperature is different for each laser. Results indicate that Al-DW suffers from mono-molecular defect-related recombination but that Auger recombination seems to be dominant close to threshold. Results suggest that another recombination process such as current spreading and/or leakage current is dominant in Al-DB.

6.4.4 Monomolecular Defect-Related Current at Room Temperature

We present here a further analysis of the monomolecular defect-related recombination present in Al-DW, as was done for DB4 in chapter 5. By quantifying the amount of current lost to defect-related recombination in Al-DW, we can get further information on the dominant recombination process at threshold in this laser. The analysis, presented in chapter 5, involves plotting $ln(I_{total})$ versus $ln(L_{SE}^{1/2})$ and fitting a line of slope = 1, which represents the monomolecular defect-related current, $I_{defects}$ ($\propto$ An), to the current range over which it dominates. By extrapolating $I_{defects}$ to threshold we can then estimate the amount of current lost to defect-related recombination at threshold.

Considering the data for Al-DW in the left panel of Fig. 6.8 a good fit between the line of slope = 1 and the experimental data is observed for a wide current range. We estimate that $\sim$ 80% of the threshold current is lost to defect-related recombination, which is therefore the dominant recombination process in Al-DW at threshold. The value of $z_{th} \sim 3$ in Al-DW is attributed to the interplay of dominant monomolecular defect-related recombination and intrinsic Auger recombination. However the large defect-related contribution to the total current means

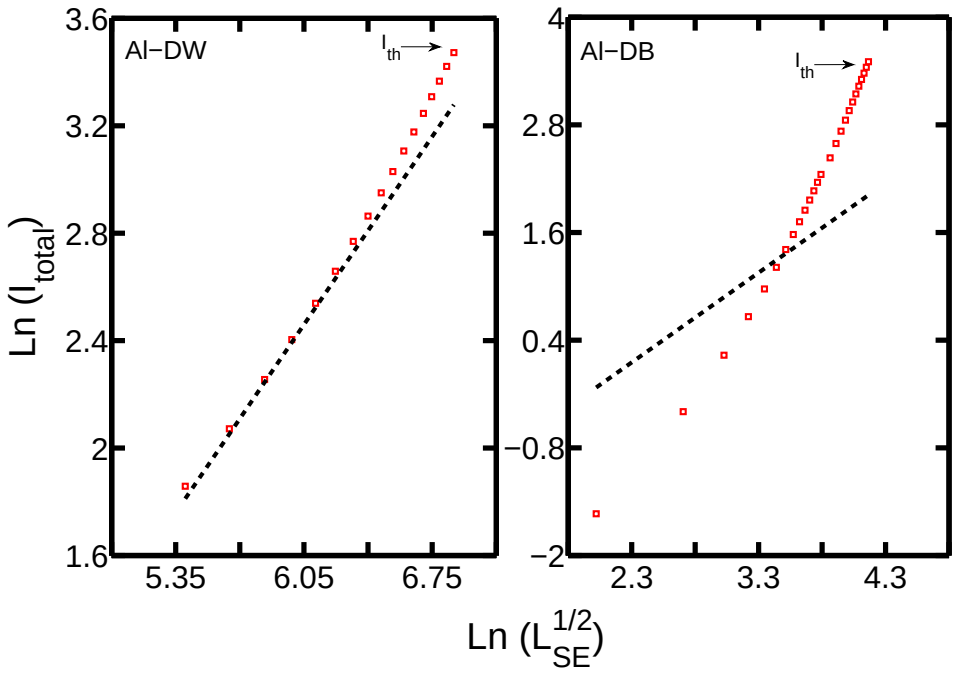

Figure 6.8: Plot of $ln(I_{total})$ versus $ln(L_{SE}^{1/2})$ (open red squares) up to threshold, I_{th} and the black line, with slope = 1, represents the monomolecular defect-related current, $I_{defects}$($\propto$ An) at 293 K for Al-DW (left panel) and Al-DB (right panel)

that it is not possible to identify the relative contributions of Auger and radiative recombination which might be expected in defect-free device.
Applying the same analysis to Al-DB, a poor fit is observed between the line of slope = 1 and the experimental data in the right panel of Fig. 6.8. This result is consistent with the result presented in section 6.4.3, which shows no evidence of defect-related recombination.

6.4.5 Barrier Emission at Room Temperature

In chapter 4 we showed that the external differential quantum efficiency, η_d^{ext}, can be severely affected by the presence of leakage currents. We also observed a correlation between a decrease in η_d^{ext} attributed to leakage currents and $z_{th} > 3$. These results were measured in BH lasers, where current spreading is not an issue. In RW lasers the current spreading and leakage currents play a role in increasing the threshold current density and decreasing the external differential quantum efficiency of the laser [38].
In this section we investigate whether leakage currents are present in Al-DB by measuring SE spectra over a wide spectral and current range. We did not experimentally quantify the current spreading in Al-DW, but expect it may play a role,

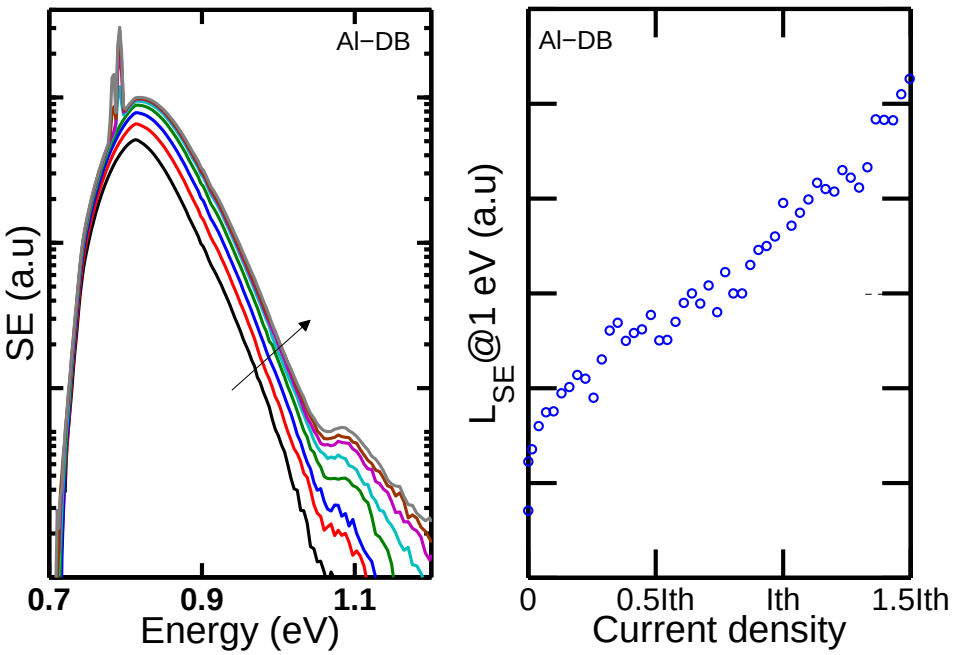

Figure 6.9: Left panel: Unpolarized SE spectra for Al-DB showing barrier emission which does not clamp at threshold. Right panel: Unpolarized, unclamped integrated SE measured at 1 eV in Al-DB. Both indicate the presence of leakage currents.

as we are using 3.5 μm wide ridges. We believe that the presence of current spreading will not change our conclusions and unlike leakage currents, current spreading can be removed by working with BH lasers. We do not investigate Al-DW in this section because it was shown above to be dominated by defect-related recombination.

Considering the left panel of Fig 6.9, barrier emission is observed in Al-DB, which does not clamp at threshold. This can be clearly seen in the right panel of Fig. 6.9, where the SE measured at 1 eV is plotted as a function of current. The results in Fig. 6.9 are consistent with $z > 3$ measured in section 6.4.3, and we therefore suggest that leakage currents are significant in Al-DB. This assignment is also supported by temperature and pressure-dependent measurements [112] on similar samples.

6.5 Summary

This chapter presented an analysis of two InAs/AlGaInAs/InP quantum dash lasers. The differences between InGaAsP and AlGaInAs quantum well material grown on InP were reviewed in section 6.1. We summarised the details of the materials and devices studied in this chapter in section 6.2. Section 6.3 included a summary of the published theoretical results for InAs/AlGaInAs/InP quantum dash-in-a-well and quantum dash-in-a-barrier materials. A comparison was made with results calculated by Dr. Sorcha Healy for InAs/InGaAsP/InP materials and presented in chapter 4.

The experimental analysis was presented in section 6.4. First we studied the anisotropy of the optical characteristics in the Al-containing quantum dash materials. We used polarized edge-photovoltage spectroscopy to confirm the suppression of electron-LH transitions at the band edge. We also collected polarized spontaneous emission spectra to study the anisotropy of the in-plane optical properties, showing that $TE_{(1-10)}$-polarized recombination is enhanced over $TE_{(110)}$-polarized recombination above the band edge, as also observed and analysed for InGaAsP-based quantum dashes in chapter 4.

Having gained an understanding of the band structure and polarization characteristics of AlGaInAs-containing materials, we then studied the recombination process present at room temperature in two AlGaInAs-based quantum dash lasers in section 6.4.3. It did not however prove possible to identify the relative importance of radiative and Auger recombination in these devices compared to InGaAsP-based structures. The analysis shows that Al-DW is dominated by defect-related recom-

bination, while leakage currents make a significant contribution in Al-DB.
Our analysis therefore indicates that the high threshold current density in Al-DW and Al-DB are not due to intrinsic processes. In the absence of defect-related recombination and leakage currents the characteristics of these 1.55 μm InAs/AlGaInAs/InP quantum dash lasers appear to be limited by intrinsic Auger recombination as in AlGaInAs/InP MQW lasers [107], but it did not prove possible with the devices considered here to identify whether AlGaInAs/InP quantum dash lasers provide an advantage compared to AlGaInAs/InP quantum well and/or InGaAsP/InP quantum dash devices.

Chapter 7

Analysis of 1.3μm InAs/GaAs Quantum Dot Lasers

7.1 Introduction

There is a significant interest recently in using GaAs-based quantum dots as the active region in polarization-insensitive semiconductor optical amplifiers (SOA) operating at 1.3 μm [114–117]. Similar work has also been recently reported on 1.5 μm InP-based materials [118–120].

Both undoped and p-doped InAs/GaAs quantum dots have been widely studied [24, 25, 67, 87–89, 95] since quantum dots were first proposed in the early-1980s [4]. However there are differing reports as to the nature of the electronic structure in InAs/GaAs quantum dot materials. Calculations and experimental measurements on single [121, 122] and ensembles [123, 124] of InAs/GaAs quantum dots have suggested optical recombination between ground state electron and hole levels to be purely TE-polarized. These reports are consistent with results for compressively strained quantum wells [53] as well as quantum dashes, presented in chapters 4 and 6, where the heavy hole (HH) and light-hole (LH) valence states are well separated due to the effects of strain. However there have also been experimental reports suggesting the presence of a non-negligible TM-polarized transition close to the main TE-polarized ground state in InAs/GaAs quantum dots [125, 126].

In previous chapters we have studied InP-based quantum dash lasers emitting at 1.5 μm ($\sim$ 0.8 eV), establishing their polarization behaviour and its effect on the overall laser performance. This chapter includes an analysis of the polarization characteristics of undoped and p-doped 1.3 μm ($\sim$ 0.95 eV) InAs/GaAs dot-in-a-well (DWELL) materials. Unlike the InP-based materials studied in the previous chapters, both sets of InAs/GaAs quantum dots studied here are not elongated

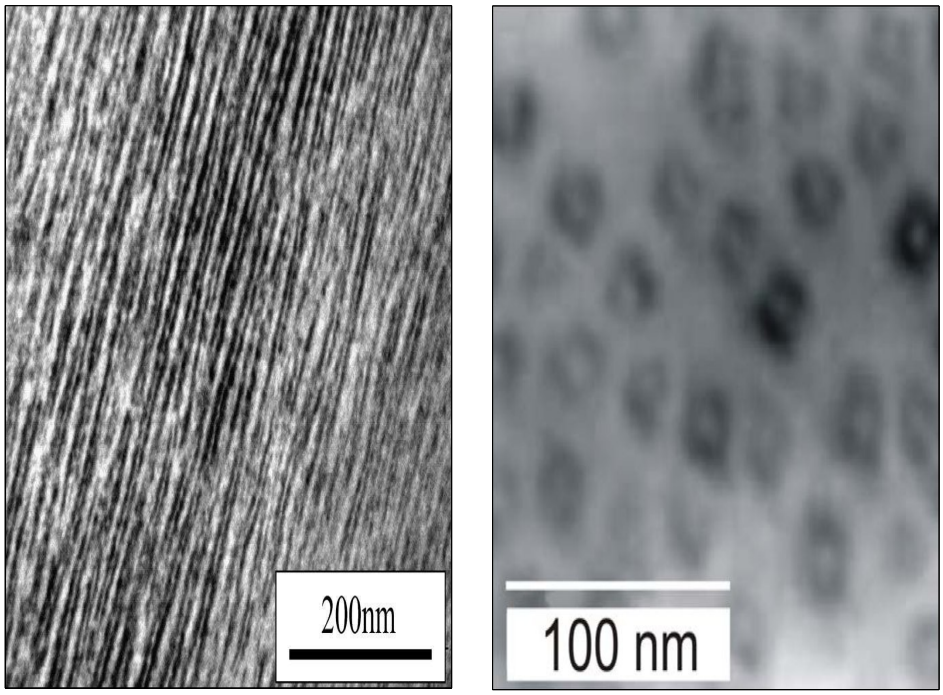

Figure 7.1: The left panel contains a plan-view transmission electron microscopy (TEM) image of a stack of six quantum dash layers similar to those studied in chapter 4 [7], while the right panel contains a plan-view TEM image of a single layer of InAs quantum dots grown in an InGaAs quantum well prior to GaAs deposition [127].

along (1-10), as seen in the left panel of Fig. 7.1 for InAs/InP. Instead InAs/GaAs quantum dots have a shape which is often described as being truncated pyramidal or lens-shaped (right hand panel of Fig. 7.1).

Having given an overview of the samples and materials in section 7.2, the experimental methods are summarised in section 7.3. The first part of the experimental analysis, included in section 7.4, is the room-temperature characterisation of a p-doped InAs/GaAs laser. Results indicate that although this p-doped laser has a temperature sensitive threshold current, its external differential quantum efficiency is almost temperature-insensitive. This sample is TE-polarized above threshold, but both TE and TM-polarized amplified spontaneous emission (ASE) are measured below threshold. In the second part of this analysis, edge-photovoltage (E-PV) spectroscopy is used to confirm the presence of a TM-polarized transition close to, but at an energy above, the TE-polarized ground state transition. An overview of the results of a theoretical analysis, carried out by Mark Crowley, which is relevant to the interpretation of experimental results, is presented in section 7.5.1. Theoretical results indicate that the low energy TM-polarized peak, close in energy to the TE-polarized ground state peak, is due to a transition involving the ground state electron and a low lying excited hole state, which has

predominantly HH character, but with significant LH character with s-like symmetry. A summary of the work presented in this chapter is included in section 7.6.

7.2 Materials and Devices

This section includes an outline of the materials and devices studied in this chapter. Two sets of 1.3μm InAs/GaAs DWELL materials are studied in this work. The material in the first sample, DO520 [128], was grown commercially using molecular beam epitaxy by NL Nanosemiconductor, Dortmund. DO520 is made up of ten stacks of InAs dots (2.5 – 3 monolayers of InAs) in a 5 nm InGaAs well, itself grown in a p-doped GaAs barrier. The dot density is $3 - 5 \times 10^{10}$ cm^2 [128]. The material was processed in Tyndall National Institute into 1200 μm long ridge waveguide (RW) lasers with a ridge width and height of 3 μm and 1.6 μm respectively. This sample will be referred to as NANO.
The second sample investigated in this chapter is a 3 mm long semiconductor optical amplifier (SOA), fabricated commercially by Zia Inc with a cavity angled at 10° to the (110) crystal axis. This SOA, referred to as ZIA, also operates at

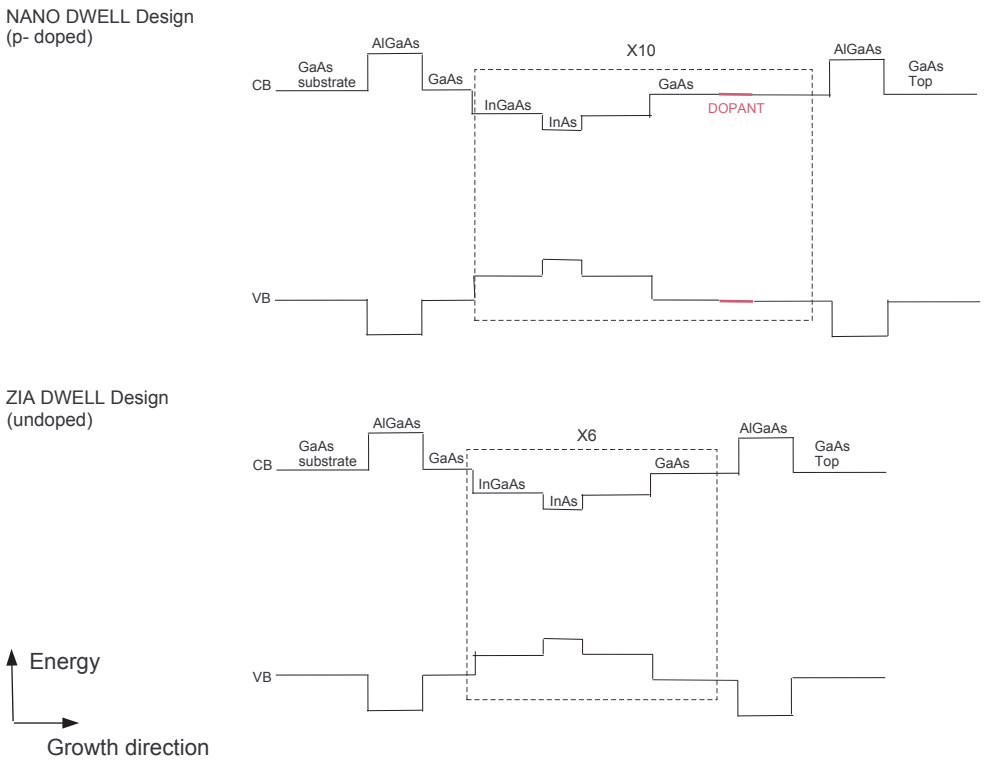

Figure 7.2: Flat band schema of the conduction and valence band profile of the DWELL design of both the modulation doped NANO (top) and undoped ZIA sample (bottom) design, which have ten and six stacks of dots-in-a-well respectively.

1.3 μm and has a 4 μm width ridge and antireflection coated facets [129]. As in chapter 4, the SOAs are only used for material property measurements in this chapter. The active region is made up of six stacks of InAs quantum dots grown on an InGaAs well, with a GaAs barrier. This sample is not modulation doped. A schematic flat band profile for the NANO and ZIA DWELL designs can be seen in Fig. 7.2.

7.3 Overview of the Experimental Methods

This section includes an overview of the experimental set up used to characterise the p-doped InAs/GaAs 1.3 μm NANO laser sample, as well as the set up used to measure the polarized edge-photovoltage (E-PV) spectra for the NANO and ZIA DWELL materials.

We used a calibrated broad area detector from an Ando AQ2140 powermeter to measure the temperature dependence of the integrated facet emission for the NANO laser close to 300 K. The temperature was varied using a Peltier-element and a temperature sensor connected to a temperature controller. An optical spectrum analyser (OSA) was then used to collected polarized amplified spontaneous emission (ASE) spectra with an 0.01 nm or an 0.5 nm resolution at 298 K. The set up can be seen in Fig. 7.3, where an isolator was used to ensure that there was no

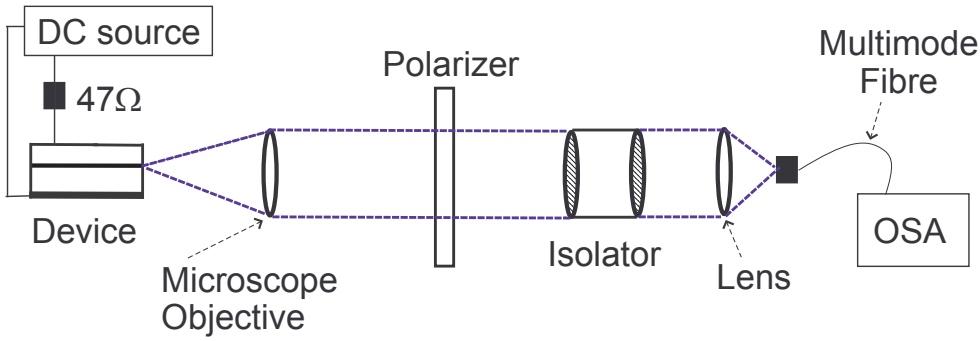

Figure 7.3: Schema of the experimental set up used to collect ASE spectra as a function of current at 298 K.

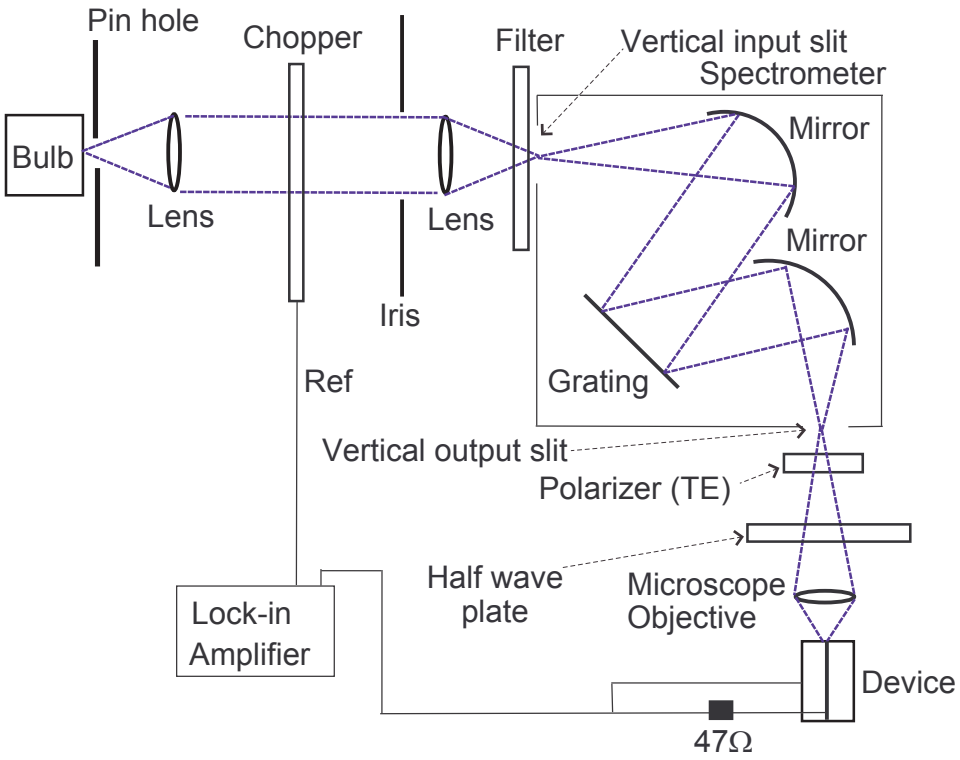

Figure 7.4: Schema of the set up used to measure polarized E-PV spectra at room temperature in the GaAs-based devices.

feedback from the external cavity. In our case the OSA model used was an Ando AQ6317.

In order to measure polarized edge-photovoltage (E-PV) spectra in these GaAs-based devices, we modified the set up described in detail in chapter 3 and included a half wave plate (HWP). A HWP is used to rotate the plane of polarization from a known linear polarization to any other desired plane. By setting the polarizer in the set up in Fig. 7.4 to the TE-polarization orientation and changing the fast axis of the HWP from 0 ° to 45 ° to the TE-polarization axis, the light incident on the facet of the laser can be changed from TE-polarized to TM-polarized. This enabled us to measure pairs of polarized E-PV spectra in a single sample orientation, which do not require any spectral correction other than the system response. In this part of the work we were interested in the ratio between TE and TM-polarized photovoltage. Extra care was taken to ensure that the polarizer in the set up had as high an extinction ratio as possible. A number of polarizers were tested, but best results were obtained with a single linear polarizer, with an extinction ratio of 0.15 %, which was also used in chapters 4 and 6.

7.4 Room Temperature Characterisation of a P-Doped InAs/GaAs 1.3μm Laser.

This section includes the results of the characterisation of the p-doped InAs/GaAs 1.3 μm NANO laser. Measurements were undertaken to establish that the general laser characteristics were comparable to other devices reported in the literature. We measure the light-current characteristics as a function of temperature from 293 – 323 K, from which we extract the characteristic temperature, T_0, defined in chapter 2. We then measure TE and TM-polarized ASE spectra as a function of current at 298 K and extract the net modal gain spectra by using the Hakki-Paoli technique [58].

7.4.1 Temperature Dependence of Light-Current Characteristics.

In order to characterise the p-doped NANO laser, we begin by measuring the integrated facet emission as a function of temperature from 293 – 323 K and plotting it in Fig. 7.5. The facet emission above threshold is found to be TE-polarized and the characteristic temperature, $T_0 \sim 60$ K, is lower than values measured over this temperature range on other p-doped GaAs-based lasers ($T_0 \geq 196$ K) [86, 89]. As

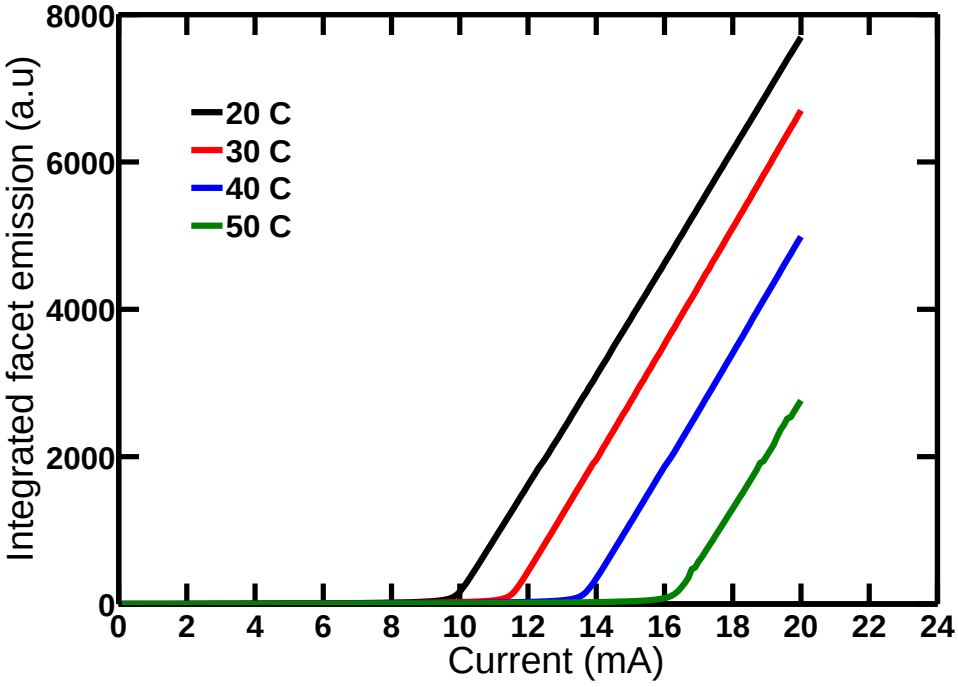

Figure 7.5: Measured temperature dependence of the threshold current for the NANO laser.

the coupling efficiency was unchanged with temperature in the measurement, we are able to consider the temperature dependence of the external differential quantum efficiency, η_d^{ext}. We find that η_d^{ext} is almost temperature independent between 293 K and 323 K, as previously observed by Fathpour *et al.* [89].

7.4.2 TE and TM-Polarized Amplified Spontaneous Emission Spectra.

We began by considering the TE-polarized ASE spectra above and below threshold at 298 K, where the threshold current was measured to be $\sim$ 11 mA. We then turned to consider the TM-polarized ASE. Plotted on a log scale in the left panel of Fig. 7.6 are TE and TM-polarized ASE spectra measured at 8.5mA with a resolution of 0.01 nm. A close up of these spectra showing the Fabry-Pérot resonances is included in the left panel of Fig. 7.6. Considering the TE-polarized ASE spectrum plotted in red we observed a single peak, which we attribute to the ground state transition. We then extracted the net modal gain spectra as a function of current from the TE-polarized ASE spectra using the Hakki-Paoli method [58]. With this approach the contrast ratio, ρ, of the Fabry-Pérot resonances of the cavity of length, L, and mirror reflectivity, R, is used to extract the net modal

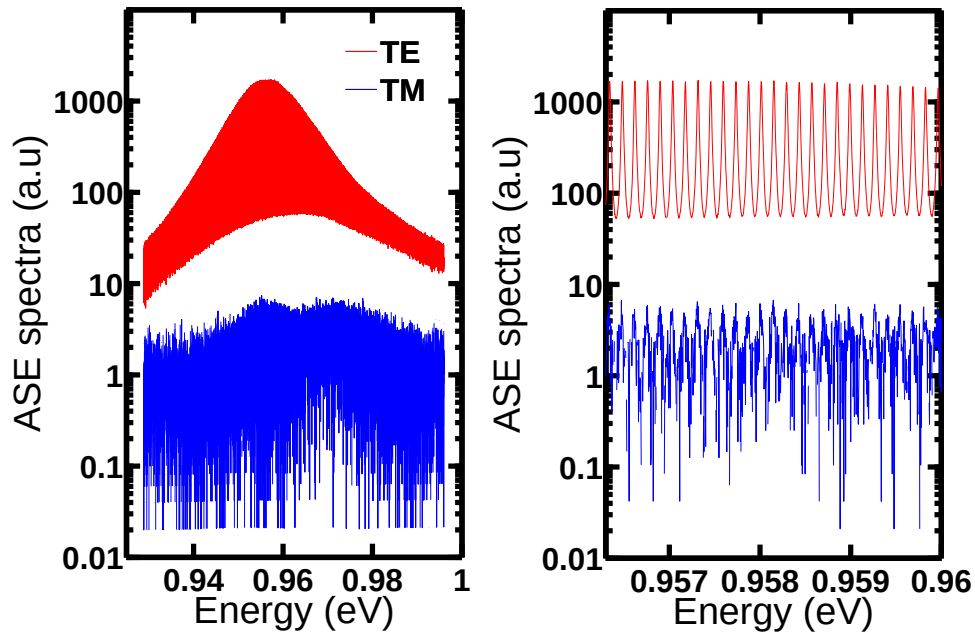

Figure 7.6: TE and TM-polarized ASE spectra measured with an 0.01 nm resolution at 8.5 mA in the left panel, with a close up of the Fabry-Pérot resonances in the right panel, plotted on a log scale.

gain spectrum from the sub – threshold ASE spectrum using

$$\Gamma g - \alpha_i = \frac{1}{L} ln\left(\frac{1}{R}\right) - \frac{1}{L} ln\left(\frac{\sqrt{\rho}+1}{\sqrt{\rho}-1}\right) \tag{7.1}$$

where $\Gamma g - \alpha_i$ is the net modal gain. The TE-polarized net modal gain spectra are plotted in Fig. 7.7. The Hakki-Paoli analysis is only valid below threshold; as evidenced by the gain clamping at 11 mA. A net modal gain spectrum converges to α_i for photon energies below the band edge. Considering the low energy tail of the net modal gain spectra in Fig. 7.7 this p-doped laser appears to have very low internal losses. Turning to the TM-polarized ASE spectra, which we also measured with a 0.01 nm resolution above and below threshold at 298 K. As the coupling was unchanged, we can plot the TM-polarized ASE spectra measured at 8.5 mA on a log scale in Fig. 7.6 along with the corresponding TE-polarized spectra. There is much less TM-polarized than TE-polarized emission and the spectra are quite different, unlike what has been reported in Ref [123].
We observed two bumps in TM-polarized ASE spectra. This can be seen more clearly in Fig. 7.8, where the resolution of the TM-polarized spectra was reduced from 0.01 nm to 0.5 nm. We attribute the higher energy peak at $\sim$ 0.975 eV to true TM-polarized emission, while the lower energy peak, just below 0.96 eV, which increases more rapidly and lases above threshold, is attributed to scattered

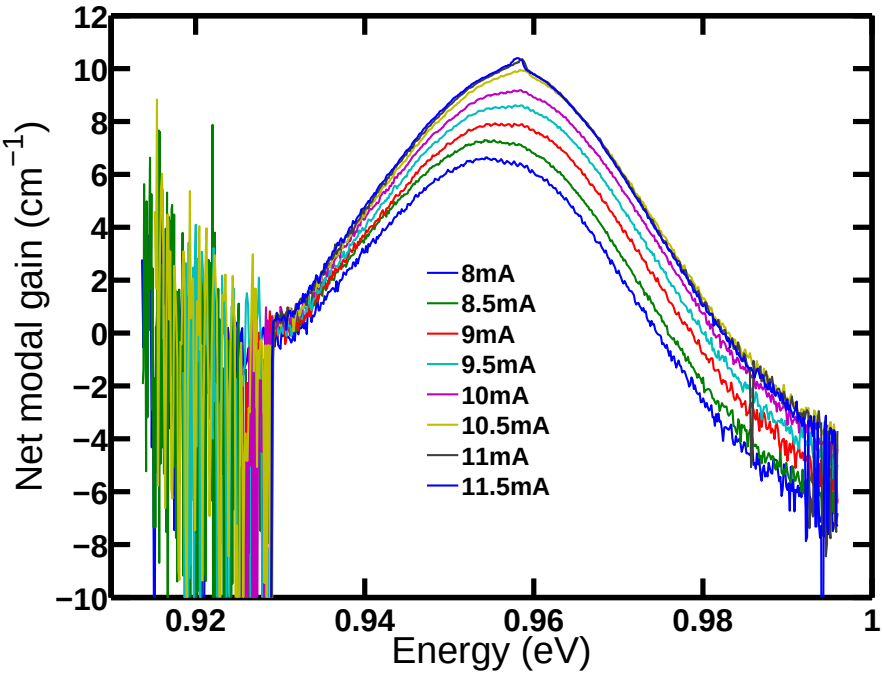

Figure 7.7: TE-polarized net modal gain spectra for the NANO laser.

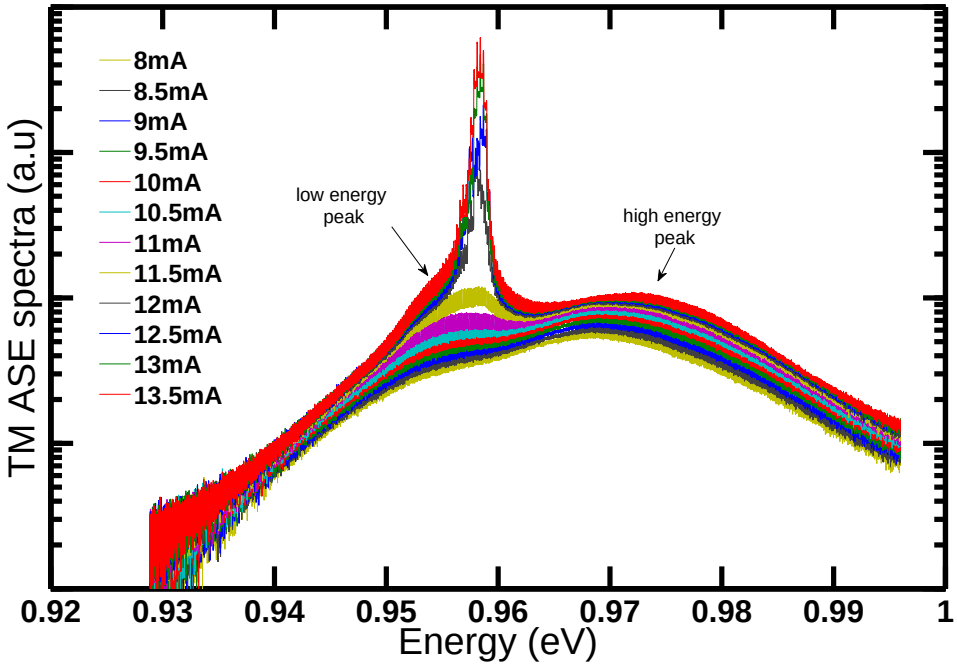

Figure 7.8: TM-polarized ASE for a 0.5 nm resolution. The peak at $\sim$ 0.975 eV is attributed to true TM-polarized peak, while we attribute the lower energy peak just below 0.96 eV to scattered TE-polarized emission.

TE-polarized ASE. The 0.01 nm resolution TM-polarized ASE spectra, similar to that plotted in Fig. 7.6, were too noisy to extract the TM-polarized net modal gain. Nevertheless we see that there is TM-polarized emission associated with recombination under the ground state peak, in agreement with Refs [125, 126] but contrary to other experimental reports [123, 124].

In summary we investigated the characteristics of a p-doped 1.3μm InAs/GaAs DWELL laser at room temperature by analysing the ASE. We first considered the integrated facet emission as a function of temperature, before considering the TE-polarized ASE spectra, from which we extracted the TE-polarized net modal gain. We also measured TM-polarized ASE, which indicates that there may be a TM-polarized transition close to, but at a slightly higher energy than the main TE-polarized ground state transition. In the following section, we use polarized edge-photovoltage (E-PV) spectroscopy to determine the energy distribution and character of transitions in the p-doped and undoped InAs/GaAs quantum dot materials.

7.5 Polarized E-PV Spectroscopy

Having identified a TM-polarized transition close to the TE-polarized ground state in the ASE spectrum of the p-doped NANO sample, we investigate this transition further in this section, as well as considering the undoped 1.3μm InAs/GaAs DWELL material, which makes up the active region in the ZIA SOA. We used the set up outlined in section 7.3 to measure polarized E-PV spectra. As outlined in chapter 3, a peak in a TE-polarized E-PV spectrum is typically due to transitions between electrons and HH states, while peaks in TM-polarized E-PV spectra are predominantly due to transitions involving electrons and LH states [50, 52].
The E-PV spectra measured in the NANO and ZIA samples are shown in the left and middle panels of Fig. 7.9. There is a striking similarity between them, indicating the negligible effect of the p-dopant on transition energies in the modulation-doped material. The arrows in Fig. 7.9 indicate the approximate energy of the peaks corresponding to different transitions. The lowest TE-polarized peak in the E-PV spectra is at an energy greater than the TE-polarized ASE peak in Fig. 7.7, because the bandgap narrows when the device is electrically pumped.

The polarized E-PV spectra measured in InAs/GaAs quantum dots are different from those measured in strained quantum well material [53] and quantum dash material, presented in chapters 4 and 6, where TM-polarized transitions are strongly suppressed at the band edge. Both TM-polarized E-PV spectra in Fig. 7.9 reveal the existence of a transition close to, but not at, the TE-polarized ground state dot transition. This TM-polarized peak is $\sim 20-30\%$ of the TE-polarized ground state peak, similar to the value reported in Ref [126] and is labelled in green as A in Fig. 7.9. We believe this is the first report of a TM-polarized peak in E-PV spectra measured in dot-in-a-well material, although similar behaviour has been reported for dot-in-a-barrier materials. Refs [125, 126, 130] report a rising background of TM-polarized absorption starting under the ground state peak. Ref [125] does not quantify or explain it, while Ref [126] quantifies the TM-polarized E-PV component at $\sim 25\%$ of the TE-polarized peak. Chu et al [130] show a plot where TM-polarized absorption is absent and another where it is present and in the latter case, attribute it to vertical coupling between quantum dots.
In the following section we investigate the origin of the peak labeled as A in the E-PV spectra in Fig. 7.9 by considering the results of a theoretical analysis undertaken by Mark Crowley.

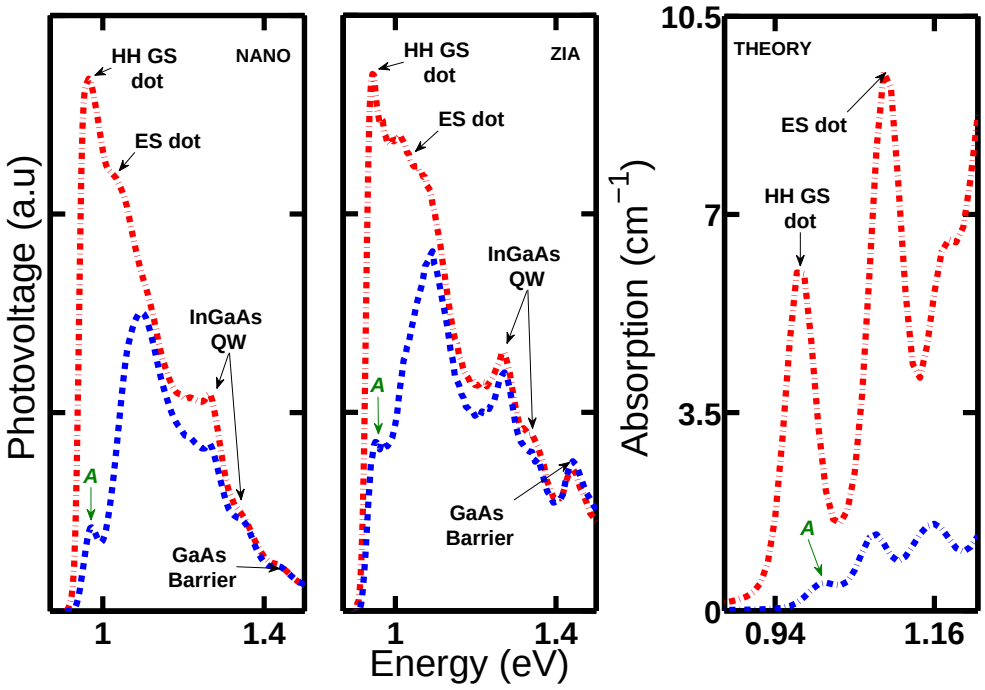

Figure 7.9: Left and middle panels: Polarized E-PV spectra for NANO laser and ZIA SOA measured using a x 25 and a x 40 microscope objective respectively. Right panel: Calculated absorption spectra for a 1.3μm DWELL material. The red dash-dot lines show TE-polarized spectra, the blue dash lines show TM-polarized spectra. The non-negligible low energy TM-polarized peak is labeled as A.

7.5.1 Origin of the Low Energy TM-Polarized Transition

This section includes a summary of the relevant theoretical results of calculations carried out by Mark Crowley on an InAs/GaAs DWELL structure similar to the undoped ZIA sample. These results will be used to understand the origin of the TM-polarized transition close to the main TE-polarized ground state transition. Calculations are performed on a square based truncated pyramidal shaped InAs dot with a base and top length of 15 nm and 11.25 nm. The dots are 5 nm high and sit on a one monolayer (0.28 nm) thick wetting layer. The dots are capped with a 5 nm thick $In_{0.15}Ga_{0.85}As$ quantum well in a GaAs barrier.

We compare the measured polarized E-PV spectra in the left and middle panels of Fig. 7.9 to the calculated absorption curves plotted in the right most panel of Fig. 7.9. The calculated absorption spectra include an inhomogeneous broadening of 30 meV to account for the dot size dispersion in a real quantum dot ensemble. This value is about twice the measured value obtained by fitting a Gaussian function to the absorption edge of the E-PV spectra. A non-negligible peak, labeled as A, can be seen in the calculated TM-polarized absorption spectrum at an energy close to the main TE-polarized ground state, in agreement with the measured

E-PV spectra.

A top view of the calculated spatial probability density component isosurface for

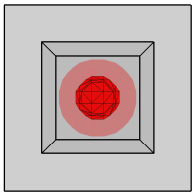

(a) E_1

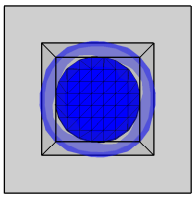

(b) HH part of H_1

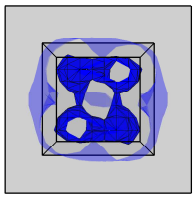

(c) LH part of H_1

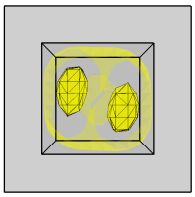

(d) HH part of H_2

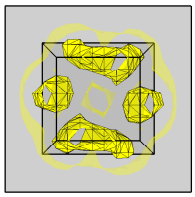

(e) LH part of H_2

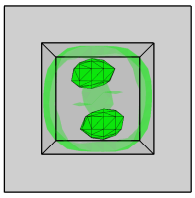

(f) HH part of H_3

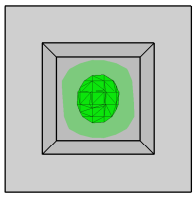

(g) LH part of H_3

Figure 7.10: Top view of the square based truncated pyramidal shaped InAs dot and the calculated spatial probability density component isosurfaces for (a) the electron ground state, E_1, and (b) – (g) the HH (left column) and LH (right column) components of the ground state hole, H_1, in blue and two lowest lying excited state hole, H_2 (in yellow) and H_3 (in green) in DWELL.

the ground state electron, E_1, is plotted in Fig. 7.10(a). The HH spatial probability density component isosurfaces for the ground state hole, H_1, and two lowest lying excited hole states, H_2 and H_3, are plotted in blue, yellow and green respectively in the left column of Fig. 7.5.1, while the corresponding LH spatial probability density component isosurfaces are plotted in the right column. Considering first the ground state transition ($E_1 \rightarrow H_1$), we can see that there is a strong spatial overlap between the spatial probability density component isosurface of E_1, plotted in Fig. 7.10(a), and the HH part of the ground state hole plotted in Fig. 7.10(b), as both have s-like symmetry. However there is no interaction between E_1 and the LH part of the ground state hole, plotted in Fig. 7.10(c), which has p-like symmetry. Hence H_1 does not contribute to the TM-polarized recombination with the ground state electron. As both the HH and LH spatial probability density component isosurfaces of H_2 in Fig. 7.10(d) and Fig. 7.10(e) respectively, have p-like symmetry, there is also negligible interaction between these and the ground state electron, E_1. By contrast the LH part of H_3, included in Fig. 7.10(g), has s-like symmetry and makes up a significant part of the second lowest lying excited hole state (15.3 % for the dot dimensions modelled here). Theoretical results suggest that the TM-polarized transition, labelled as A in Fig. 7.9, is due to a strong spatial overlap between the ground state electron, E_1, and the LH part of the second lowest lying excited hole state, H_3, which both have s-like symmetry.

To summarise, polarized E-PV spectroscopy is used to study and differentiate transitions involving electrons and HH states from transitions involving LH states. Experimental results confirm the presence of a TM-polarized transition at an energy close to, but slightly above, the TE-polarized ground state. These results are in good agreement with the calculated absorption spectra included in the right panel of Fig. 7.9. The theoretical results, summarised in section 7.5.1, indicate that the low energy TM-polarized transition involves ground state electrons and the LH component of the second lowest lying excited state holes, H_3. As both have s-like symmetry, there is a strong spatial overlap leading to a non-negligible TM-polarized transition at an energy close to the main TE-polarized ground state transition.

7.6 Summary

This chapter has presented an analysis of InAs/GaAs 1.3μm DWELL devices. Section 7.2 includes an overview of the materials and devices studied in this chapter, with an overview of the experimental methods in section 7.3. Having characterised a p-doped InAs/GaAs 1.3μm DWELL laser at room temperature, we investigated

the TE-polarized ASE spectra and extracted the TE-polarized net modal gain. We then measured the TM-polarized ASE spectra and identified two peaks. We attribute the higher energy peak to the true TM-polarized transition. We then use polarized E-PV spectroscopy to further investigate the energy distribution and nature of the energy states in the p-doped as well as in an undoped 1.3μm InAs/GaAs DWELL material in section 7.5. The transitions are very similar in the undoped and p-doped sample, indicating that the modulation doping has a negligible effect on the transition energies. Analysing the E-PV spectra we identified an electron-LH transition close to the main TE-polarized ground state, consistent with the measured TM-polarized ASE spectra in section 7.4. Although the TM-polarized ground state has been previously measured, it has never been satisfactorily explained. We gained an understanding of the origin of the TM-polarized ground state peak measured in the undoped and p-doped 1.3μm DWELL materials by considering results calculated by Mark Crowley in section 7.5.1. The theory indicates that the measured TM-polarized transition, with an energy close to the main TE-polarized ground state, is due to the strong spatial overlap between the ground state electron and the LH component of the second lowest lying excited hole state. Experimental results are in very good agreement with theory and help confirm the overall trend observed in Mark Crowley's further calculations which suggest that the TM-polarized transition is quashed as the quantum dot height to base ratio decreases.

Chapter 8

Summary

8.1 Conclusions

This thesis has been concerned with investigating gain and loss mechanisms in 1.3 μm and 1.5 μm semiconductor quantum dot lasers. Chapters 4 and 5 provided an analysis of undoped and p-doped InAs/InGaAsP/ InP quantum dash lasers emitting at 1.5 μm. This was followed in chapter 6 by a study of 1.5 μm InAs/AlGaInAs/InP quantum dash lasers. In chapter 7 we analysed the polarization characteristics of 1.3 μm InAs/GaAs quantum dots lasers. In the following sub-sections we summarise the achievements of each topic, and conclude with a brief summary of future directions in section 8.2.

8.1.1 Analysis of InAs/InGaAsP/InP Quantum Dash Lasers

In chapter 4 we presented a combined theoretical and experimental analysis of InAs/InGaAsP/InP quantum dash structures.

We began with a summary of the relevant theoretical results of 8 band k.p calculations carried out by Dr. Sorcha Healy. The theoretical results indicate that because of the low electron mass and small conduction band offsets, the electron states in the dash-in-a-well material are confined within the quantum well and are only weakly confined in the dash in the dash-in-a-barrier structure. The shape of the dashes, as well as strain, led to a predicted enhancement in the optical recombination rate for light polarized along the dash long axis. Strain also led to strongly reduced TM-polarized emission at the band edge, as is found in compressively strained quantum well lasers [53].

The anisotropy in the optical characteristics, which is a beneficial property of the dash structure [65], was confirmed experimentally. We first used polarized edge-photovoltage spectroscopy to confirm the suppression of TM-related recom-

bination at the band edge, and then measured polarized spontaneous emission spectra through a window in the top contact of the laser to confirm the anisotropy in the growth plane. The measured E-PV spectra and spontaneous emission enhancement were in excellent agreement with the theoretical calculations.
We then investigated the measured dependence of the integrated spontaneous emission rate to the total current as a function of temperature in order to identify the recombination processes present in InAs/InGaAsP/InP quantum dash lasers. Our results showed that Auger recombination remained the dominant intrinsic carrier recombination process in these lasers, as previously shown for 1.55 μm quantum well lasers [39]. We also identified a correlation in one device between the onset of current leakage paths and a reduction in the external differential quantum efficiency.
Despite these limitations InAs/InGaAsP/InP dash lasers have the benefit of having anisotropic optical properties, of interest in edge and surface emitting lasers [65, 75, 76], as well as having improved temperature performance compared to conventional InGaAsP/InP quantum well and (311)B quantum dot [39, 78] lasers.

8.1.2 Recombination Processes in P-Doped Quantum Dash Lasers

Having established in chapter 4 the intrinsic characteristics of undoped InAs/ InGaAsP/InP dash structures, we then turned in chapter 5 to undertake an analysis of two p-doped InAs/InGaAsP/InP lasers.
We found that care had to be taken when using the measured variation of the integrated spontaneous emission with total current analysis to identify the dominant carrier recombination process in p-doped lasers. This was due to the high density of acceptors in the active region, which at very low temperatures played a dominant role at threshold. The acceptors had a less pronounced effect on the analysis with increasing temperature, allowing a reasonable analysis of the recombination mechanisms at room temperature. Auger recombination was identified as the dominant intrinsic process at room temperature in these lasers.

8.1.3 Analysis of InAs/AlGaInAs/InP Quantum Dash Lasers

It has been shown that the improved electron confinement in AlGaInAs/InP quantum wells leads to a reduced temperature dependence of the threshold current compared to InGaAsP-containing quantum well lasers. There is therefore an interest in growing quantum dots on AlGaInAs-containing materials. The aim of the analysis in chapter 6 was to compare the characteristics of InAs/AlGaInAs/InP quantum

dash lasers to the lasers studied in chapter 4. However the InAs/AlGaInAs/InP quantum dash laser samples available degraded rapidly when low temperature measurements were carried out. Therefore the analysis was only carried out at room temperature.
The characteristics of the 1.55 μm InAs/AlGaInAs/InP quantum dash lasers appeared to be limited by intrinsic Auger recombination as in AlGaInAs/InP multi quantum well lasers [107], in the absence of defect-related recombination and leakage currents. However, because only room temperature data was available, it did not prove possible to identify whether AlGaInAs/InP quantum dash lasers had beneficial properties over AlGaInAs/InP quantum well and/or InGaAsP/InP quantum dash lasers.

8.1.4 Analysis of 1.3 μm InAs/GaAs Quantum Dot Lasers

Chapter 7 presented a study of the polarization characteristics of undoped and p-doped 1.3 μm InAs/GaAs quantum dot materials and devices.
We began by considering the characteristics of a p-doped laser between 293 K and 323 K. We then measured the TE-polarized amplified spontaneous emission (ASE), from which we extracted the net modal gain using the Hakki-Paoli technique [58]. We also measured the weaker TM-polarized ASE, which had a peak at a slightly higher energy than the TE-polarized ASE peak.
To determine the energy distribution and character of the interband transitions and to confirm the presence of a TM-transition close to the TE-polarized ground state peak, we measured polarized E-PV spectra in the p-doped laser, as well as in an undoped InAs/GaAs quantum dot device. Our results showed the presence of a TM-polarized transition close in energy to the main TE-polarized ground state transition. We gained an understanding of the origin of the measured low-energy TM-polarized transition by reviewing the relevant theoretical results of 8 band k.p calculations carried out by Mark Crowley. These results show that low lying excited hole states, with both a non-negligible LH character and strong spatial overlap with the ground state electron, are responsible for the TM-polarized transition with an energy close to, but slightly above, the main TE-polarized ground state.

8.2 Future Work

In summary we have investigated in this thesis gain and loss mechanisms in 1.5 μm and 1.3 μm semiconductor quantum dash and dot lasers, including an analysis of

the polarization characteristics of the different devices.

We were able to undertake a detailed analysis of 1.5 μm undoped and p-doped InAs/InGaAsP/InP quantum dash lasers. This analysis helped in the development of a new generation of InAs/InGaAsP/InP quantum dash lasers with improved temperature stability ($T_0 \approx 95$ K), which have recently been grown and processed by Alcatel – Thales III – V Lab. It would be interesting to investigate these new lasers further to analyse the different factors contributing to the improvement.

Having studied first generation InAs/AlGaInAs/InP quantum dash lasers in chapter 6, it would also be of interest to study the temperature dependence of the threshold current and its radiative component for a new generation of InAs/AlGaInAs/InP quantum dash lasers. AlGaInAs/InP quantum well lasers show improved performance over InGaAsP-based quantum well lasers, due to improved electron confinement, and one would expect this to be the case also in InAs/AlGaInAs/InP quantum dash lasers when only intrinsic recombination processes are present. Coupling this analysis with other analyses (TEM, AFM) would also allow us to confirm whether there is a bimodal or trimodal dash distribution, as suggested by the measurements in chapter 6.

It would also be interesting to apply the analysis methods presented here to other anisotropic materials, including GaInP quantum wells and GaN quantum dots grown on non-polar substrates, as well as to self-assembled Sb- and N-containing quantum dots. If site-controlled quantum dots and nano-pillars grown on pre-patterned Si and GaAs substrates are electrically pumped, it would also be of interest to study the optical properties of these materials and their polarization dependence.

There has been an interest in recent times in using InAs/GaAs quantum dot materials in the development of polarization insensitive semiconductor optical amplifiers. It would be valuable to carry out a systematic analysis of TE and TM-polarized emission in InAs/GaAs quantum dots as a function of dot asymmetry, size and aspect ratio, as a means to identify and understand the polarization characteristics of InAs-based quantum dots grown on GaAs.

Although the z analysis has been widely used to study how the dominant carrier recombination process at threshold changes with temperature, studying z as a function of current at a given temperature has not been widely used. We showed here that the z analysis can be used in this way to identify changes in the dominant recombination process, as well as the interplay of a number of recombination processes as a function of current. Such questions are of wide interest in semiconductor LEDs, lasers and amplifiers, and the analysis techniques presented here

should therefore be of value in detailed studies across a wide range of such devices.

Bibliography

[1] Y. Suematsu and K. Iga. Semiconductor Lasers in Photonics. *Journal of Lightwave Technology*, 26:1132–1144, 2008.

[2] I. Tangring, H. Q. Ni, B. P. Wu, D. H. Wu, Y. H. Xiong, S. S. Huang, Z. C. Niu, S. M. Wang, Z. H. Lai, and A. Larsson. 1.58 μm InGaAs Quantum Well Laser on GaAs. *Applied Physics Letters*, 91:221101, 2007.

[3] L. Ya. Karachinsky, T. Kettler, I. I. Novikov, Yu. M. Shernyakov, N. Yu. Gordeev, M. V. Maximov, N. V. Kryzhanovskaya, A. E. Zhukov, E. S. Semenova, A. P. Vasil'ev, V. M. Ustinov, G. Fiol, M. Kuntz, A. Lochmann, O. Schulz, L. Reissmann, K. Posilovic, A. R. Kovsh, S. S. Mikhrin, V. A. Shchukin, N. N. Ledentsov, and D. Bimberg. Metamorphic 1.5 μm-Range Quantum Dot Lasers on a GaAs Substrate. *Semiconductor Science and Technology*, 21:691–696, 2006.

[4] Y. Arakawa and H. Sakai. Multidimensional Quantum Well Laser and Temperature Dependence of its Threshold Current. *Applied Physics Letters*, 40:939, 1982.

[5] D. Bimberg, M. Grundmann, and N. N Ledentsov. *Quantum Dot Heterostructures*. Wiley, 1999.

[6] J. P. Reithmaier, A. Somers, S. Deubert, R. Schwertberger, W. Kaiser, A. Forchel, M. Calligaro, P. Resneau, O. Parillaud, S. Bansropun, M. Krakowski, R. Alizon, D. Hadass, A. Bilenca, H. Dery, V. Mikhelashvili, G. Eisenstein, M. Gioannini, I. Montrosset, T. W. Berg, M. van der Poel, J Mork, and B. Tromborg. InP Based Lasers and Optical Amplifiers with Wire-/Dot-Like Active Regions. *Journal of Physics D: Applied Physics*, 38:20882102, 2005.

[7] F. Lelarge, B. Dagens, J. Renaudier, R. Brenot, A. Accard, F. van Dijk, D. Make, O. Le Gouezigou, J.-G. Provost, F. Poingt, J. Landreau, O. Drisse, E. Derouin, B. Rousseau, F. Pommereau, and G.-H. Duan. Recent Advances on InAs/InP Quantum Dash Based Semiconductor Lasers and Optical Amplifiers Operating at 1.55 μm. *IEEE Journal of Selected Topics in Quantum Electronics*, 13:111, 2007.

[8] H. C. Casey and M. B. Panish. *Heterostructure Lasers. Part A: Fundamental Principles*. Academic Press Inc., New York, 1978.

[9] G. P. Agrawal and N. K. Dutta. *Long-wavelength Semiconductor Lasers*. Van Nostrand Reinhold, 1986.

[10] Z. I. Alferov. The History and Future of Semiconductor Heterostructures. *Semiconductors*, 32:1–14, 1998.

[11] R.N. Hall, G. E. Fenner, J. D. Kingsley, T. J. Soltys, and R. O. Carlson. Coherent Light Emission from GaAs Junctions. *Physical Review Letters*, 9:366–368, 1962.

[12] M. I. Nathan, W. P. Dumke, G. Burns, Jr F. H. Dill, and G. Lasher. Stimulated Emission of Radiation from GaAs P-N Junctions. *Applied Physics Letters*, 1:62, 1962.

[13] N. Holonyak and S. F. Bevacqua. Coherent (Visible) Light Emission from $Ga(As_{1-x}P_x)$. *Applied Physics Letters*, 1:82–83, 1962.

[14] T. M. Quist, R. H. Rediker, R. J. Keyes, W. E. Krag, B. Lax, A. L. McWhorter, and H. J. Zeigler. Semiconductor Maser of GaAs. *Applied Physics Letters*, 1:91–92, 1962.

[15] H. Kroemer. A Proposed Class of Heterojunction Injection Lasers. *Proceedings of the IEEE*, 51:1782–1783, 1963.

[16] Z. I. Alferov, V. M. Andreev, E. L. Portnoy, and M. K. Trukan. AlAs/GaAs Heterojunction Injection Lasers with a Low Room-Temperature Threshold. *Soviet Physics - Semiconductors*, 3:11071110, 1970.

[17] Z. I. Alferov, V. M. Andreev, D. Z. Garbuzov, Y. V. Zhilyaev, E. P. Morozov, E. L. Portnoi, and V. G. Trofim. Investigation of the Influence of the AlAs/GaAs Heterostructure Parameters on the Laser Threshold Current and the Realization of Continuous Emission at the Room Temperature. *Soviet Physics - Semiconductors*, 4:15731575, 1971.

[18] I. Hayashi, M. B. Panish, P. W. Foy, and S. Sumski. Junction Lasers which Operate Continuously at Room Temperature. *Applied Physics Letters*, 17:109–111, 1970.

[19] K. Oe, S. Ando, and K. Sugiyama. 1.3 μm CW Operation of GaInAsP/InP DH Diode Lasers at Room Temperature. *Japanese Journal of Applied Physics*, 16:1273–1274, 1977.

[20] S. Arai, M. Asada, Y. Suematsu, and Y. Itaya. Room Temperature CW Operation of GaInAsP/InP DH Laser Emitting at 1.51 μm. *Japanese Journal of Applied Physics*, 18 (12):2333–2334, 1979.

[21] C.-E. Zah, R. Bhah, B. N. Pathak, F. Favire, W. Lin, M. C. Wang, N. C. Andreadakis, D. M. Hwang, M. A. Koza, T.-P. Lee, Z. Wang, D. Darby, D. Flanders, and J. J. Hsieh. High-Performance Uncooled 1.3 μm $Al_xGa_yIn_{1-x-y}As/InP$ Strained-Layer Quantum-Well Lasers for Subscriber Loop Applications. *IEEE Journal Of Quantum Electronics*, 30:511–523, 1994.

[22] J. P. van der Ziel, R. Dingle, R. C. Miller, W. Wiegmann, and W. A. Nordland Jr. Laser Oscillations from Quantum States in Very Thin GaAsAlGaAs Multilayer Structures. *Applied Physics Letters*, 26:463–465, 1975.

[23] W. T. Tsang. Extremely Low Threshold (AlGa)As Graded-Index Waveguide Separate-Confinement Heterostructure Lasers Grown by Molecular-Beam Epitaxy. *Applied Physics Letters*, 40:217–219, 1982.

[24] N. Kirstaedter, N.N. Ledentsov, M. Grundmann, D. Bimberg, V. M. Ustinov, S.S. Ruvimov, M.V. Maximov, P.S. Kop'ev, Z.I. Alferov, U. Richter, P. Werner, U. Gdsele, and J. Heydenreich. Low Threshold, Large T_0 Injection Laser Emission from (InGa)As Quantum Dots. *Electronics Letters*, 30:1416–1418, 1994.

[25] G. Park, O. B. Shchekin, D. L. Huffaker, and D. G. Deppe. Low-Threshold Oxide-Confined 1.3 μm Quantum-Dot Laser. *IEEE Photonics Technology Letters*, 13:230–232, 2000.

[26] M. Kondow, K. Uomi, A. Niwa, T. Kitatani, S. Watahiki, and Y. Yazami. GaInNAs: A Novel Material for Long-Wavelength-Range Laser Diodes with Excellent High Temperature Performance. *Japanese Journal of Applied Physics*, 35:1273–1275, 1996.

[27] S. R. Bank, M. A.Wistey, L. L. Goddard, H. B. Yuen, V. Lordi, and J. S. Harris. Low-Threshold Continuous-Wave 1.5 μm GaInNAsSb Lasers Grown on GaAs. *IEEE Journal Of Quantum Electronics*, 40 (6):656–664, 2004.

[28] M. Yokozeki, J. Mitomo, Y. Sato, T. Hino, and H. Narui. 1.50 μm CW Operation of GaInNAs/GaAs Laser Diodes Grown by MOCVD. *Electronics Letters*, 40:1060–1061, 2004.

[29] N.N. Ledentsov, A.R. Kovsh, A.E. Zhukov, N.A. Maleev, S.S. Mikhrin, A.P. Vasilev, E.S. Semenova, M.V. Maximov, , Yu.M. Shemyakov, N.V Kryzhanovskaya, V. M. Ustinov, and D. Bimberg. High Performance Quantum Dot Lasers on GaAs Substrates Operating in 1.5 μm Range. *Electronics Letters*, 39:1126–1128, 2003.

[30] A. E. Zhukov, A. R. Kovsh, S. S. Mikhrin, E. S. Semenova, N. A. Maleev, A. P. Vasilev, E. V. Nikitina, N. V. Kryzhanovskaya, A. G. Gladyshev, Yu. M. Shernyakov, Yu. G. Musikhin, M. V. Maksimov, N. N. Ledentsov, V. M. Ustinov, and Zh. I. Alferov. Metamorphic Lasers for 1.3 μm Spectral Range Grown on GaAs Substrates by MBE. *Semiconductors*, 37:11191122., 2003.

[31] H. Saito, K. Nishi, and S. Sugou. Ground-State Lasing at Room Temperature in Long-Wavelength InAs Quantum-Dot Lasers on InP(311)B Substrates. *Applied Physics Letters*, 78:267–269, 2001.

[32] L. A. Coldren and S. W. Corzine. *Diode Lasers and Photonic Integrated Circuits*. Wiley-Interscience, 1995.

[33] M. G. A. Bernard and G. Duraffourg. Laser Conditions in Semiconductors. *physica status solidi*, 1:699–703, 1961.

[34] S. L. Chuang. *Physics of Optoelectronic Devices*. Wiley Series in Pure and Applied Optics, 1995.

[35] E.P. O'Reilly. *Quantum Theory of Solids (Kindle Edition)*. Routledge, USA, 2003.

[36] P. S. Zory, editor. *Quantum Well Lasers*. Academic Press, 1993.

[37] M. Gioannini. Analysis of the Optical Gain Characteristics of Semiconductor Quantum-Dash Materials Including the Band Structure Modifications due to the Wetting Layer. *IEEE Journal of Selected Topics in Quantum Electronics*, 42:331–340, 2006.

[38] P.M. Smowton and P. Blood. The Differential Efficiency of Quantum-Well Lasers. *IEEE Journal of Selected Topics in Quantum Electronics*, 3:491–498, 1997.

[39] A. F. Phillips, S. J. Sweeney, A. R. Adams, and P. J. A. Thijs. The Temperature Dependence of 1.3 and 1.5 μm Compressively Strained InGaAs(P) MQW Semiconductor Lasers. *IEEE Journal of Selected Topics in Quantum Electronics*, 5:401–412, 1999.

[40] M. Asada and Y. Suematsu. Measurement of Spontaneous Emission Efficiency and Nonradiative Recombinations in 1.58 μm Wavelength GaInAsP/InP crystals. *Applied Physics Letters*, 41:353–355, 1982.

[41] R. Olshansky, C. Su, J. Manning, and W. Powazinik. Measurement of Radiative and Nonradiative Recombination Rates in InGaAsP and AlGaAs Light Sources. *IEEE Journal Of Quantum Electronics*, 20:838– 854, 1984.

[42] F. Girardin and G.-H. Duan. Characterization of Semiconductor Lasers by Spontaneous Emission Measurements. *IEEE Journal of Selected Topics in Quantum Electronics*, 3:461–470, 1997.

[43] C. A. Volkert and A. M. Minor. Focused Ion Beam Microscopy and Micromachining. *Material Research Society Bulletin*, 32:389–399, 2007.

[44] M. Sugiyama and G. Sigesato. A Review of Focused Ion Beam Technology and its Applications in Transmission Electron Microscopy. *Journal of Electron Microscopy*, 53:527–536, 2004.

[45] S. Rubanov and P.R. Munroe. Damage in III-V Compounds during Focused Ion Beam Milling. *Microscopy and Microanalysis*, 11:446–455, 2005.

[46] J. Orloff, L. Swanson, and M. W. Utlaut. *High resolution Focused Ion Beams*. Springer, 2003.

[47] A. A. Tseng, I. A. Insua, J.-S. Park, and C. D. Chen. Milling Yield Estimation in Focused Ion Beam Milling of Two-Layer Substrates. *Journal of Micromechanics and Microengineering*, 15:2028, 2005.

[48] C.-F. Lin. *Optical Components for Communications*. Springer, 2004.

[49] P. Togher. *The Temperature Dependence of the Gain in Semiconductor Lasers*. PhD thesis, Department of Physics University of Surrey, 1996.

[50] P. C. Mogensen, S. A. Hall, P. M. Smowton, U. Bangert, P. Blood, and P. Dawson. The Effect of High Compressive Strain on the Operation tf AlGaInP Quantum-Well Lasers. *IEEE Journal Of Quantum Electronics*, 34:1652 – 1659, 1998.

[51] J. S. Liang, S. D. Wang, Y. S. Huang, C. W. Tien, Y. M. Chang, C. W. Chen, N. Y. Li, D. Y. Lin, and F. H Pollak. Polarized Edge-Incident Photovoltage Spectroscopy and Reflectance Characterization of a GaAs/GaAlAs Vertical-Cavity Surface-Emitting Laser Structure. *Applied Physics Letters*, 80:752–754, 2002.

[52] I. C. Sandall, P. M. Smowton, C. L. Walker, H. Y. Liu, M. Hopkinson, and D. J. Mowbray. Recombination Mechanisms in 1.3 μm InAs Quantum-Dot Lasers. *IEEE Photonics Technology Letters*, 18:965–967, 2006.

[53] M. Mexis, P. M. Smowton, and P. Blood. Polarization Response of Quantum-Confined Structures using Edge-Photovoltage Spectroscopy. *Semiconductor Science and Technology*, 22:1298–1301, 2007.

[54] P. A. Probst and B. Collet. Low-Frequency Digital Lock-In Amplifier. *Review of Scientific Instruments*, 56:466–470, 1985.

[55] What is a Lock-in Amplifier? Technical report, PerkinElmer, TN 1000.

[56] C. H. Henry, R. A. Logan, and K.A. Bertness. Measurement of Spectrum, Bias Dependence, and Intensity of Spontaneous Emission in GaAs Lasers. *Journal of Applied Physics*, 52:4453–4456, 1981.

[57] M. P. Kesler and C. Harder. Spontaneous Emission and Gain in GaAlAs Quantum Well Lasers. *IEEE Journal Of Quantum Electronics*, 21:1812–1816, 1991.

[58] B. W. Hakki and T. L. Pauli. Gain Spectra in GaAs Double-Heterostructure Injection Lasers. *Journal of Applied Physics*, 46, Issue 3:1299–1306, 1975.

[59] E. S.-M. Tsui, P. Blood, and E. D. Fletcher. Electroluminescent Processes in Quantum Well Structures. *Semiconductor Science and Technology*, 7:837–844., 1992.

[60] *Leybold Spec. Sheets*.

[61] M. Asada, Y. Miamoto, and Y. Suematsu. Gain and the Threshold of Three-Dimensional Quantum-Box Lasers. *IEEE Journal Of Quantum Electronics*, 22:1915–1921, 1986.

[62] G.T. Liu, A. Stintz, H. Li, K.J. Malloy, and L.F. Lester. Extremely Low Room-Temperature Threshold Current Density Diode Lasers using $lnAsDotsinIn_{0.5}Ga_{0.85}As$ Quantum Well. *Electronics Letters*, 35:1163, 1999.

[63] S. Azouigui, B. Kelleher, S. P. Hegarty, G. Huyet, B. Dagens, F. Lelarge, A. Accard, D. Make, O. Le Gouezigou, K. Merghem, A. Martinez, Q. Zou, and A. Ramdane. Coherence Collapse and Low-Frequency Fluctuations in Quantum-Dash Based Lasers Emitting at 1.57 μm. *Optics Express*, 15 (21):14155–14162, 2007.

[64] C. Gosset, K. Merghem, A. Martinez, G. Moreau, G. Patriarche, G. Aubin, A. Ramdane, J. Landreau, and F. Lelarge. Subpicosecond Pulse Generation at 134 GHz using a Quantum-Dash-Based Fabry-Pérot Laser Emitting at 1.56 μm. *Applied Physics Letters*, 88:241105, 2006.

[65] J.-M. Lamy, C. Levallois, A. Nakhar1, P. Caroff, C. Paranthoen, R. Piron1, A. Le Corre, A. Ramdane, and S. Loualiche. Characterization of InAs Quantum Wires on (001)InP: Toward the Realization of VCSEL Structures with a Stabilized Polarization. *physica status solidi (a)*, 204:16721676, 2007.

[66] I. P. Marko, A. D. Andreev, A. R. Adams, R. Krebs, J. P. Reithmaier, and A. Forchel. The Role of Auger Recombination in InAs 1.3 μm Quantum-Dot Lasers Investigated using High Hydrostatic Pressure. *IEEE Journal of Selected Topics in Quantum Electronics*, 9:1300–1307, 2003.

[67] C.-Y. Jin, T. J. Badcock, H.-Y. Liu, K. M. Groom, R. J. Royce, D. J. Mowbray, and M. Hopkinson. Observation and Modeling of a Room-Temperature Negative Characteristic Temperature 1.3 μm P-type Modulation-doped Quantum-Dot Laser. *IEEE Journal Of Quantum Electronics*, 42:1259–1265., 2006.

[68] B. Dagens, D. Make, F. Lelarge, B. Rousseau, M. Calligaro, M. Carbonnelle, F. Pommereau, A. Accard, F. Poingt, L. Le Gouezigou, C. Dernazaretian, O. Le Gouezigou, J.-G. Provost, F. van Dijk, P. Resneau, M. Krakowski, and G.-H. Duan. High Bandwidth Operation of Directly Modulated Laser Based on Quantum-Dash InAs–InP Material at 1.55 μ m. *IEEE Photonics Technology Letters*, 20(11):903–905, 2008.

[69] M. Silver and E. P. O'Reilly. Optimization of Long Wavelength InGaAsP Strained-Quantum-Well Lasers. *IEEE Journal Of Quantum Electronics*, 31(7):1193 – 1200, July 1995.

[70] T. B. Bahder. 8-Band K.P Model of Strained Zincblend Crystals. *Physical Review B*, 41(17):11992 – 12001, 1990.

[71] A. D. Andreev and E. P. O'Reilly. Theory of the Electronic Structure of GaN/AlN Hexagonal Quantum Dots. *Physical Review B*, 62(23):15851 – 15870, 2000.

[72] M. Gioannini. Numerical Modeling of the Emission Characteristics of Semiconductor Quantum Dash Materials for Lasers and Optical Amplifiers. *IEEE Journal of Quantum Electronics*, 40(4):364–373, 2004.

[73] F. Szmulowicz. Derivation of a General Expression for the Momentum Matrix-Elements within the Envelope-Function Approximation. *Physical Review B*, 51:1613–1623, January 1995.

[74] S Tomić, E. P. O'Reilly, R. Fehse, S. J. Sweeney, A. R. Adams, A. D. Andreev, S. A. Choulis, T. J. C. Hosea, and H Riechert. Theoretical and Experimental Analysis of 1.3 μm InGaAsN/GaAs Lasers. *IEEE Journal of Selected Topics in Quantum Electronics*, 9(5):1228 – 1238, September 2003.

[75] A. T. Meney, E. P. O'Reilly, and K. J. Ebeling. Polarisation Selectivity in Ordered GaInP2 Vertical Cavity Surface Emitting Lasers. *Electronics Letters*, 31:461–462, 1995.

[76] G.G. Forstmann, F. Barth, H. Schweizer, M. Moser, C. Geng, F. Scholz, and E.P. O'Reilly. Effects of Strain and GaInP2 Superlattice Ordering on Laser Polarization. *Semiconductor Science and Technology*, 9:1268–1271, 1994.

[77] S. B. Healy and E. P. O'Reilly. A Theoretical Investigation of Anisotropic Gain Mechanisms in 1.55 μm InGaAsP Quantum Dash Devices. *to be submitted to IEEE Journal Of Quantum Electronics.*

[78] N. F. Massé, E. Homeyer, I. P. Marko, A. R. Adams, S. J. Sweeney, O. Dehaese, R. Piron, F. Grillot, and S. Loualiche. Temperature and Pressure Dependence of the Recombination Processes in 1.5 μm InAs/InP (311B) Quantum Dot Lasers. *Applied Physics Letters*, 91:131113, 2007.

[79] S. J. Sweeney, A. F. Phillips, A. R. Adams, E. P. OReilly, and P. J. A. Thijs. The Effect of Temperature Dependent Processes on the Performance of 1.5 μ m Compressively Strained InGaAs(P) MQW Semiconductor Diode Lasers. *IEEE Photonics Technology Letters*, 10:1076–1078, 1998.

[80] D. A. Neamen. *Semiconductor Physics and Devices: Basic Principles.* McGraw-Hill Professional, 2002.

[81] K. J. Vahala and C. E. Zah. Effect of Doping on the Optical Gain and the Spontaneous Noise Enhancement Factor in Quantum Well Amplifiers and Lasers Studied by Simple Analytical Expressions. *Applied Physics Letters*, 52:1945–1947, 1988.

[82] T. Takahashi and Y. Arakawa. Theoretical Analysis of Gain and Dynamic Properties of Quantum-Well Box Lasers. *Optoelectronics -Devices and Technologies*, 3:155–162, 1988.

[83] Y. Miyamoto, Y. Miyake, M. Asada, and Y. Suematsu. Threshold Current Density of GaInAsP/InP Quantum-Box Lasers. *IEEE Journal Of Quantum Electronics*, 25:2001–2006, 1989.

[84] K. Uomi, T. Mishima, and N. Chinone. Ultrahigh Relaxation Oscillation Frequency (up to 30 GHz) of Highly P-doped Ga/GaAlAs Multiple Quantum Well Lasers. *Applied Physics Letters*, 51:78–80, 1987.

[85] C. E. Zah, R. Bhat, S. G. Menocal, F. Favire, N. C. Andreadarkis, M. A Koza, C. Caneau, S. A. Schwarz, Y. Lo, and T.P. Lee. Cavity Length and Doping Dependence of 1.5 μm GaInAs/GaInAsP Multiple Quantum Well Laser Characteristics. *IEEE Photonics Technology Letters*, 2:231–233, 1990.

[86] O. B. Shchekin and D. G. Deppe. The Role of P-type Doping and the Density of States on the Modulation Response of Quantum Dot Lasers. *IEEE Journal Of Quantum Electronics*, 80:2758–2760, 2002.

[87] D. G. Deppe, H. Huang, and O. B. Shchekin. Modulation Characteristics of Quantum-Dot Lasers: The Influence of P-type Doping and the Electronic Density of States on Obtaining High Speed. *IEEE Journal Of Quantum Electronics*, 38:1587–1593, 2002.

[88] P. M. Smowton, I. C. Sandall, H. Y. Liu, and M. Hopkinson. Gain in P-doped Quantum Dot Lasers. *Applied Physics Letters*, 101:013107, 2007.

[89] S. Fathpour, Z. Mi, P. Bhattacharya, A. R. Kovsh, S. S. Mikhrin, I. L. Krestnikov, A. V. Kozhukhov, and N. N. Ledentsov. The Role of Auger Recombination in the Temperature-Dependent Output Characteristics ($T_0 = \infty$) of P-doped 1.3 μm Quantum Dot Lasers. *Applied Physics Letters*, 85:5164–5166, 2004.

[90] P. M. Smowton, I. C. Sandall, D. J. Mowbray, H. Y. Liu, and M.Hopkinson. Temperature-Dependent Gain and Threshold in P-doped Quantum Dot Lasers. *IEEE Journal of Selected Topics in Quantum Electronics*, 13:1261–1266, 2007.

[91] N. F. Massé, I. P. Marko, A. R. Adams, and S. J. Sweeney. Temperature Insensitive Quantum Dot Lasers: Are We Really There Yet? *Journal of Materials Science: Materials in Electronics*, 20:S272S276, 2007.

[92] O. B. Shchekin and D. G. Deppe. 1.3 μm InAs Quantum Dot Laser with T_0 = 161 K From 0 to 80 °C . *Applied Physics Letters*, 80:3277–3279, 2002.

[93] K. Otsubo, N. Hatori, M. Ishida, S. Okumura, T. Akiyama, Y. Nakata, H. Ebe, M. Sugawara, and Y. Arakawa. Temperature-Insensitive Eye-Opening under 10-Gb/s Modulation of 1.3 μm P-doped Quantum-Dot Lasers without Current Adjustments. *Japanese Journal of Applied Physics*, 43:L1124–L1126, 2004.

[94] O. B. Shchekin and D. G. Deppe. Low-Threshold High-T_0 1.3 μm InAs Quantum-Dot Lasers due to P-type Modulation Doping of the Active Region. *IEEE Photonics Technology Letters*, 14:1231–1233, 2002.

[95] I. P. Marko, N. F. Massé, S. J. Sweeney, A. D. Andreev, and A. R. Adams. Carrier Transport and Recombination in P-Ddoped and Intrinsic 1.3 μm InAs/GaAs Quantum-Dot Lasers. *Applied Physics Letters*, 87:211114, 2005.

[96] Z. Mi and P. Bhattacharya. DC and Dynamic Characteristics of P-doped and Tunnel Injection 1.65 μm InAs Quantum-Dash Lasers Grown on InP (001). *IEEE Journal Of Quantum Electronics*, 42:1224–1232, 2006.

[97] Y. Li, T. J. Rotter, Y. C. Xin, A. Stinz, A. Martinez, K. J. Malloy, S. Patterson, and L. F. Lester. High Characteristic Temperature of P-doped InAs Quantum Dots-in-a-well Lasers on InP Substrate. In *Conference on Lasers and Electro-Optics (CLEO)*, 2006.

[98] M. T. Crowley, I. P. Marko, N. F. Mass, A. D. Andreev, S. Tomi?, S. J. Sweeney, E. P. OReilly, and A. R. Adams. The Importance of Recombination Via Excited States in InAs/GaAs 1.3 μm Quantum Dot Lasers. *to be published in IEEE Journal of Selected Topics in Quantum Electronics*, 2009.

[99] S. Y. Hu, S. W. Corzine, K.-K. Law, D. B. Young, A. C. Gossard, L. A. Coldren, and J. L. Merz. Lateral Carrier Diffusion and Surface Recombination in InGaAs/AlGaAs Quantum-Well Ridge-Waveguide Lasers. *Journal of Applied Physics*, 76:4479–4487, 1994.

[100] H. Dong and A. Gopinath. Optical Switches using Active AlGaAs/GaAs Ridge Waveguides. Technical report, University of Minnesota, 1995.

[101] S. Ghosh, P. Bhattacharya, E. Stoner, , J. Singh, H. Jiang, S. Nuttinck, and J. Laskar. Temperature-Dependent Measurement of Auger Recombination in Self-Organized $In_{0.4}Ga_{0.6}As$/GaAs quantum dots. *Applied Physics Letters*, 79:722–724, 2001.

[102] A. Sugimura. Comparison of Band-To-Band Auger Processes in InGaAsP. *IEEE Journal Of Quantum Electronics*, QE-19:930–932, 1983.

[103] M. Silver, E. P. O'Reilly, and A. R. Adams. Determination of the Wavelength Dependence of Auger Recombination in Long-Wavelength Quantum-Well Semiconductor Lasers using Hydrostatic Pressure. *IEEE Journal Of Quantum Electronics*, 33:1557–1566, 1997.

[104] R. Fehse. *Recombination Processes in GaInNAs/GaAs Semiconductor Quantum-Well Lasers*. PhD thesis, Department of Physics School of Electronics and Physical Sciences University of Surrey, 2003.

[105] S.C. Heck, S.B. Healy, S. Osborne, D.P. Williams, R. Fehse, E.P. O'Reilly, F. Lelarge, F. Poingt, A. Accard, F. Pommereau, O. Le Gouezigou, and B. Dagens. Theoretical and Experimental Analysis of InAs/InP Quantum Dash Lasers. In *IEEE Conference on Indium Phosphide and Related Materials (IPRM)*, 2008.

[106] K. Takemasa, M. Kubota, T. Munakata, and H.i Wada. 1.3 μm AlGaInAs Buried-Heterostructure Lasers. *IEEE Photonics Technology Letters*, 11(8):949–951, 1999.

[107] T. Higashi, S. J. Sweeney, A. F. Phillips, A. R. Adams, E. P. O'Reilly, T. Uchida, and T. Fujii. Experimental Analysis of Temperature Dependence in 1.3 μm AlGaInAsInP Strained MQW Lasers. *IEEE Journal of Selected Topics in Quantum Electronics*, 5:413–419, 1999.

[108] R. H. Wang, A. Stintz, P. M. Varangis, T. C. Newell, H. Li, K. J. Malloy, and L. F. Lester. Room-Temperature Operation of InAs Quantum-Dash Lasers on InP (001). *IEEE Photonics Technology Letters*, 13:767–769, 2001.

[109] R. Schwertberger, D. Gold, J.P. Reithmaier, and A. Forchel. Epitaxial Growth of 1.55 μm Emitting InAs Quantum Dashes on InP-Based Heterostructures by GS-MBE for Long-Wavelength Laser Applications. *Journal of Crystal Growth*, 251:248252, 2003.

[110] S. Hein, A. Somers, S. Höfling, and A. Forchel. Low Threshold High Efficiency InAs/InGaAlAs/InP 1.55 μm Quantum Dash-in-a-well Lasers. In *IEEE Conference on Indium Phosphide and Related Materials (IPRM)*, 2007.

[111] J. H. Wei and K. S. Chana. A Theoretical Analysis of Quantum Dash Structures. *Journal of Applied Physics*, 97:123524, 2005.

[112] I. P. Marko, S. J. Sweeney, A. R. Adams, S. R. Jin, B. N. Murdin, R. Schwertberger, A. Somers, J. P. Reithmaier, and A. Forchel. Recombination Mechanisms in InAs/InP Quantum Dash Lasers Studied using High Hydrostatic Pressure. *physica status solidi (b)*, 241:34273431, 2004.

[113] H. Dery, E. Benisty, A. Epstein, R. Alizon, V. Mikhelashvili, G. Eisenstein, R. Schwertberger, D. Gold, J. P. Reithmaier, and A. Forchel. On the Nature of Quantum Dash Structures. *Applied Physics Letters*, 95:6103–6111, 2004.

[114] Takashi Kita, Osamu Wada, Hiroji Ebe, Yoshiaki Nakata, and Mitsuru Sugawara. Polarization-Independent Photoluminescence from Columnar InAs/GaAs Self-Assembled Quantum Dots. *Japanese Journal of Applied Physics*, 41:L 1143–L 1145, 2002.

[115] P. Jayavel, H. Tanaka, T. Kita, O. Wada, H. Ebe, M. Sugawara, J. Tatebayashi, Y. Arakawa, Y. Nakata, and T. Akiyama. Control of Optical Polarization Anisotropy in Edge Emitting Luminescence of InAs/GaAs Self-Assembled Quantum Dots. *Applied Physics Letters*, 84:1820–1822, 2004.

[116] P. Ridha, L. Li, M. Rossetti, G. Patriarche, and A. Fiore. Polarization dependence of electroluminescence from closely-stacked and columnar quantum dots. *Optical and Quantum Electronics*, 40:239–248, 2008.

[117] N. Yasuoka, K. Kawaguchi, H. Ebe, T. Akiyama, M. Ekawa, S. Tanaka, K. Morito, A. Uetake, M. Sugawara, and Y. Arakawa. Demonstration of transverse-magnetic dominant gain in quantum dot semiconductor optical amplifiers. *Applied Physics Letters*, 92:101108, 2008.

[118] K. Kawaguchi, N. Yasuoka, M. Ekawa, H. Ebe, T. Akiyama, M. Sugawara, and Y. Arakawa. Controlling Polarization of 1.55 μm Columnar InAs Quantum Dots With Highly Tensile-Strained InGaAsP Barriers on InP(001). *Japanese Journal of Applied Physics*, 45:L1244–L1246, 2006.

[119] S. Anantathanasarn, P. J. van Veldhoven, T. J. Eijkemans, T. de Vries, E. Smalbrugge, E. J. Geluk, E. A. J. M. Bente, Y. S. Oei, M. K. Smit, and R. Ntzela. Polarization Control of Gain of Stacked InAs/InP (100) Quantum Dots at 1.55 μm: Interplay Between Ground and Excited State Transitions. *Applied Physics Letters*, 92:123113, 2008.

[120] P. Podemski, G. Sek, K. Ryczko, J. Misiewicz, S. Hein, S. Hfling, A. Forchel, and G. Patriarche. Columnar Quantum Dashes for an Active Region in Polarization Independent Semiconductor Optical Amplifiers at 1.55 μm. *Applied Physics Letters*, 93:171910, 2008.

[121] G. A. Narvaez and A. Zunger. Nominally Forbidden Transitions in the Interband Optical Spectrum of Quantum Dots. *Physical Review B*, 75:045316–(1–6), 2006.

[122] R. M. Stevenson, R. J. Young, P. See, C. E. Norman, A. J. Shields, P. Atkinson, and D. A. Ritchie. Strong directional dependence of single-quantum-dot fine structure. *Applied Physics Letters*, 87:133120, 2005.

[123] S. Osborne. *Optical Gain in Long Wavelength Laser Diodes*. PhD thesis, Cardiff University, Cardiff, U.K., 2004.

[124] S. Cortez, O. Krebs, P. Voisin, and J. M. Gerard. Polarization of the Interband Optical Dipole in InAs/GaAs Self-Organized Quantum Dots. *Physical Review B*, 63:233306, 2001.

[125] P.W. Fry, M.S. Skolnick, D.J. Mowbray, I.E. Itskevich, J.J. Finley, L.R. Wilson, K.L. Schumacher, J.A. Barker, E.P. O'Reilly, M. Al-Khafaji, A.G. Cullis, M. Hopkinson, J.C. Clark, and G. Hill. Electronic Properties of InAs/GaAs Self-Assembled Quantum Dots Studied by Photocurrent Spectroscopy. *Physica E: Low-dimensional Systems and Nanostructures*, 9:106–113, 2001.

[126] P. Ridha, L. Li, A. Fiore, G. Patriarche, M. Mexis, and P. M. Smowton. Polarization Dependence Study of Electroluminescence and Absorption from InAs/GaAs Columnar Quantum Dots. *Applied Physics Letters*, 91:191123, 2007.

[127] A.R. Kovsh, N.A. Maleev, A.E. Zhukov, S.S. Mikhrin, A.P. Vasilea, E.A. Semenova, Yu.M. Shernyakov, M.V. Maximov, D.A. Livshits, V.M. Ustinov, N.N. Ledentsov, D. Bimberg, and Zh.I. Alferov. InAs/InGaAs/GaAs Quantum Dot Lasers of 1.3 μm Range with Enhanced Optical Gain. *Journal of Crystal Growth*, 251:729–736, 2003.

[128] M. Lämmlin. *GaAs-Based Semiconductor Optical Amplifiers with Quantum Dots as an Active Medium*. PhD thesis, Fakultät II Mathematik und Naturwissenschaften der Technischen Universität Berlin, 2006.

[129] I. O'Driscoll. *Carrier Dynamics of InAs/GaAs Semiconductor Quantum Dots*. PhD thesis, Department of Physics, University College Cork, National University of Ireland, Cork, 2007.

[130] L. Chu, M. Arzberger, A. Zrenner, G. Bohm, and G. Abstreiter. Polarization Dependent Photocurrent Spectroscopy of InAs/GaAs Quantum Dots. *Applied Physics Letters*, 75:2247–2249, 1999.